7-24-2014

Molecular Dynamics in Diatomic Molecules with One- and Two-Color Ultrafast Laser Pulses

Vincent Tagliamonti
tagliamonti@gmail.com

Molecular Dynamics in Diatomic Molecules with One- and Two-Color Ultrafast Laser Pulses

Vincent Tagliamonti, Ph.D.

University of Connecticut, 2014

ABSTRACT

Strong field ionization with ultrafast laser pulses allows for real-time measurements of the forming and breaking of chemical bonds. The time duration of an ultrafast pulse is tens of femtoseconds (1 fs = 10^{-15} s) while dynamics such as nuclear vibration and dissociation occurring in small molecules is hundreds of fs. Ultrafast lasers are therefore capable of imaging these dynamics in real-time, providing insight into the physics of molecular ionization, vibration, and orbital structure. I will discuss several experiments examining the effects of strong field ionization in diatomic iodine in the presence of a two-color (800 and 400 nm, $1\omega 2\omega$) phase stable femtosecond laser pulse. By controlling the relative phase of the two-color pulse, the magnitude and direction of the electric field can be controlled. As strong field ionization depends exponentially on the electric field strength, ionization rates can be controlled. The spatial asymmetry of the $1\omega 2\omega$ pulse breaks the spatial symmetry of ionization allowing for control over directions of ion yields while providing insight into the physics of ionization. In particular, this work studies excited states of the doubly ionized molecule which are produced via two processes, described as asymmetric production or depletion of a charge asymmetric dissociation channel. In the production experiment a pump probe technique is used to excite I_2 to the B state of the neutral which is subsequently

ionized by a two color probe pulse. By varying the relative phase between the two colors we are able to probe the asymmetric dissociation of $I_2^{2+} \rightarrow I^{2+} + I$ and we observe spatial asymmetries in the ion yield of this (2,0) channel. The depletion experiment uses a pump pulse at 800 nm to create a wave packet in the (2,0). As the molecule dissociates, a two color probe pulse is used to study the dynamics as a function of internuclear separation, *R*. We find a critical region of *R* in which there is spatially asymmetric enhanced ionization of the (2,0) channel to a counterintuitive (1,2) channel. In this region the neutral iodine atom is ionized such that one electron is released to the continuum and another is transferred to the I^{2+} ion. The production experiment results in a description of ionization into coherent mixed states of the dication while the depletion experiment reveals prominent multielectron dynamics near the critical region of *R*. I will also discuss the development of a velocity map imaging (VMI) detector which provides two-dimensional information about the dissociation and distribution of molecular ions upon ionization. The VMI allows us to identify specific molecular orbitals from which electrons are removed through ionization by measuring the vibrational period and angular distributions of the ion fragments. We study the inner orbital ionization of I_2 and identify the ionized orbitals through Fourier transform spectroscopy.

Molecular Dynamics in Diatomic Molecules with One- and Two-Color Ultrafast Laser Pulses

Vincent Tagliamonti

M.S. California State University, Northridge, 2008

B.S. California State University, Northridge, 2006

A Dissertation

Submitted in Partial Fulfillment of the

Requirements for the Degree of

Doctor of Philosophy

at the

University of Connecticut

2014

APPROVAL PAGE

Doctor of Philosophy Dissertation

Molecular Dynamics in Diatomic Molecules with One- and Two-Color Ultrafast Laser Pulses

Presented by

Vincent Tagliamonti, B.S., M.S.

Major Advisor _____
George Gibson

Associate Advisor _____
Winthrop Smith

Associate Advisor _____
Phillip Gould

University of Connecticut

2014

ACKNOWLEDGEMENTS

My time spent at UConn has helped me develop and grow professionally and there are many people who played instrumental roles in this process. Thank you to my advisor George Gibson for working so closely with me in the lab. His hands-on approach to teaching in the lab has provided me with the necessary skills to develop as an experimentalist. Working together with George has always been enlightening and fruitful and my experience as a student in his lab has been quite fulfilling.

I have had a strongly positive experience learning through experimentation and discussion with my labmates and peers. My thanks to Hui Chen for working closely with me both in developing and performing experiments as well as discussing results. Together we successfully published several papers and developed new techniques to be used in the lab. Thank you for your time and help, it has been a pleasure working with you. Thanks to Katya Sergan and Dale Smith as well for our time spent in the lab together. I wish you all the best in your future work and careers.

I would also like to thank the members of my committee, Phil Gould and Win Smith, for taking time to read my dissertation and provide useful comments and questions for my consideration. Special thanks to Niloy Dutta and Jason Hancock for attending my dissertation defense and offering constructive discussion and questions.

I have had the chance to make many great friends over the last few years and I would like to thank them for making my time here even more enjoyable. Thank you to Leland Aldridge, Michael Ambroselli, Alex Barnes, Jen Carini, Ryan Carollo, Brad Clarke, Rob

Dabrowski, Doug Goodman, Nick Lewkow, Chris Sanborn, and James Wells. Thank you also to members of the department including Dr. Gerald Dunne, Dr. Jeff Schweitzer, Dr. Alex Kovner, and Dr. Robin Cote for your time as mentors.

Thank you to Kim Giard and Dawn Rawlinson in the office and thank you to Alan Chasse in the machine shop for all of your help and patience.

I would like to thank my parents for their encouragement over these last few years and for their love all the years before that. I am thankful that we were able to remain close while I was away at school. Thank you both for providing me with the work ethic and self-confidence to achieve.

Contents

List of Figures

List of Tables

Chapter 1

Introduction

Since the inception of the laser in 1960, atomic and molecular physics has undergone substantial growth in experimental methods and theoretical models. Spectroscopy has benefited a great deal from laser use and has resulted in a wealth of information about atomic and molecular stucture. Various Nobel Prizes have been awarded involving lasers, from optical fibers, holography, and atomic clocks to high precision spectroscopy with optical frequency combs and development of the field of femtochemistry. The development of "ultrafast" laser systems in the 1980's pushed the ability and applications of the laser further still by producing pulses of coherent light with femtosecond (1 fs = 10^{-15} s) time durations. This time scale is the natural time of chemical reactions including bond breaking and formation as well as nuclear motion and vibration. The femtosecond laser could therefore take "pictures" of these dynamics in real time, acting as a fast camera, leading to direct observations of atomic and molecular processes as they occur temporally.

1.1 Ultrafast Science Origins

The fairly recent development of ultrafast laser systems and technology has grown out of the questions pertaining to how nature behaves on time scales that can't be "seen" or experienced directly. Indeed, the discovery that light and sound have associated speeds is a realization that is paramount in science. The finite velocity of light is clear in Maxwell's equations with the additional understanding that light has wave-like properties and can be described by the propagation of electric and magnetic fields. Soon after, Michelson and Morley performed experiments to detect the medium in which the light propagates, the aether. Measurements such as these were major in developing an understanding of light and matter.

Understanding the propagation of waves through matter was not unique to light, however. August Toepler (1836-1912) developed visual methods for measureing shock waves and super sonic motion in 1864 known as Schlieren photography (see Fig.1.1.1). Toepler's contributions are arguably the start of visualizing ultrafast events and are still utilized today, for example, in aerospace engineering. Contemporary with Toepler's Schlieren photography, Eadweard Muybridge was working in developing photography, and most famously for "animal locomotion," using a fast shutter and short exposure times. Muybridge was able to capture images of a galloping horse in which one could see that all of the horse's legs were off of the ground at a given moment, images of which were published in Scientific American in 1878 and shown in Fig.1.1.2. This early work in fast photography is some of the first to surpass the limits of human vision where the duration of the blink of a human eye is $\sim$100 ms. Temporal resolution saw further advancement in the mid 20th century with stroboscopic techniques pursued by Harold Edgerton in particular. The use of strobe lighting increased the resolvable visible time scales to $\sim\mu$s and some examples are shown

in Fig.1.1.3. The second half of the twentieth century saw even further technological developments. High speed photography reaching $\sim$1 ns resolution was realized, but reached a plateau as most electronics could not operate reliably beyond this point. However, the development of the laser by 1960 would prove to be an invaluable tool for continuing to probe and understand nature at ever shorter time scales.

1.1.1 Generating Ultrafast Laser Pulses

The method of creating ultrafast laser pulses first requires a broad, coherent bandwidth of frequencies. All of the frequencies produced can have a phase, allowing for constructive and destructive interference, and ideally, all of the frequencies in the laser pulse should be in phase with each other. As there are many possible modes available in a Ti:sapphire oscillator, there will be constructive and destructive interference in the time domain. Adjusting the phases to this point will compress the bandwidth and result in a short laser pulse (Fig. 1.1.5. The shortest possible pulse which can be produced in time for a given bandwidth of frequencies is the transform limited pulse and can be as short as 15-50 fs in duration. These pulses are widely produced using a Ti:sapphire oscillator, although other methods exist to produce even shorter pulses. One such method involves self-phase modulation in gas filled hollow core fibers [84] in conjunction with chirped mirrors, gratings, and pulse-shaping devices to produce pulses of $\sim$5 fs in duration.

Since its development in the 1980's, the Ti:sapphire laser system mentioned above has become widely used in experiments where strong fields are required. The bandwidth for this material is around 600 - 1100 nm with the best operating efficiency around 800 nm. The pulses are therefore in the optical part of the wavelength spectrum and many transitions and interactions of material with light can be studied as an abundance of atoms and small

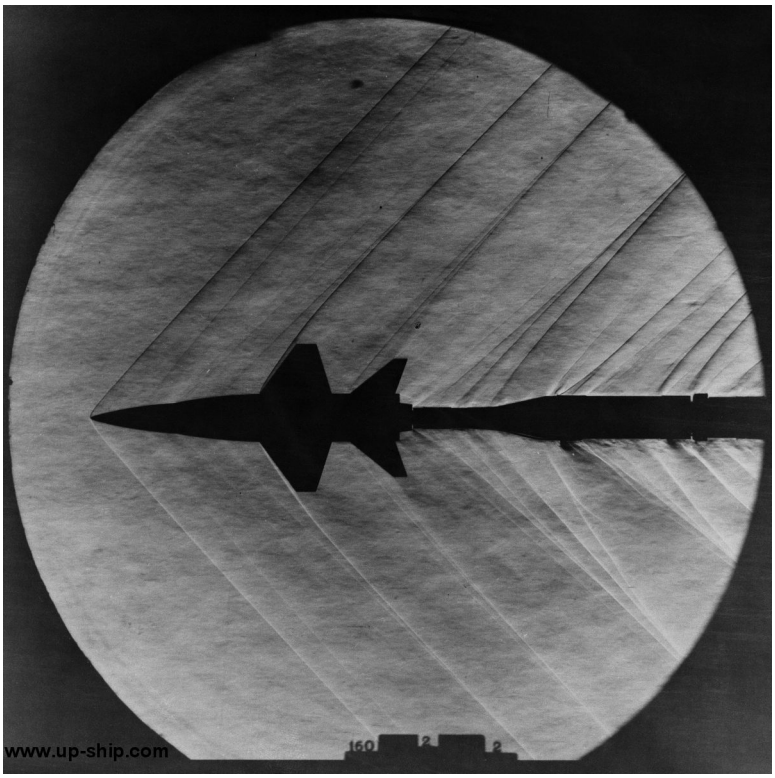

Figure 1.1.1: A NASA photo of an X-15 model jet in a supersonic wind tunnel demonstrating the shockwaves with Schlieren photography.

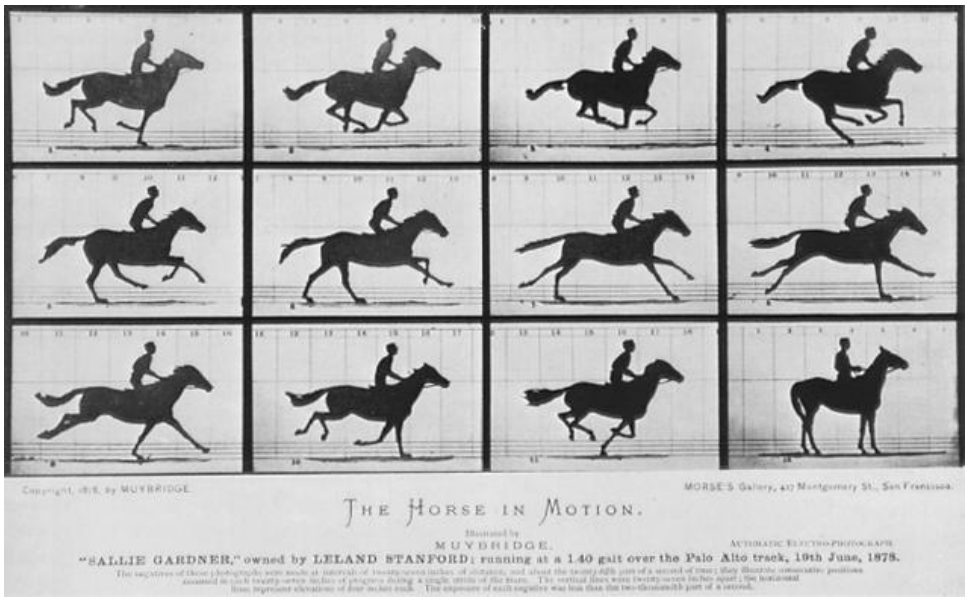

Figure 1.1.2: Photos of a horse galloping as taken by Eadweard Muybridge in the 1870's.

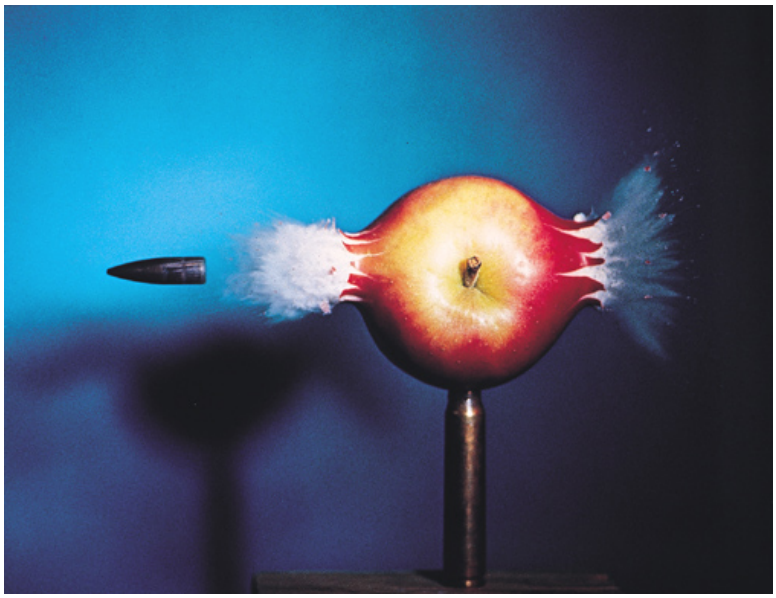

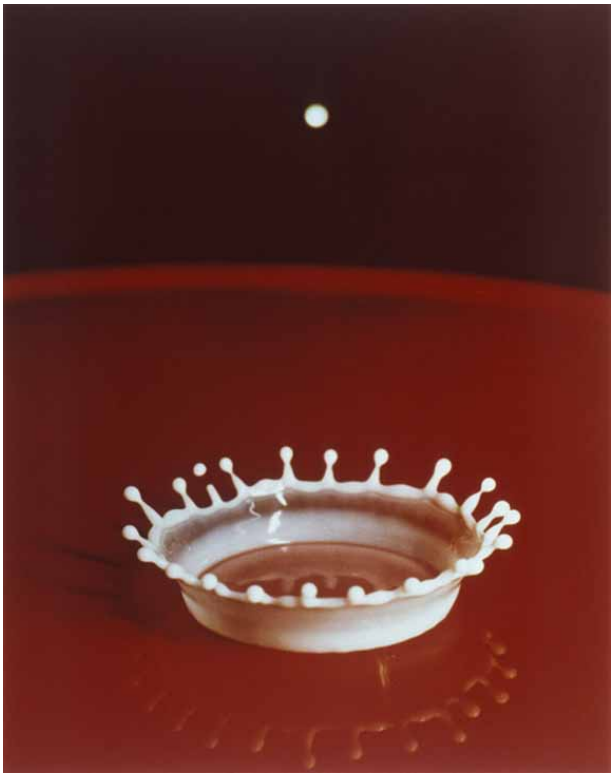

Figure 1.1.3: Well known images taken by Harold Edgerton resolving events in time which are not seen with the naked eye.

molecules have strong interactions with visible light. The Ti:sapphire has a transition or fluorescence lifetime of ~ 3 μs with a peak absorption around 490 nm (blue-green) and is often pumped with an Argon ion or frequency doubled Nd:YAG and YLF lasers which produce light at 532 nm. More recently, diode pump lasers have become available at the wavelengths necessary for pumping Ti:sapphire.

When initially turned on, the laser will typically be in a continuous wave operation with narrow bandwidth. When used in an oscillator, the Ti:sapphire crystal produces a broadband pulse of light through Kerr lens mode locking. A schematic of the oscillator used for this work is presented in Fig. 1.1.4. Fluctuations in the cavity can result in a particular oscillator mode dominating over the others, so called mode locking of the laser. This may occur spontaneously, but often the user must physically bump a mirror or dispersion compensating prism to induce mode locking. A Ti:sapphire laser oscillator will produce a few nanojoules (nJ) at a high repetition rate of $\sim$ 80 MHz, depending on the length of the resonator cavity. These pulses can then be amplified to around 1 mJ using multi-pass amplifiers and chirped pulse amplification which operate at a user defined repetition rate (typically 1 kHz - 10 kHz) to increase the intensity by several orders of magnitude. Intensities of 10^{14} W/cm^2 are regularly achievable, or equivalently, electric field strengths on the order of 1 atomic unit and higher.

The length of the cavity results in many possible modes (on the order of millions) which will compete to gain energy when passing through the crystal (Fig. 1.1.5). The pulses are generated periodically in time depending on the length of the cavity, L, and travel back and forth through the gain medium with a period of $T = 2L/c$ or the round trip time, where c is the speed of light. Each reflection of this pulse at the output coupler mirror will be partly transmitted and leave the cavity. The output laser radiation is then a ”train” of pulses separated in time by the round trip time of the cavity. Again, the pulse duration is inversely

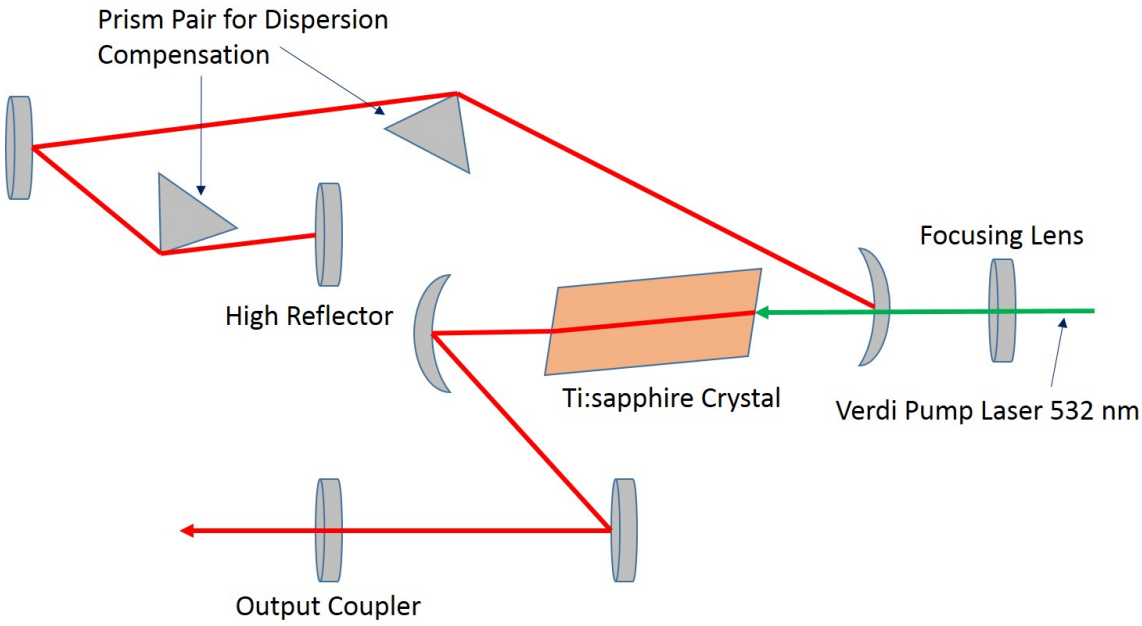

Figure 1.1.4: Schematic layout of the Ti:sapphire oscillator.

related to the spectral width of the gain medium and to the number of oscillating modes as well. The number of modes in the cavity is $n = 2L/\lambda$ where λ is the the laser wavelength. For example, a cavity of 2 m in length will have approximately 5,000,000 modes for 800 nm light.

1.1.2 Gaussian Pulses

In general, a light wave can be described in the time domain with an amplitude, $F(t)$, and a phase factor relating the central frequency, ω_0, and a temporal phase, $\phi(t)$, such that

$$E(t) = F(t)e^{i(\omega_0(t)+\phi(t))} + c.c. \tag{1.1.1}$$

This discussion will focus primarily on the time domain description of the pulse. Further information on the description of focused Gaussian beams and their propagation and spatial structure can be found in [85]. The electric field in the frequency domain can be obtained by performing a Fourier transform in time and the resulting function will have an amplitude and phase as well. In the frequency domain, the amplitude and phase define a spectrum. The temporal width of a short pulse laser, $E(t)$, is then inversely related to the spectral width, $\tilde{E}(\omega)$, as shown in Eq. 1.1.2. The frequency domain function obtained from the Fourier transform is:

$$\tilde{E}(\omega) = \int_{-\infty}^{+\infty} E(t)e^{-i\omega t}dt = A(\omega)e^{i\varphi(\omega)} \tag{1.1.2}$$

where $A(\omega)$ is the real part of the spectral amplitude and $\varphi(\omega)$ is the spectral phase. These quantities form a description of the generation of ultrafast pulses in the oscillator. An example showing how the frequency spectrum broadens while the temporal profile narrows

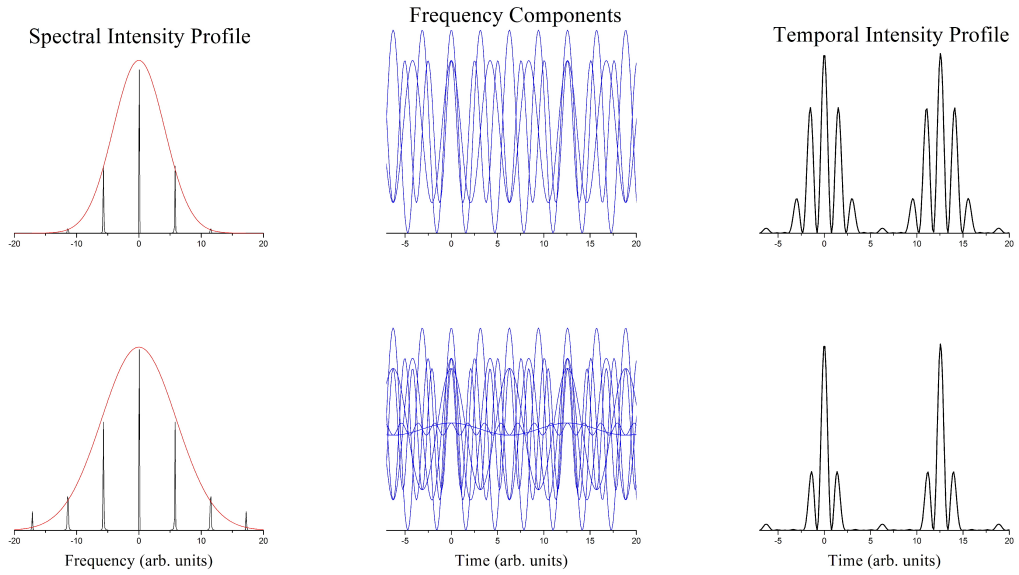

Figure 1.1.5: Example of the possible modes and frequency components in an oscillator to produce varying pulse durations centered around frequency ω_0 in arbitrary units for several amplitudes and frequencies. The more frequencies that are phase locked, the shorter the pulses may become in the time domain, with a corresponding broadening in the frequency domain. Constructive interference can be seen at times 0 and 12.5 in arbitrary units.

with the number of mode-locked frequencies is given in Fig. 1.1.5. The frequency spectrum is not continuous, but is composed of equally spaced spectral components each with a certain amplitude. This process is realized in mode-locked femtosecond laser systems as the frequencies within the cavity interfere constructively to form short pulses in the time domain.

The envelope functions $F(t)$ and $A(\omega)$ can be described by several forms including Lorentzian, exponential, hyperbolic secant squared, or Gaussian profiles. In practice, Gaussian profiles are often used as they represent the actual pulses very well and are easier to use in computational efforts where Fourier transforms of Gaussian profiles return Gaussian functions. As such, the following discussion will work with Gaussian envelope functions to describe several important features used in characterizing a laser pulse including power, intensity, spectral width (bandwidth), and pulse duration.

Defining the envelope functions for Eq. 1.1.1 and Eq. 1.1.2 as Gaussians and inserting them into those equations gives:

$$E(t) = F_0 e^{-2ln2(t/\tau)^2} e^{i(\omega_0(t)+\phi(t))} \tag{1.1.3}$$

$$\tilde{E}(\omega) = A_0 e^{-2ln2(\omega-\omega_0)^2/(\Delta\omega)^2} e^{i(\varphi(\omega))} \tag{1.1.4}$$

where F_0 and A_0 are the peak amplitudes of the envelope functions. The term $\varphi(\omega)$ is the spectral phase and is a constant for a transform limited pulse. This term would also contain information about the chirp or time dependent frequency information of the pulse. The pulse duration is defined as the full width at half maximum of the temporal profile, namely τ. The spectral width, or the bandwidth, is then defined as $\Delta\omega$. A Gaussian can be used to

describe the spatial dependence of a beam with waist w as:

$$E(r,t) = \sqrt{\frac{2}{\pi w^2}} e^{-(r/w)^2} E(t) = \sqrt{\frac{2}{\pi w^2}} F_0 e^{-(r/w)^2} e^{-2ln2(t/\tau)^2} \tag{1.1.5}$$

The power and intensity can now be described in terms of the electric field. Intensity is proportional to the modulus squared of the electric field in the time domain as defined in Eq. 1.1.3, $I \propto |E(t)|^2$. The peak power of a single pulse of energy, ρ, is then:

$$P_0 = \frac{\rho}{\int_{-\infty}^{+\infty} e^{-4ln2(t/\tau)^2} dt} = \rho \sqrt{\frac{4ln2}{\tau^2 \pi}} \tag{1.1.6}$$

For a Gaussian beam, the mode has an area of πw^2 and the intensity is two times the peak power, P_0, divided by the area of the beam:

$$I_0 = \frac{2P_0}{\pi w^2} = 4\sqrt{\frac{ln2}{\pi^3}} \frac{\rho}{w^3 \tau} \tag{1.1.7}$$

From Eq. 1.1.6, the peak power of the pulse can be increased by either increasing the energy in a single pulse or by decreasing the pulse duration (or similarly, increasing the bandwidth). As there is a repetition rate, R_{rep}, to the laser system, it is often useful to note the relation between the average power measured with a power meter for example, and the average single pulse power.

$$P_{avg} = R_{rep} \rho \tag{1.1.8}$$

Finally, another useful relation exists relating the bandwidth and pulse duration of the laser. This is the time-bandwidth product, $\tau \Delta\omega$ and it gives a minimum possible pulse duration

for a given spectral bandwidth. For the Gaussian pulses described above:

$$\tau\Delta\omega = 2ln2/\pi \approx 0.44 \tag{1.1.9}$$

Thus, for Gaussian beams, the time-bandwidth product is about 0.44. A similar formalism using other profiles would yield, for example, 0.315 for a hyperbolic secant and 0.142 for a Lorentzian function.

1.2 Strong Field Phenomena

The extremely short pulse durations of femtosecond lasers result in equally extreme intensities. Typically when discussing the interaction of atoms with strong external fields, the fields may not necessarily be "strong." If the field is not strong, then, for example, the Schrödinger equation can be solved using perturbation theory. For low intensity electric fields, the interaction of the atomic or molecular system with the laser light is linear in intensity and can be described with perturbation theory. Here, the laser field is treated as a perturbing force to the system, i.e., the internal field of the atom due to the nuclei is much stronger than the applied external field. The internal field for hydrogen corresponding to 1 a.u. is 5.14×10^9 V/cm, corresponding to an intensity of 3.5×10^{16} W/cm^2. Electrons are not easily ionized with a weak field and remain bound to the nucleus. With a strong laser field, however, ionization becomes more likely and many electrons may be removed from the atom or molecule. However, the high intensities produced by femtosecond pulses can be on the order of, or exceed, the atomic unit of intensity and thus perturbation theory is no longer applicable. The ionization processes are non-resonant and Stark shifts in the energy levels become important in describing the system as the potential surface can be

distorted by the strong field. In this regime, non-linear processes can become dominant and experiments become vital for a complete understanding.

1.2.1 Strong Field Ionization

Ionization of an atomic or molecular system with a strong field can be described several ways. Let us begin with a discussion of an atom subjected to a strong field. For a given bound state of the electron, there will be an associated amount of energy required to remove the electron from the potential of the nucleus. This ionization potential energy, I_P, is typically on the order of 10 eV and since optical light has photon energies from $\sim$1 eV to $\sim$3 eV, several photons may be required to ionize the electron from a bound state to the continuum. In xenon, for example, the ionization potential is 12.27 eV [2] and for iodine is 10.45 eV. Ionization of either one of the atoms would require absorption of multiple visible photons, a process called multiphoton ionization (see Fig. 1.2.1). By measuring the electron energy spectrum in xenon, it was found that the atom will absorb N photons required to ionize, but at high laser intensities there can be an additional absorption of photons in the continuum [2]. This strong field ionization in which an excess number of photons may be absorbed is known as above threshold ionization (ATI) and is reflected in the electron energy spectrum as a series of peaks of equal amplitude separated by the single photon energy.

A further description of strong field ionization can be developed in terms of the Keldysh parameter, γ, in Eq. 1.2.2 [3]. The Keldysh parameter is useful in describing three different regimes for strong field ionization including multiphoton ionization ($\gamma \gg 1$), tunneling ionization ($\gamma \ll 1$), and a combination of both ($\gamma \approx 1$). This parameter is defined as the ratio of the ionization potential in an atom or molecule to the energy of a free electron in an

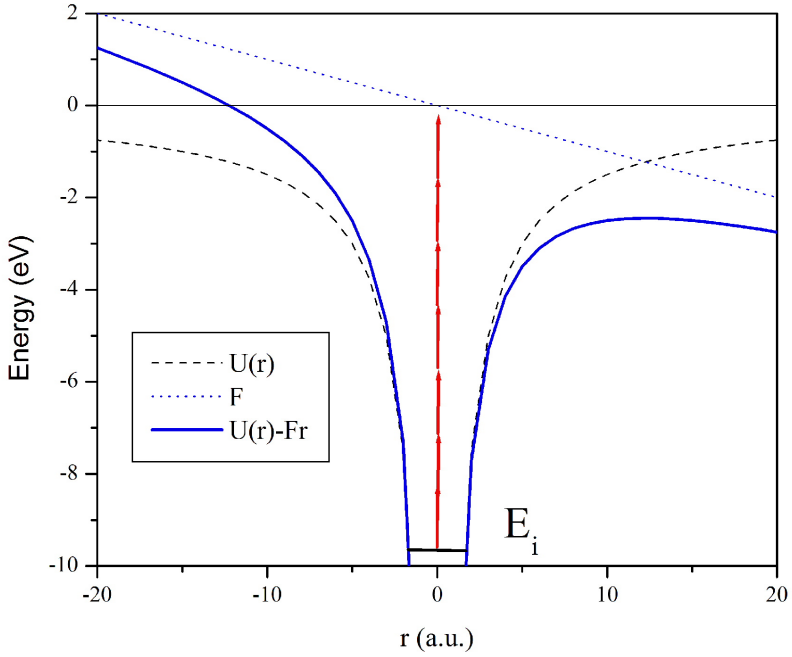

Figure 1.2.1: Coulomb potential, $U(r)$ for an atom in a strong field. E_i is the energy required to remove the electron from the bound state i. F is the applied laser electric field. The arrows (red) indicate the multiple photons needed for ionization.

electric field, the pondermotive energy. The pondermotive energy is the energy the electron will gain in the oscillatory electric field and can be defined as the following:

$$U_P = \frac{e^2 F_0^2}{4 m_e \omega^2} \tag{1.2.1}$$

where e is the charge of the electron, m_e is the mass of the electron, F_0 is the amplitude of the electric field, and ω is the frequency of the laser field. As the electric field strength increases, it distorts the potential well and can create a barrier through which the bound electron may tunnel. When the electron is in a time dependent, oscillatory field as is the case with an ultrafast laser pulse, quantum tunneling is possible if the time it takes for the electron to travel the length of the barrier (T_{tunnel}) is much shorter than the time it takes for the electric field to change direction ($T_{laserfrequency}$). Then the Keldysh parameter is also proportional these time scales and is defined as:

$$\gamma = \sqrt{\frac{I_p}{2U_P}} \propto \frac{T_{tunnel}}{T_{laserfrequency}} \tag{1.2.2}$$

In the case of multiphoton ionization when $\gamma \gg 1$, single photon energies are not enough to ionize atoms. The ionization potential may be several times the photon energy and the electric field frequency may be high (shorter wavelength) but with low intensity. The weak electric field will not create a significant distortion to the potential energy surface and the ionization will require the absorption of multiple photons in order to remove the electron from the atom or molecule. The rate of the ionization then scales with the intensity, I, and number of photons absorbed, n, as I^n. In this case, ionization in molecules proceeds much as it does in atoms.

Most fields used in strong field ionization are near IR ($\approx$ 800 nm, $\gamma \approx 1$) which is low frequency (long wavelength) and high intensity and the tunneling limit is typically a

good description for ionization. There is a probability for the electron to tunnel through the potential barrier into the continuum. For high enough laser intensities when $\gamma \ll 1$, this regime can result in a suppression of the barrier created by the electric field. The electrons energy may be below that of the energy barrier of the distorted potential and the electron will be ionized to the continuum by travelling over the barrier. All three of these descriptions are guidelines to aid in developing accurate descriptions of ionization and merely provide an order of magnitude scaling argument. Again, as much of the current work in ultrafast physics involves near IR lasers, ionization is often a combination of multiphoton and tunneling pictures. This is an active area of research in strong field physics in which new mechanisms for ionization are being realized, as will be discussed later on.

Laser intensities where the electric field begins to approach the internal field of the atom result in strong distortions to the atomic potential energy surface (Fig. 1.2.2). The barrier on the low energy side introduces a high probability that the electron may tunnel through the slowly varying potential to the continuum. A successful method for calculating the ionization rate of electrons in a strong field is the ADK (Ammosov-Delone-Krainov) model. This model treats the ionization rate, Γ, as that of a hydrogen-like atom in a static electric but can be extended to an oscillating field and more complex systems [5] such that:

$$\Gamma = |C_{n,l}|^2 \frac{(2l+1)(l+|m|)!}{2^{|m|}(|m|)!+(l-|m|)!} I_p \left(\frac{3F_0}{\pi\varepsilon_0}\right)^{1/2} \left(\frac{2\varepsilon_0}{F_0}\right)^{2n-|m|-1} exp\left(\frac{-2\varepsilon_0}{3F_0}\right) \qquad (1.2.3)$$

where $\varepsilon_0 = (2I_p)^{3/2}$ in atomic units is the intra-atomic field strength and the $|C_{n,l}|^2$ is a coefficient containing the principal quantum and orbital angular momentum values, n and l, respectively. It is important to note that Eq. 1.2.3 depends exponentially on both the ionization potential, I_p, and the amplitude of the electric field, F_0. In other words, the ionization rate of the atomic system will be highly sensitive to the electric field of the laser as well as

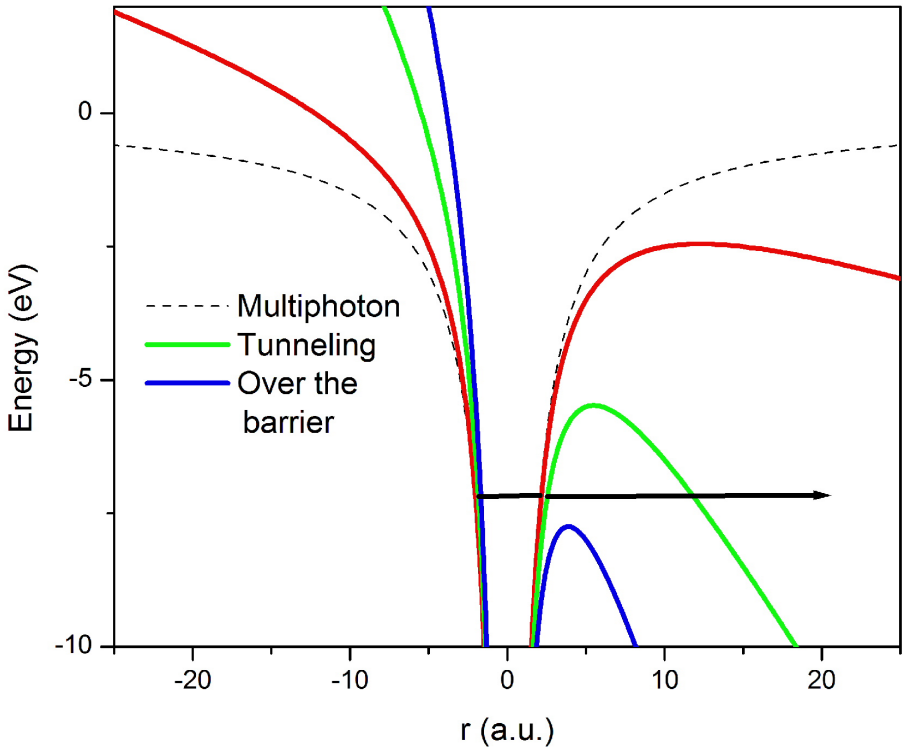

Figure 1.2.2: Distortions in the Coulomb potential for several electric field strengths from 0.1 to 1 atomic unit. For strong enough electric field, a barrier is created on the low energy side of the potential and the electron has a probability for ionization through tunneling.

the ionization potential. Small changes in the field strength will result in noticeable changes in the observed ionization rate. For example, when ionizing a system with an asymmetric electric field, one in which the amplitude is different in one direction compared to the other, the ionization rate will directly reflect the orientation and magnitude of the field. This will be discussed later on. The ADK model does not predict some interesting phenomena which occur in molecules such as ionization as a function of internuclear separation, although it has still been met with success when applied to modeling ionization in atom-like molecules where a single electron picture of ionization is a good approximation.

1.2.2 Enhanced Ionization

Studying ionization in molecules is more complex due to the additional degrees of freedom of rotational and vibrational motion as well as multi-electron effects. In diatomic molecules, the potential energy structure can be described by a double-well potential with the centers of each well at the site of each nucleus. The separation of the wells is the internuclear distance, R, and this degree of freedom can exhibit nuclear vibration for bound electronic states as well as change the structure of the double-well as the nuclei undergo dissociation due to ionization. Just as the atomic well is distorted by the strong field as described above, the double-well potential of the molecule has changing features as a function of internuclear distance in the presence of a strong field (Fig. 1.2.3).

One particular phenomenon in the strong field ionization of molecules is the observation of large enhancements in the ionization rate as dissociation occurs. It has been found experimentally in I_2 [18], for example, that the ionization rate peaks when the nuclei are at about twice the equilibrium distance, R_e, of the molecule at a critical separation, R_c. Further, the effect is only seen by probing with polarizations parallel to the internuclear

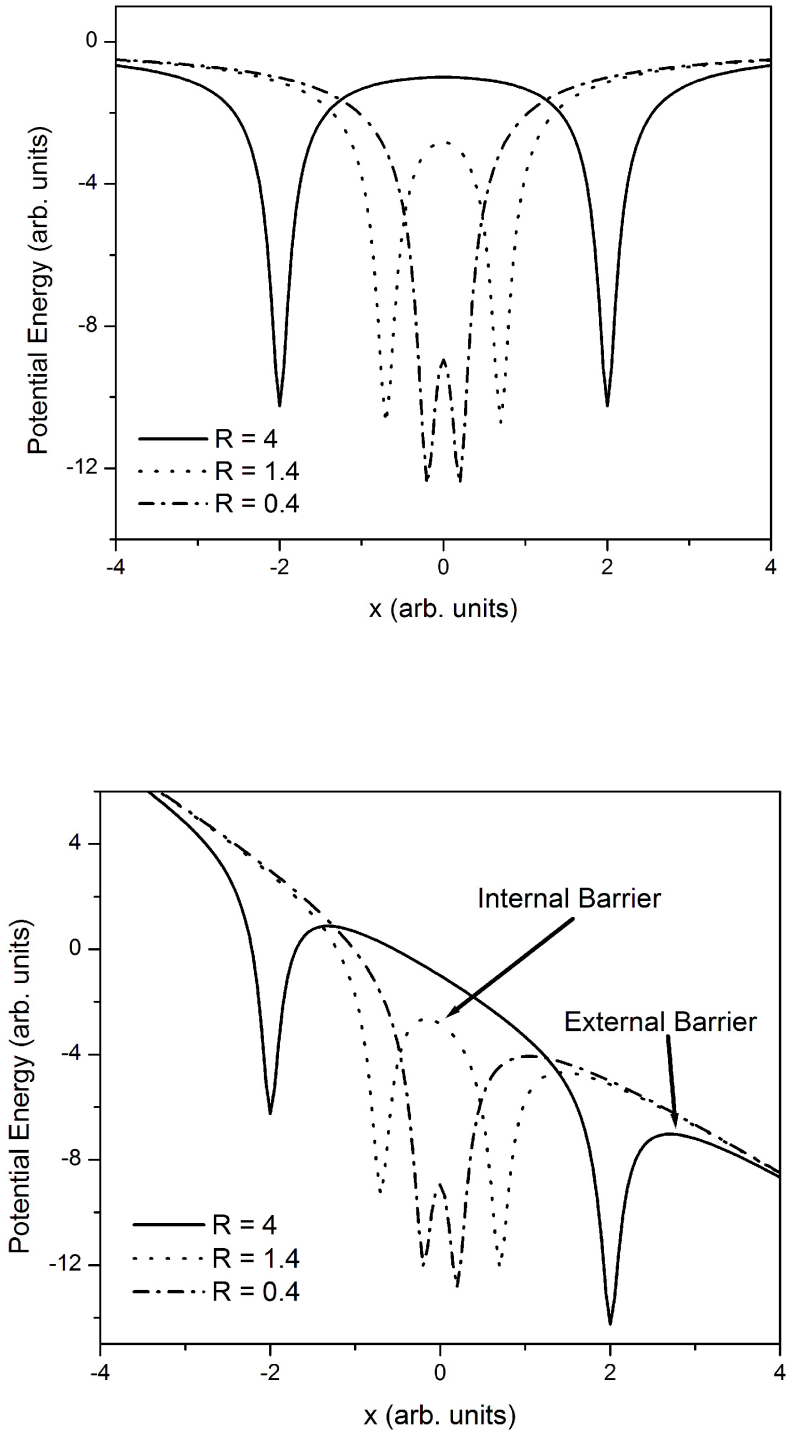

Figure 1.2.3: Schematic of the electronic double-well potential for several internuclear distances $R = 2d$ in the absence of the electric field (top) and in the presence of the electric field (bottom). The electron coordinate is x and the nuclei are located at $\pm\, d$.

axis with the peak dissappearing when probed with perpendicular polarization. This has also been observed for an excited state of I_2 in the work appearing in [59]. The proposed mechanism is explained by electron localization as the molecule extends in R [53].

An electron may move between the two wells as it responds to the strong laser field applied along the internuclear axis. This charge resonance (CR) mechanism was first proposed by Mulliken [26] and gives rise to a mechanism called charge resonance enhanced ionization in which a pair of charge resonant states are strongly dipole coupled to the applied laser field at large R with a dipole moment that diverges linearly as $R/2$ where the energies are nearly degenerate [17]. This is the subject of Chapter 2. The ionization of a molecule depends strongly on the internuclear separation due to the internal barrier such that at small separations the energy of the internal barrier is lower than the electronic ground state energy (the dashed-dotted curves in Fig. 1.2.3). Here, the ionization is atom-like as the electron experiences only the external barrier (lower potential energy side) through which tunneling may occur. At much larger separations (the solid curves in Fig. 1.2.3) there is a broad internal barrier between the two wells and again, the ionization behaves similarly to that of an atom as the electron cannot move easily between the two nuclei. An electron may then tunnel through potential barriers which are atom-like. At intermediate separations (dotted curve), around R_c, there is a nonadiabatic localization of the electronic wave function in the upper energy well, trapping the population. The ionization in this regime can be enhanced dramatically compared to atoms since the electron may now tunnel through the narrow internal barrier directly to the continuum. This mechanism will be revisited in the coming chapters and an interpretation for two electrons in a double-well will also be discussed.

1.3 Non-Linear Optics

The ability to produce such high intensities with laser light made it possible to examine new phenomena in the response of matter to light. For example, some properties of light propagating through dielectric media such as glass or crystal can be described by the index of refraction, n, of the material. At high enough intensities of optical light, I, the index of refraction may have non-negligible higher order terms taking the form of Eq. 1.3.1

$$n = n_0 + n_2 I(r,t) \tag{1.3.1}$$

where n_0 is the linear index of refraction and n_2 is the nonlinear refractive index. As the intensity is proportional to the square of the electric field strength, Eq. 1.3.1 is a nonlinear phenomenon. Nonlinear effects as a result of this intensity dependence include the Kerr effect, self phase modulation, and self focusing. This may occur, in general, for any dielectric material given a high enough intensity, although the magnitude of the nonlinearity may be quite small, or zero, for different materials depending on their structure as will be discussed below.

Although nonlinearities could be predicted by optics before the invention of the laser, there was no source of light intense enough to experimentally observe nonlinear effects. In 1960, along with the development of the ruby optical maser, Franken was able to produce for the first time an observable optical nonlinear response to high intensity light in the form of optical harmonics ([1]). Franken and coworkers used an optical maser at 694 nm incident on crystalline quartz to produce light at the second harmonic (347 nm). As noted above, all dielectrics are nonlinear with high enough field strength, so quartz was an obvious choice to use given that it was a readily available and inexpensive material. Still, in order to have

a nonlinear response to the incident light, the material must have a nonlinear dielectric coefficient and be transparent to both the fundamental and harmonic light. It is the atomic structure and lattice configuration of the material that will dictate whether nonlinearities are possible. In order to describe this process, the following discussion is presented, with particular focus on second harmonic generation (SHG). High intensity lasers can produce interesting nonlinear effects in materials which can be used to produce ultrafast pulses.

The intensity of a laser beam in Eq. 1.3.1 has a spatial and temporal dependence. For a positive n_2, the index of refraction becomes larger at the center than at the edges and the gain medium behaves similarly to a converging lens. This leads to self focusing of the beam like a converging lens and is a spatial phenomenon. As the intensity increases, the self focusing can become stronger as well. The tighter focusing of the beam results in little loss through the gain medium and mode locking can be achieved when most of the available energy is concentrated in a single pulse. The mode locking may not occur spontaneously, but can be started by applying a perturbation to the system such as touching a mirror or prism in the cavity. This type of mode locking is used in our oscillator and is a result of self focusing known as Kerr lens mode-locking. There is also a temporal component to the intensity profile which can lead to spectral broadening of the pulse through the gain medium. This effect is self phase modulation and is related to the compression of the laser pulses and the pulse duartion.

1.3.1 Second Harmonic Generation

In the classical theory of light propagating as a wave, the polarizability can be described as the average induced dipole moment of the medium due to the external electric field. The polarization induced by an electric field is related to the electric susceptibility of the

medium, as in Eq.1.3.2:

$$\vec{P}(t) = \chi \vec{E}(t) \tag{1.3.2}$$

where χ is the susceptibility and $\vec{E}$ is the electric field. More generally the susceptibility is a tensor with both zero and non-zero components describing the response to the electric field. This is for a description of a linear response, but the polarization can be expanded in a power series in the electric field as

$$\vec{P}(t) = \chi^{(1)}\vec{E}^1(t) + \chi^{(2)}\vec{E}^2(t) + \chi^{(3)}\vec{E}^3(t) + ... \tag{1.3.3}$$

$$\vec{P}(t) = \vec{P}^1(t) + \vec{P}^2(t) + \vec{P}^3(t) + ... \tag{1.3.4}$$

where $\chi^{(i)}$ are the ith order nonlinear susceptibilities and $\vec{P}^i$ are the linear and nonlinear polarizations. For the remainder of this section, let the polarization and electric fields be scalar quantities as it does not detract from the discussion. We may then define the electric field as:

$$E(t) = Ee^{i\omega t} + E^* e^{-i\omega t} \tag{1.3.5}$$

where ω is the frequency of the fundamental or incident radiation. The second order contribution to Eq. 1.3.3 is then found by using Eq. 1.3.5 in Eq. 1.3.6

$$P^2(t) = \chi^{(2)}E^2(t) \tag{1.3.6}$$

$$P^2(t) = 2\chi^{(2)}EE^* + \chi^{(2)}E^2(e^{2i\omega t} + c.c) \tag{1.3.7}$$

$$P_{2\omega} = \chi^{(2)}E^2 \tag{1.3.8}$$

where $P_{2\omega}$ is the amplitude of the second order nonlinearity which is shown to be a wave oscillating at the second harmonic frequency, 2ω. Now, in order for this to be nonzero, $\chi^{(2)}$

must be nonzero. Up to this point there has been no consideration of the material itself. However, the structure of the material now becomes important in terms of the susceptibilities.

Media may be symmetric under inversion if a particle at position $\vec{r}$ sees the same location and distribution of surrounding particles as a particle placed at - $\vec{r}$ as in Fig. 1.3.1. Crystal structures may lack this inversion symmetry, while liquids and gases are symmetric under inversion. For centrosymmetric media, $\vec{P}$ = - $\vec{P}$ and $\vec{E}$ = - $\vec{E}$. The symmetry dictates that these centrosymmetric media will have no contributions from even-order terms in Eq. 1.3.3. The lowest order nonlinearity in a centrosymmetric medium is then the third order, χ^3 term. This is the case for a pair of atoms. In order for a material to be capable of producing second harmonics, it must lack a center of inversion with respect to the atomic structure. A bulk media can lack inversion symmetry and in this case the lowest order nonlinearity would be χ^2, which is the component related to the second harmonic. This term is also proportional $\left|\vec{E}\right|^2$ and is the relevant contribution for SHG. These types of materials are called noncentrosymmetric (as shown in Fig. 1.3.2).

The potential, $U(x)$, felt between a pair of atoms in the lattice structure must have some anharmonicity such that $U(x)$ is different from $U(-x)$. Consider the lattice in Fig. 1.3.2. If particle A is displaced from equilibrium towards particle B, it will experience a repulsive force which pushes it back towards particle C. Particle C will also attract particle A. As particle A moves along a line between B and C, it will experience a restoring force with a different size and direction which can be described by the potential energy of particle A as shown in Fig. 1.3.2. As particle A moves a distance x between B and C the potential will not be symmetric about the equilibrium position and the material lacks a center of symmetry. The anharmonic potential, from a classical stand point, will lead to a nonlinear restoring force when the lattice is perturbed by the intense field. The lowest order nonlinearity in

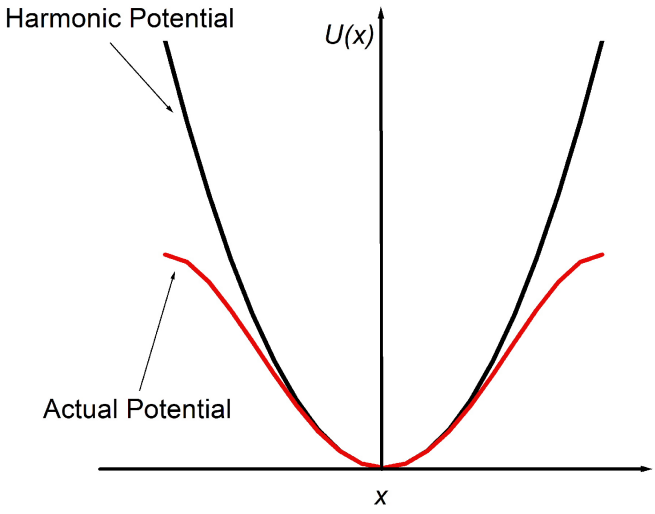

Figure 1.3.1: Potential energy schematic for centrosymmetric materials. In a harmonic potential, the inversion symmetry is preserved.

the polarization is then $\chi^{(2)}$. This is a global property of the material and makes second harmonic generation possible.

Some common materials used for SHG are beta barium borate (BBO) and potassium dihydrogen phosphate (KDP). These materials can produce radiation at the second harmonic with efficiencies of 30 - 60% depending on the beam structure and the thickness of the crystal. Gaussian beams can often produce efficiencies greater than 60% when focused and higher efficiencies are often achieveable with thicker crystals as the efficiency goes $\sim L^2$, where L is the thickness of the crystal. Maintaining proper phase matching of the $\vec{k}$ vectors of the incident and nonlinear light is important for producing strong SHG and using ultrafast pulses may require thinner crystals.

1.3.2 Asymmetric Two-Color Fields

Combining a laser field with its second harmonic in a phase coherent manner can produce an electric field which is spatially asymmetric (Eq. 2.2.1). A field of this type has a greater peak field in one direction than the other and is referred to as an asymmetric field (Fig. 1.4.1). These asymmetric fields are useful in strong field physics as processes such as ionization are typically sensitive to peak field intensity. Even small asymmetries in the field will be exaggerated leading to a spatial control of ionization and ion yields. Further, strong fields can excite states that lead to charge asymmetric dissociation channels and the asymmetric field can probe these channels.

The spatial control can be described by considering a molecular ion $A_2^{(n+m)+}$, where n and m are intergers. We can treat the potential as a double well, as described above, where the left well has n ionized electrons (or holes) and the right well has m ionized electrons. Ionization of this molecule can result in dissociation into ionic fragments such

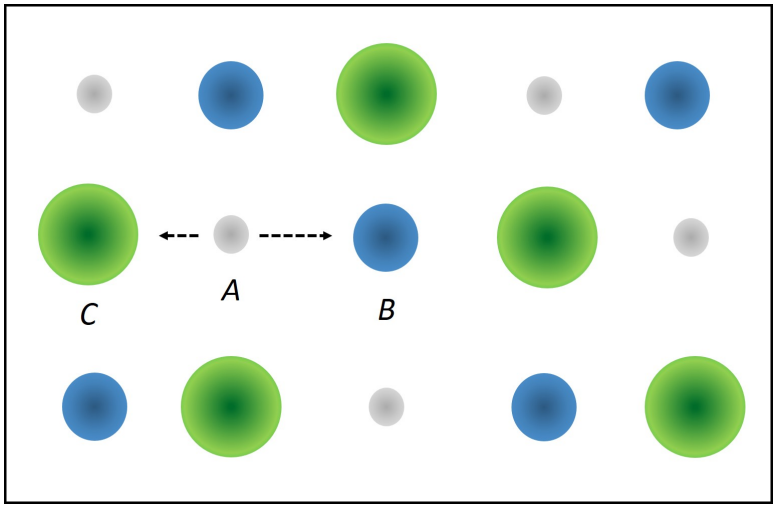

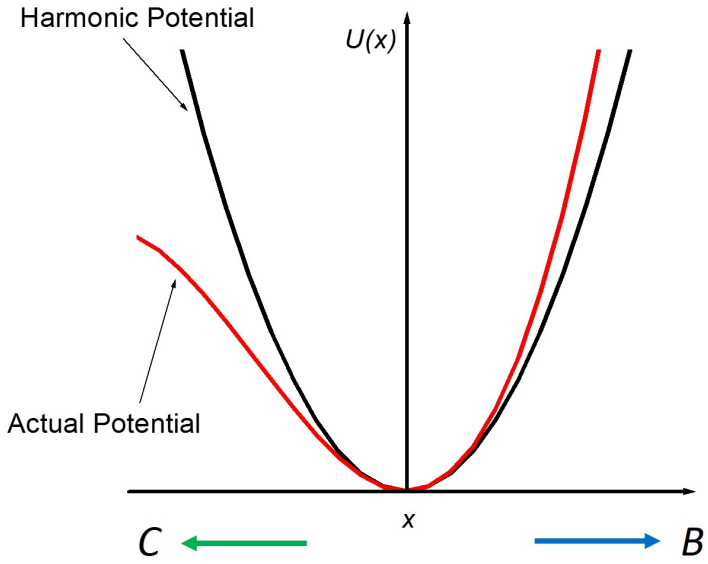

Figure 1.3.2: (Top) Lattice structure of a crystal which lacks a center of symmetry with particles A, B, and C. (Bottom) As particle A is displaced a distance x toward particle B, it experiences a weaker restoring force than moving the same distance towards C.

that $A_2^{(n+m)+} \rightarrow A^{n+} + A^{m+}$. The fragments may therefore be asymmetric as n and m can be different from each other. As an example, let $n = 2$ and $m = 0$, then $A_2^{2+} \rightarrow A^{2+} + A^0$ which we label as (2,0) (2+ on the left well, 0 on the right). With the convention of n for the left well and m for the right, this fragmentation is characteristic of an ionic fragment of charge 2 and another with neutral charge. In a time of flight experiment, there is an ensemble of molecules which will ionize and be detected. Energetically, there is no difference between $A_2^{2+} \rightarrow A^{2+} + A^0$ (2,0) and $A_2^{2+} \rightarrow A^0 + A^{2+}$ (0,2), i.e., the right or left well of the potential. Both kinds of ionic fragments will be detected at the same time of flight and the spatial information about how the fragmentation is occuring will be lost. However, the asymmetric field can preferentially ionize one well over the other thus differentiating between (2,0) and (0,2) and breaking the symmetry. This laser field can break the spatial symmetry of the interaction, which, in turn, can lead to a spatial asymmetry in the dissociation of the ionic states. This is the topic of Chapter 3 and will be discussed in detail there.

The magnitude and direction of the two color field are controlled by varying the relative phase between the fundamental and second harmonic to produce varying asymmetric fields,

$$E(t) = E_\omega(t)cos(\omega t) + E_{2\omega}(t)cos(2\omega t + \phi), \tag{1.3.9}$$

where ϕ is the relative phase between the pulses and E_ω and $E_{2\omega}$ are the envelopes of the fundamental and second harmonic, respectively. The fundamental is generally of larger amplitude than the second harmonic, although the ratio of $E_\omega/E_{2\omega}$ can be somewhat controlled. Coherently combining these two frequencies at a given relative phase will result in an electric field which is spatially asymmetric. When the relative phase is $\pi/2$, the combined field is symmetric, while the maximum asymmetry occurs at $\phi = 0$ and π (Fig.

1.4.1). The measured ion yields will reflect this asymmetry in time of flight, for example, resulting in more ions going toward the detector than away. An example of a time of flight measurement is given in Fig. 1.4.2.

1.4 Dynamics in Molecules

The application of a strong field to a molecular gas in high vacuum, for example, can lead to ionization of multiple electrons, weakening the bonds of the molecule. This pump pulse can dissociate the molecule into ionic fragments and the momenta and charge states of these fragments can then be detected in the laboratory through various methods. By using a second pulse with a variable time delay from the first, we can probe the dynamics as a function of time, or equivalently, internuclear separation. This method of pump-probe spectroscopy will be used throughout the experiments described in this thesis. The pulses allow for measurement of vibrational periods of different states, ionization as a function of internuclear separation, and control over electronic vibrational wavepackets as well as any dynamics which may occur as a function of time such as enhanced ionization and charge transfer.

1.4.1 Vibrational Wavepackets

Molecular vibrational levels are described by eigenenergies, E_n, and eigenstates, ϕ_n, and are defined by the dynamic interaction of the electrons with the nuclei. In a field-free system, the potential energy surface will have some number of bound vibrational states with each possessing an associated energy and phase. Electronic population can be in any of these eigenstates and can also be distributed amongst many states. An ultrafast laser

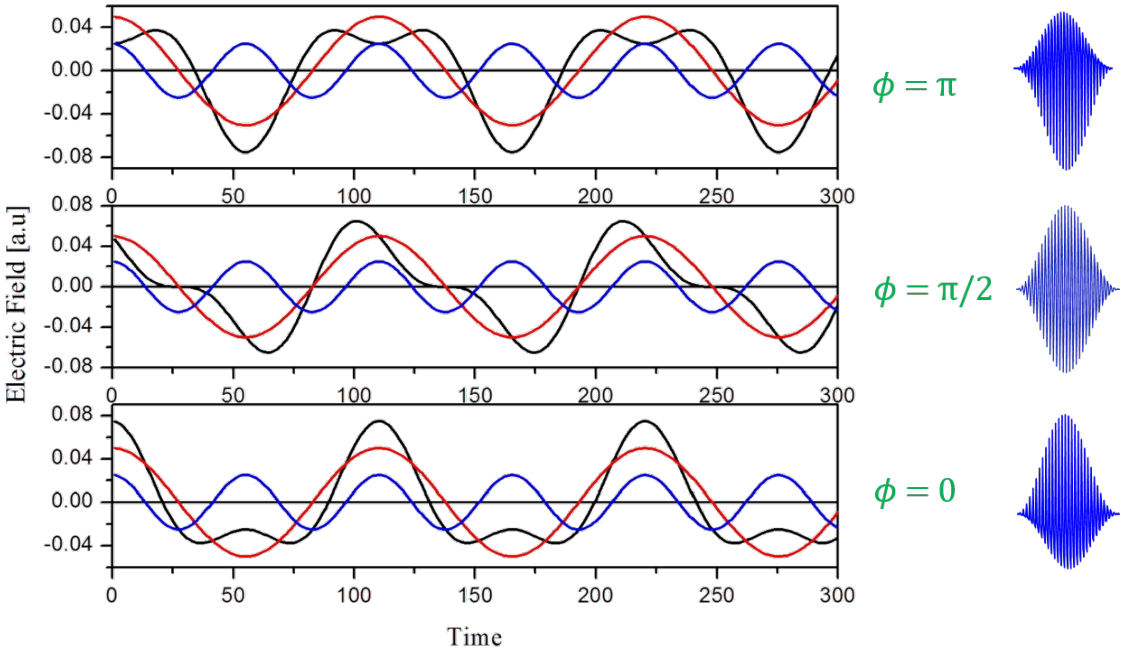

Figure 1.4.1: Electric field produced through superposition of the fundamental and second harmonic at several relative phases of the two-color field.

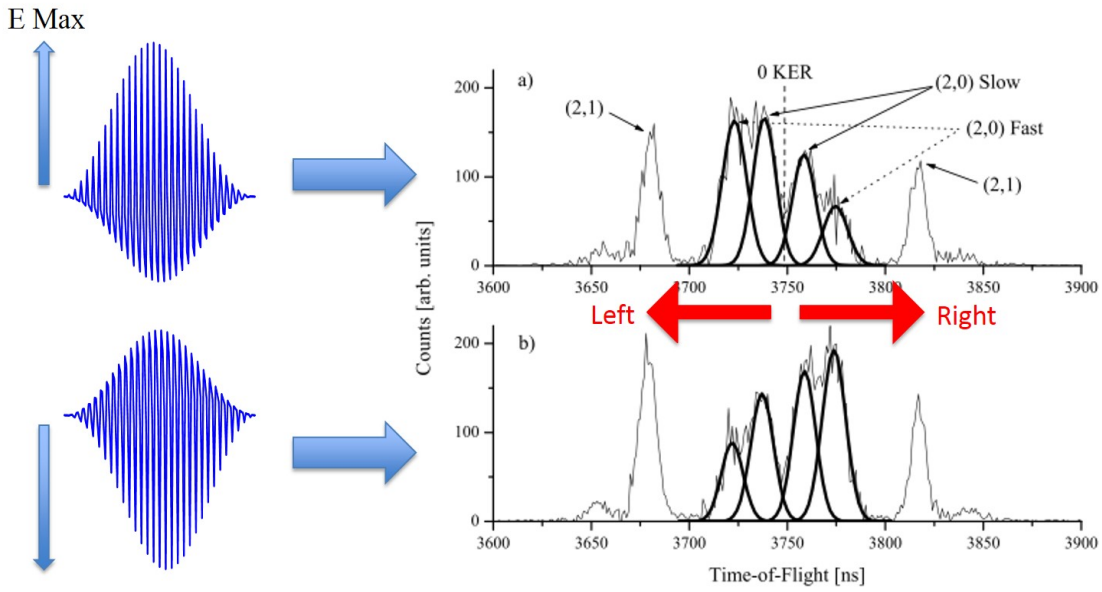

Figure 1.4.2: Example of asymmetric ion yields measured with a two-color asymmetric laser pulse at two relative phases, ϕ. The ions at earlier time of flight (left, toward the detector) have a different yield than those at later time of flight (right, away from the detector).

pulse, due to its broad bandwidth, is capable of coherently exciting many eigenstates at once creating a coherent superposition of these eigenstates with a well defined phase. The result of ionizing with a strong field laser is the production of a vibrational wave packet. A vibrational wavepacket can be defined as:

$$\Psi_{vwp}(R,t) = \sum_n C_n e^{-iE_n t/\hbar} \phi_n(R) \tag{1.4.1}$$

where the temporal information is contained in the phase $e^{-iE_n t/\hbar}$ and the spatial information is in the eigenstates of the field-free system, ϕ_n. The coefficients C_n are the projections onto the n^{th} eigenstate and $|C_n|^2$ are the populations in the eigenstates. The energy spacing of the vibrational levels is small, around 0.013 eV for I_2 in the ground state. Therefore, resonant excitations between levels of a potential require extremely narrow bandwidth to occur. The broad bandwidth of an ultrafast laser excites many levels simultaneously through nonresonant processes and the strength of the field can modify the coherence. When the excitation of the system is coherent, as is the case with a laser, the phases between the eigenstates are coherent resulting in a wave packet. For example, the thermal energy at room temperature (0.025 eV) is enough to begin to vibrationally excite I_2. However, this excitation is not coherent and the phases of the eigenstates are random so that any vibrational motion averages out (although can raise the average vibrational energy) so no wave packet is formed.

A wave packet can be produced in an electronically excited state after ionization. The strong laser field with high intensity can excite many vibrational states through nonresonant processes. In this case, ionization can be described as a direct projection of the initial wavefunction onto an upper electronic state. The vibrational wave packet produced by the laser depends on "projecting" the ground state amplitude by a Franck-Condon vertical transition onto an excited electronic state. From there, the wave packet evolves in time on the

excited state potential. The wave packet can then be detected through either dissociation or vibration if it is produced in a bound upper state. If the projection of the inital wavefunction is onto a dissociating state, the molecule will come apart in fragments whose energy depends on R. The dissociation energy of the process, if the fragments are ions, can then be measured in a time of flight detector, for example. Wave packets can also be produced in bound regions of a potential. The vibrational motion is a result of producing a wave packet which is perturbed from the equilibrium position of the molecule. In this case, the wave packet will oscillate in the well at a frequency which is characteristic of the potential it is occupying. The motion of the wave packet therefore carries information about the structure of the potential.

If the well is harmonic in structure, as is approximately the case near the minimum potential energy region, the wave packet will oscillate for long periods of time as there will be little dephasing of the wavepacket during each period of oscillation. This has been seen in the process of Lochfrass, or R-dependent ionization, of the ground state of I_2 in which strong field ionization creates a coherent hole in the wavefunction. The vibration of the hole created in the wavefunction can be observed for dozens of cycles with very little dephasing with a period of 6.3 THz or about 159 fs [39]. A real potential well is anharmonic such that the restoring force is nonlinear compared to a linear restoring force for a harmonic potential. This anharmonicity results in a dephasing of the wave packet as it vibrates in the potential well (Fig. 1.4.4) as the components near the bottom of the well have a shorter period than those higher in the well. The amplitude of the wave function decreases as a function of time as the eigenfunctions it is composed of become out of phase and detecting the wave packet through ionization, for example, becomes difficult as signals become quite weak. The ionization of electrons with the strong field on ultrafast, femtosecond time scales results in a ”freezing” of the nuclear motion such that ionization

occurs at a single internuclear separation R. By applying a second, time delayed ultrafast pulse, dynamics can be probed as a function of time which can be mapped to R. Since the laser pulse duration is much less than the vibrational period, a femtosecond pulse is an excellent tool for studying dynamics in molecules such as ionization and dissociation as a function of R.

1.4.2 Pump-Probe Spectroscopy

Since an ultrafast pulse is typically around 30-50 fs, it is ideal for studying dynamics in molecular systems. The time scale of nuclear motion and chemical reactions is in the femtosecond regime. Diatomic molecules have vibrational periods ranging from a few femtoseconds in light molecules ($\approx$ 8 fs in H_2 and $\approx$ 12 fs in N_2) to hundreds of femtoseconds in heavier molecules ($\approx$ 150 - 700 fs in I_2). As the molecule vibrates or dissociates as a function of time, it can be probed by another time delayed laser pulse. This pump-probe technique is used throughout this dissertation to study iodine, I_2.

A schematic of the experimental setup is given in Fig. 1.4.3. The beam is split by the first beamsplitter and recombined at the second. There are now two identical pulses which can be used in a pump probe measurement. Since they are on separate paths, the intensity and polarization of the beams can be controlled independently allowing for both dependencies to be explored in an experiment. The spatial overlap of the beams is optimized with a camera or by focusing through a small pinhole and optimizing the transmitted power of each. Temporal overlap can be optimized by measuring the interference pattern (for beams of the same wavelength and polarization) or also by an ion signal in the chamber. As shown in Fig. 1.4.4, when the beams have no time delay between them (0 delay, or T_0) there is a large enhancement in the ion signal as the intensity is much higher when overlap occurs.

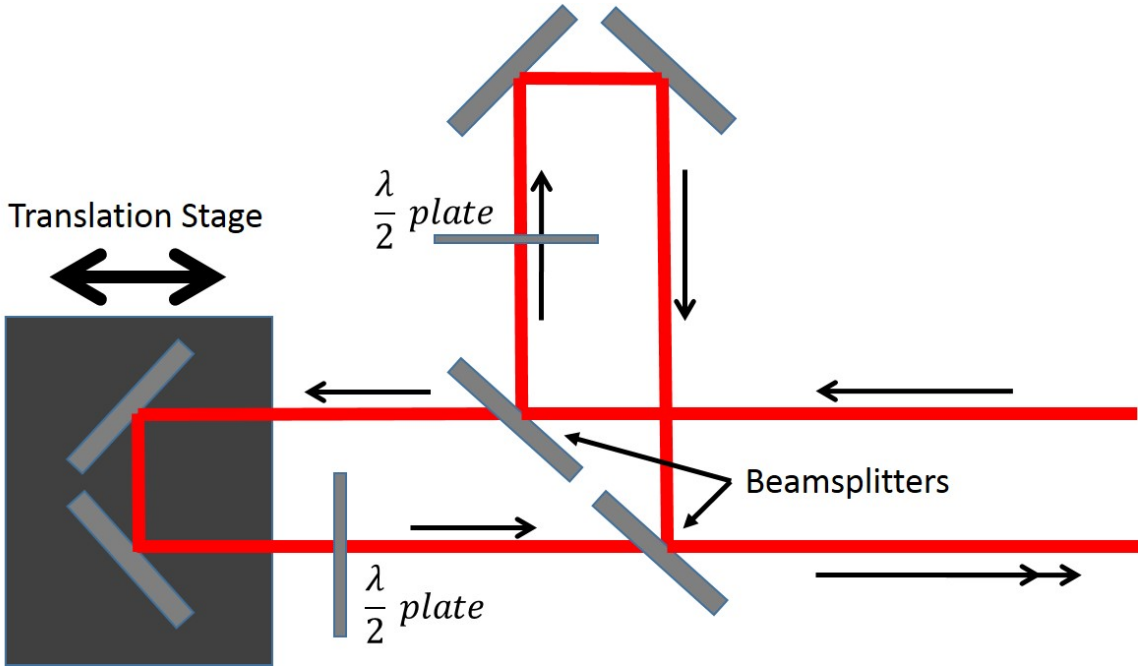

Figure 1.4.3: Schematic for a pump probe experiment. The translation stage controls the time delay between the two pulses. The wave plates control the polarization of each pulse individually.

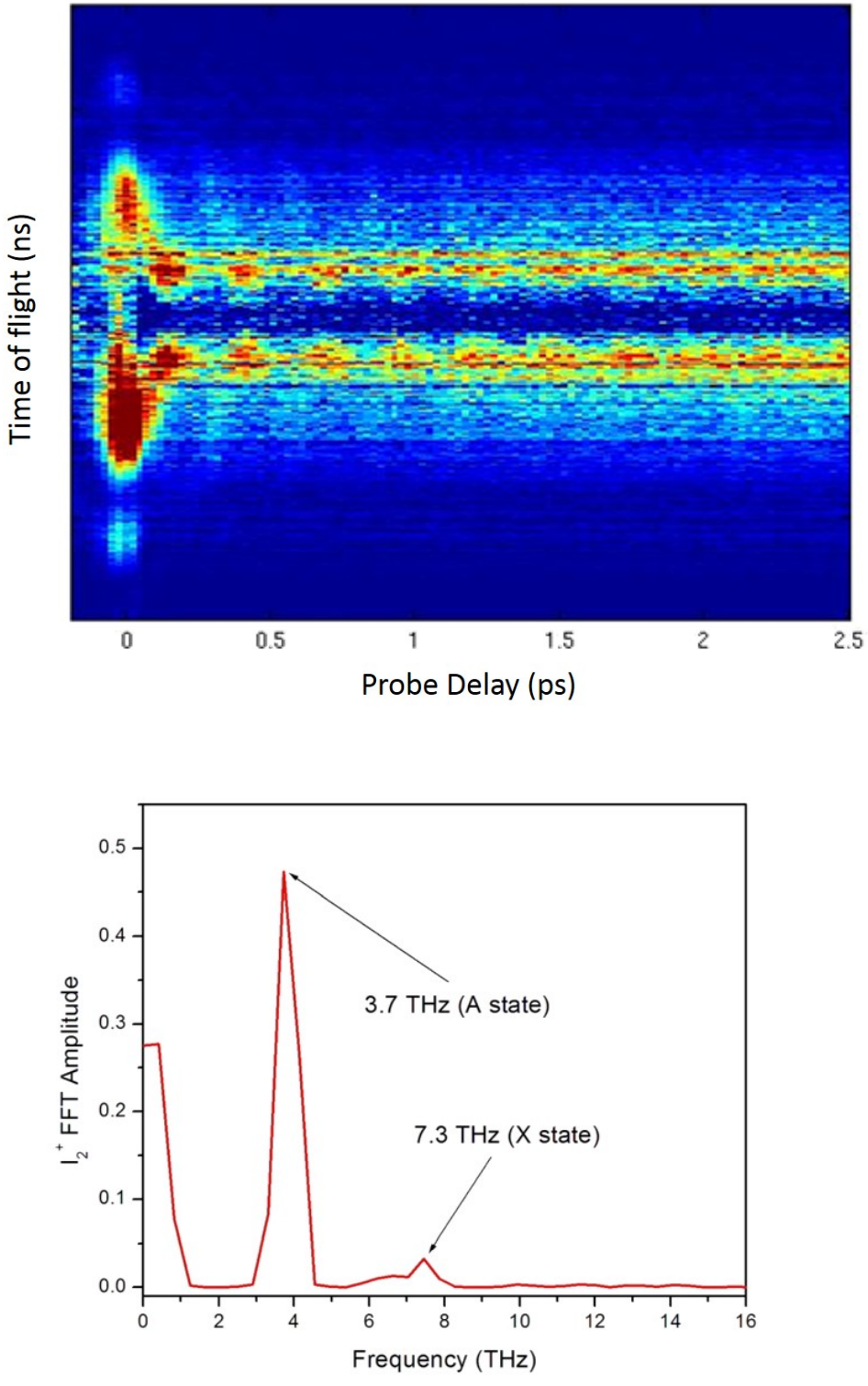

Figure 1.4.4: Example time of flight pump-probe data examing vibrational motion of a wave packet in the ground (X) and excited (A) states of I_2^+. By performing a Fourier transform of the ion signal, two periods are identified. The A state has a period of about 270 fs (3.7 THz) and the X state has a period of about 150 fs (7.3 THz). This is the subject of Chapter 5.

Fig. 1.4.4 is an example of a typical pump probe time of flight measurement of a vibrational wavepacket in iodine (I_2). In this example, the pump pulse first ionizes the neutral I_2 creating a wavepacket in the ion. As will be discussed in Chapter 5, the pump ionization step may remove multiple electrons, and while the general assumption is that the ion will be left in the ground state, it is also possible that the ion will end up in an excited state [49, 64]. The coherent evolution of the wave packet produced in the potential well of the ion can be measured by applying a second, time delayed short pulse (probe). The probe pulse may then transfer the wave packet population by coupling to dissociating states resonantly or directly through nonresonant processes, such as ionization. The kinetic energy release (KER) of the dissociating ionic fragments is dependent upon where in the potential well ionization occurs. Since R can be determined from the probe delay time for well known potential curves, any observed periodicity in the KER will map out the vibrational motion of the wave packet. The frequency of the vibration can then be used to identify the state being probed. This method can also be used to determine energies of unknown potential curves as in [38].

1.5 Experimental Techniques

1.5.1 Time of Flight

In the following ongoing and proposed experiments, molecular dynamics of ionization and ion fragmentation are examined using a time of flight (TOF) mass spectrometer or a velocity map imaging (VMI) detection system and pump-probe spectroscopy. First, iodine is introduced into the vacuum chamber effusively from a stainless steel bulb. In the TOF configuration, the laser pulses are focused by a spherical mirror to a spot size of $\sim 50\ \mu$m,

resulting in the high intensities needed to ionize the molecule. Ions are then detected using a typical Wiley-McLaren TOF spectrometer [43]. Once the ions are produced they are extracted by a dc electric field of 223 V/cm through a 1 mm pinhole and accelerated by an additional 800 eV. They are then sent through a 10 cm field-free drift tube giving both symmetric velocity dispersion and high resolution. A microchannel plate is used to detect the ions and the signal is amplified, discriminated, sent to a time-to-digital converter and then readout to a computer. The molecules in the TOF chamber are at room temperature with a pressure of around $1\text{x}10^{-6}$ torr and a base pressure around 10^{-9} torr.

As the fragmentation occurs, only ions whose internuclear axis is aligned with the TOF axis are collected. A small pinhole prevents most off-axis ions from reaching the detector (Fig.1.5.2). For each dissociation event with the molecule aligned along the TOF axis, there is a forward and backward going fragment which correspond to fragmentation with the initial momentum toward or away from the detector, respectively. The resulting TOF spectra for a particular dissociation channel consists of two peaks which are symmetric about the arrival time of the zero-kinetic-energy ion. The separation of the peaks is proportional to the initial momentum of the dissociating fragments (Eq. 1.5.2) and the kinetic energy release (KER) (Eq. 1.5.3). The mass-to-charge ratio of the fragments dictates how long they will travel in the TOF tube until reaching the detector as is described by Eq. 1.5.1. Therefore, for a given species of nuclei, a higher charged ion will reach the detector faster than a lower charged ion. Once the calibration, A, and offset, T_0, are known, one can predict the time of flight of any ion based on the mass-to-charge ratio and Eq. 1.5.1.

$$T = T_0 + A\sqrt{m/q} \tag{1.5.1}$$

where T is the time of flight, A is the calibration, and m and q are the mass and charge of

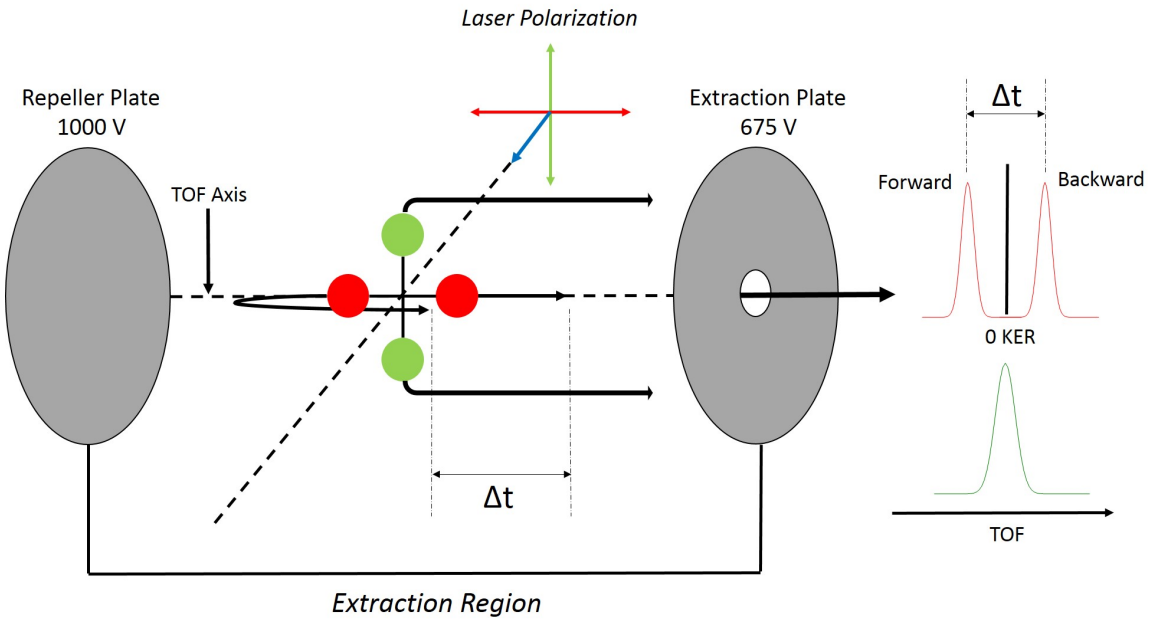

Figure 1.5.1: Schematic of the time of flight setup. The laser polarization can be parallel or perpendicular to the time of flight axis resulting in dissociation along the polarization direction. When polarized parallel to the axis, fragmentation occurs along the axis with ions going forward or backward relative to the detector. The amount of time it takes the ion to turn around in the extraction region, Δt, is proportional to the KER of the dissociation event and is seen as two separate peaks in the TOF separated by Δt.

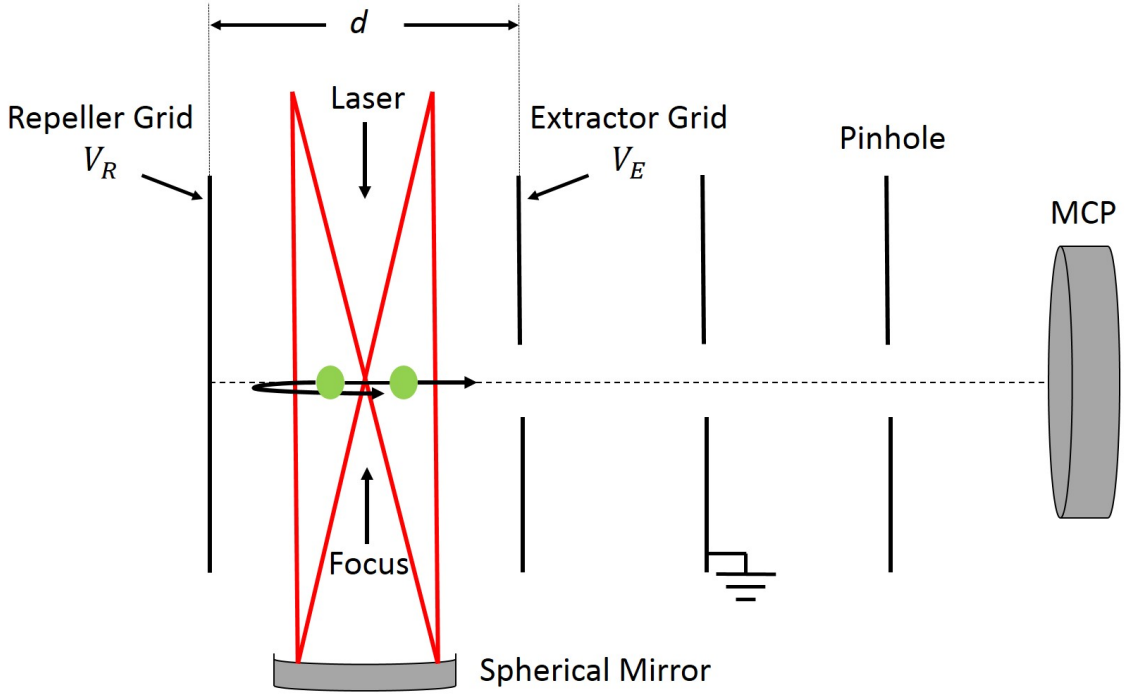

Figure 1.5.2: Time of flight chamber. The repeller and extractor grids are separated by a distance d.

the ion in atomic mass units (amu), respectively. This results in a TOF spectrum for various ionic fragments, an example of which is shown in Fig. 2.2.3. For example, if A = 465 ns and T_0 = 0, the time of flight for the detected ions is then 7410 ns for I_2^+, 5240 ns for I^+, and 3705 ns for I^{2+}.

The momentum and KER can be found from the time of flight parameters and the measured time separation of a pair of dissociating peaks, Δt:

$$P = \frac{(V_R - V_E)q}{2d}\Delta t \tag{1.5.2}$$

$$KER = \frac{P^2}{2m} = \frac{(V_R - V_E)^2 q^2}{4md^2}(\Delta t)^2 \tag{1.5.3}$$

Here, V_R and V_E are the repeller and extractor voltages, respectively and d is the separation of those plates. These relations arise from the kinematics of the charged particles in the electric field of the extraction region between the plates.

1.5.2 Velocity Map Imaging System

To acquire new information about ion fragmentation and dissociation, a velocity map imaging (VMI) system may also be used. The VMI differs from the TOF as it is a two-dimensional spatial detector, instead of a one-dimensional temporal detector. Ions produced through ionization and dissociation expand outward with a distribution of velocities creating a spherical shell in three dimensions. This shell is then extracted through the vacuum chamber in a similar way to the TOF configuration except now there is no pinhole to select certain energies and all spatial fragments over the solid angle reach the detector. In general, the fragments produced by the laser will have cylindrical symmetry about the ϕ-coordinate (Fig. 1.5.4). By placing the detector parallel to this plane of symmetry, only

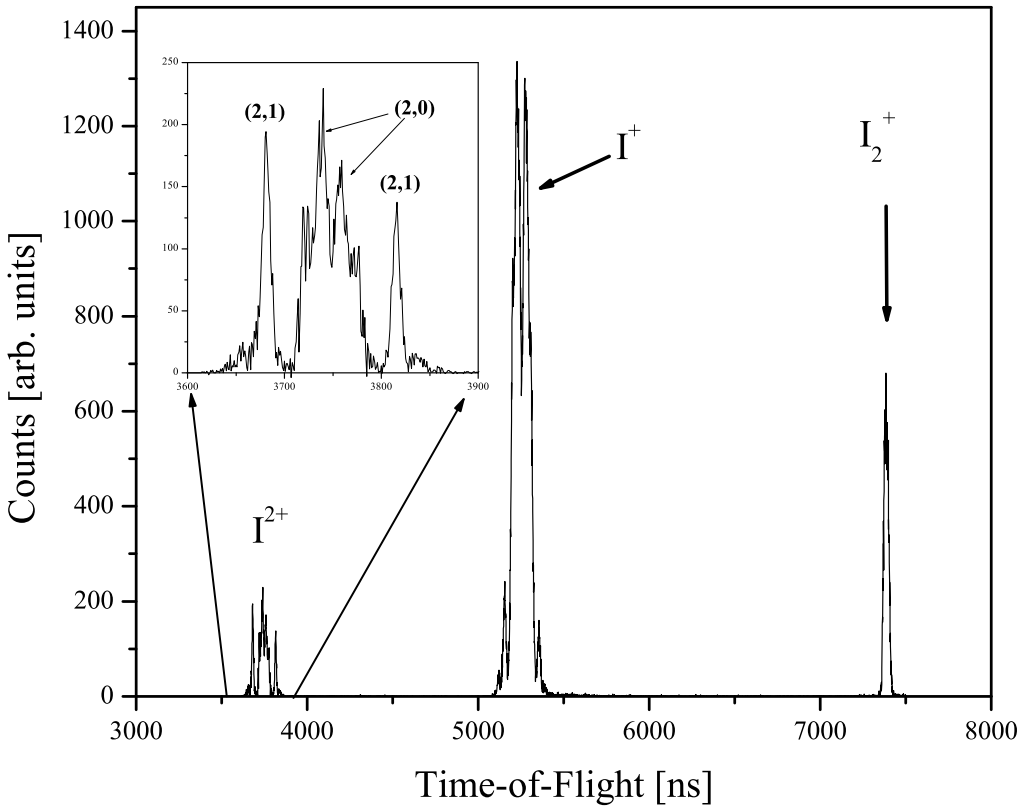

Figure 1.5.3: Example of an ion TOF spectrum showing several different ionic fragments as a function of flight time.

this coordinate is ”lost” in the subsequent projection of three to two dimensions. All velocity components are then focused in the plane of the detector using an electrostatic lensing in the form of steel plates with applied high voltages as in Fig. 1.5.5. For proper plate voltages, the velocity components of the fragments will be focused onto the same point on the detector, regardless of the position where they were created in the laser focus. This method allows for the determination of the velocity vector and angular distribution of the ion fragments, but may also be used for neutrals or electrons, and is a powerful tool in ionization and dissociation experiments. Since the three-dimensional shell is projected onto two dimensions with cylindrical symmetry, one could attempt, for example, to reconstruct a three-dimensional structure from the two-dimensional data numerically by means of an inverse Abel transformation (see for example [87]).

The three dimensional spherical shell is projected onto a two-dimensional position sensitive detector, in this case, a pair of microchannel plates (MCP). The MCP provides the spatial information of where an ion hits as it is composed of many micrometer-sized open channels. A high voltage is put across the MCP and when an ion reaches the surface it produces secondary electrons in the associated channels. The electrons are accelerated into the walls of the MCP channels, ejecting multiple electrons with each collision in the microchannel. This results in a gain of about $10^6 - 10^7$ for each ion that reaches the detector. The secondary electrons exit the MCP directly behind where the ion arrives at the detector. The electrons are then accelerated to a phosphor grid which fluoresces and can be imaged directly with a CCD camera resulting in a velocity image. A schematic of the VMI detector is shown in Fig. 1.5.5.

Each ionic fragment will reach the detector at a different time, again depending on its mass-to-charge ratio, and will spread out according to the initial momentum. Fragments or ions with a low initial momentum will hit the MCP near the center and will produce

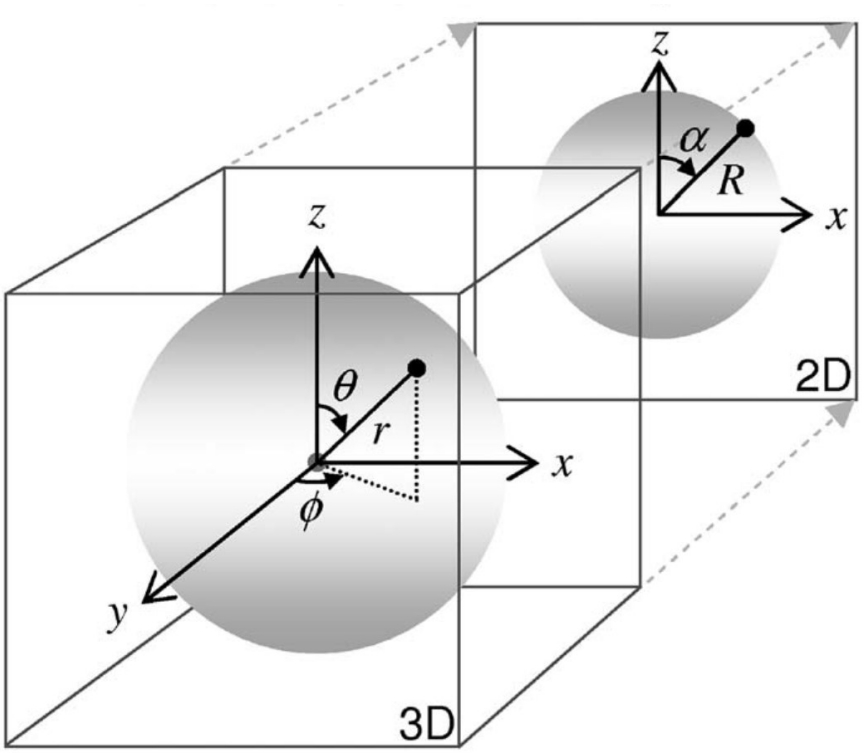

Figure 1.5.4: Schematic of the principle of velocity map imaging [86]. Laser ionization creates fragments with a distribution of velocities in three dimensions. There is cylindrical symmetry in the ϕ-coordinate about z. The detection of the fragments is a two-dimensional projection of the three-dimensional distribution.

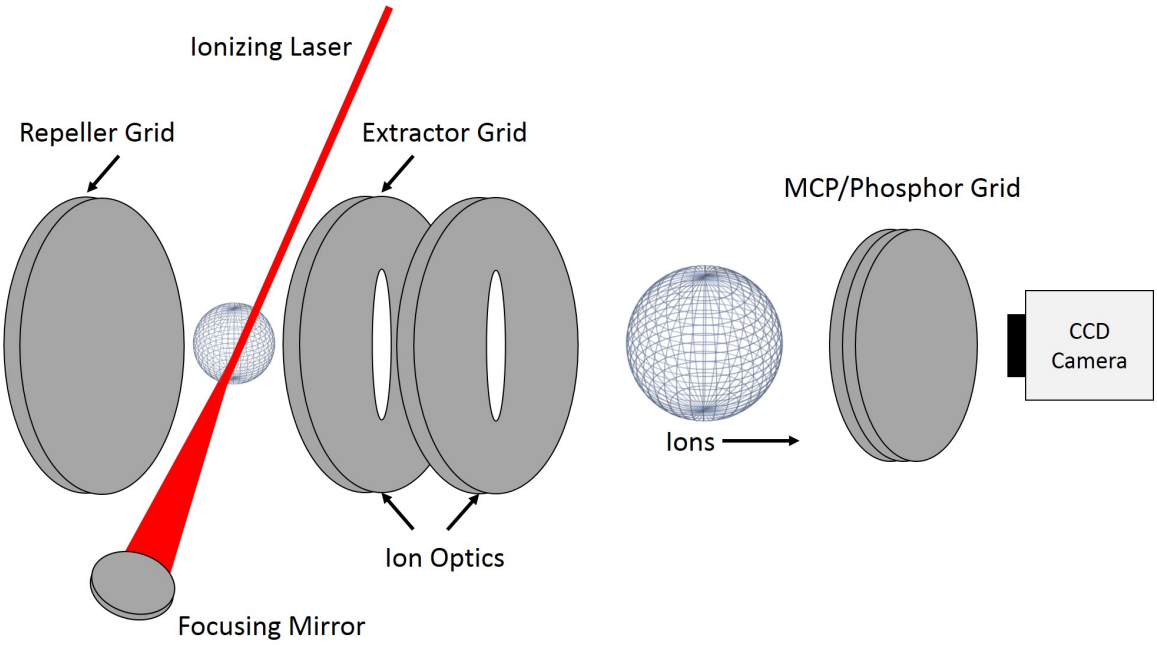

Figure 1.5.5: Schematic of the VMI setup and detection method (not to scale).

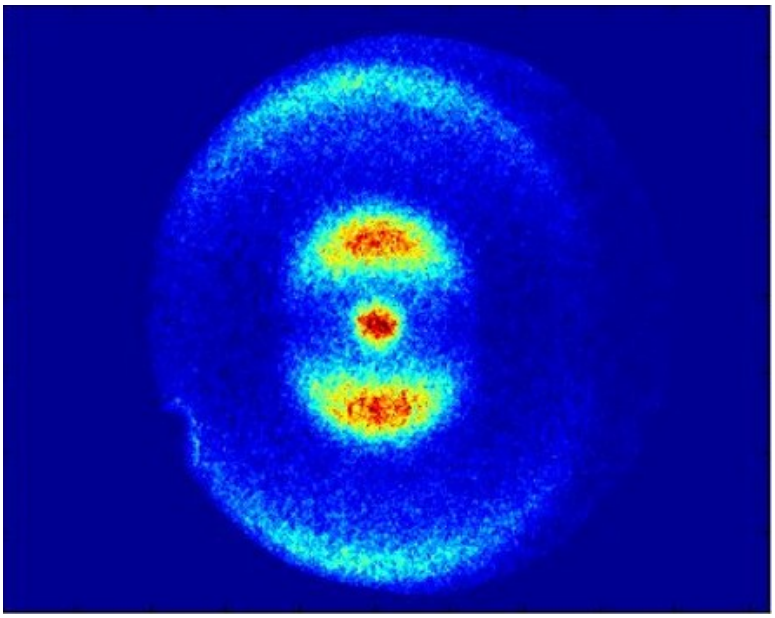

Figure 1.5.6: Example of a VMI image produced by I^{2+} ions selected by gating the MCP.

an image of a circle with a small spread. Higher energy (momentum) fragments will be further away from the center of the detector and may exhibit structure which has an angular dependence. Several images are shown in Fig. 1.5.6 for the ionization of iodine. The MCP must be gated with a high voltage pulse in order to collect data at different ion flight times in order to observe specific ions (Fig. 1.5.6).

Chapter 4 will discuss the angular distributions of ionic fragments associated with different electronic configurations of ionic states of I_2. By using a pump-probe measurement as described above, a VMI image can be collected at each probe delay and information about ionization can be recorded as a function of internuclear separation. These angular distribution measurements will provide insight as to which electrons in the molecule are involved in ionization and could lead to further understanding of our current framework for describing the evolution of molecular orbitals during ionization.

1.5.3 Measurement of Ultrafast Laser Pulses

Ultrafast pulses can be measured with a second order autocorrelation method. By mixing two laser pulses in a nonlinear crystal such as KDP (potassium dihydrogen phosphate) or BBO, a nonlinear, second harmonic signal is created which can be related to the beam overlap in the crystal. The second harmonic signal will have an intensity which is proportional to the overlap of the two beams in the nonlinear medium:

$$I(t) \propto \int_{-\infty}^{+\infty} |[E(t) + E(t-\tau)]^2|^2 dt \tag{1.5.4}$$

where $E(t)$ is the stationary beam and $E(t-\tau)$ is the second beam delayed by τ. The overlap of the two beams depends on the delay τ and the intensity will be strongest where

the beams overlap. The signal produced by the overlapping beams will have a certain width as measured by the camera which is related to the pulse duration. The delay between the two pulses can be controlled by a translation stage, for example. As the time delay between the pulses decreases, there is more overlap of the pulses in the crystal and the second harmonic signal becomes larger. The intensity as a function of time delay between the pulses may then be recorded at many time delays to produce an intensity profile of the nonlinear signal. The full width at half maximum (FWHM) of the auotocorrelation signal, $\tau_{autocorrelation}$, is related to the pulse duration of the input pulse, τ_{pulse}, as $\tau_{pulse} = \tau_{autocorrelation}/1.414$ for Gaussian pulse profiles. A calibration for the camera can be performed to find the number of pixels/fs by recording several images at different time delays. This can be done with a translation stage to change the delay between the pulses by a known amount and recording how far the image moves (in pixels) when measured by the camera.

Another method for measuring the pulse duration is to use a real time autocorrelator such that a single image can be recorded by a camera. By removing the translation stage controlling the delay between the two pulses and using a split mirror, the input beam can be split into two as in Fig. 1.5.7. Once the beams are split, both beams are sent into a nonlinear crystal and they interact to create a new pulse which is sensitive to the overlap of the beams. The region where the beams overlap in the crystal produces a much higher intensity than either beam on its own and the second harmonic produced can be observed with a camera. A schematic of the real time autocorrelator is given in Fig. 1.5.7 and an autocorrelation measurement is shown in Fig. 1.5.8.

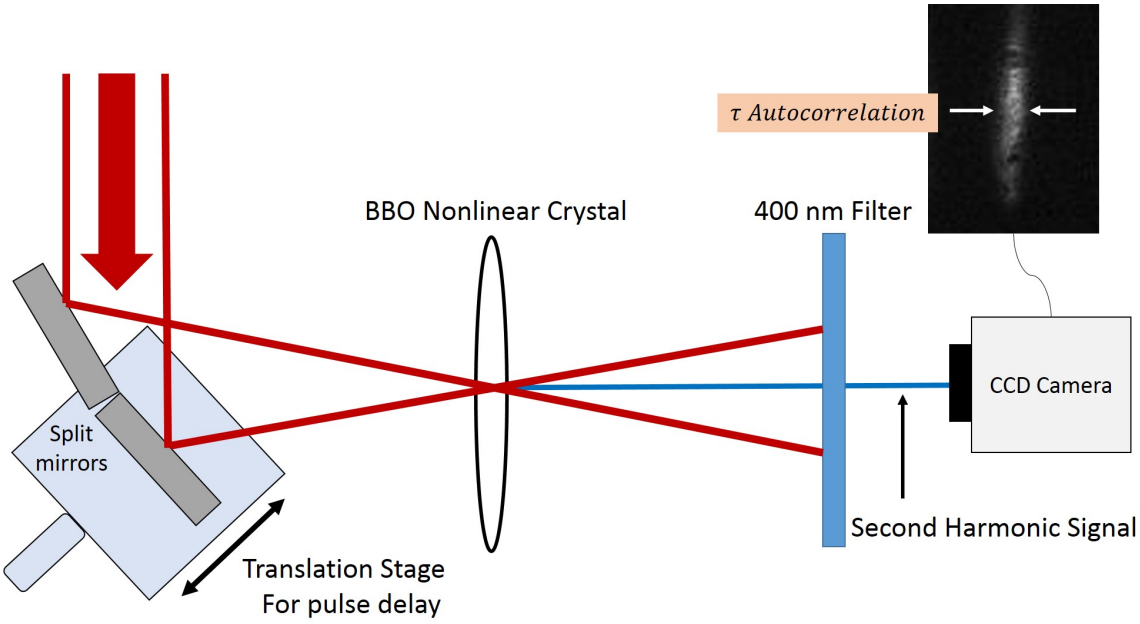

Figure 1.5.7: Schematic of second order autocorrelator. The overlap of the beams in the nonlinear crystal produces a second harmonic signal and the intensity is recorded with a camera. The width of the signal is related to the pulse duration.

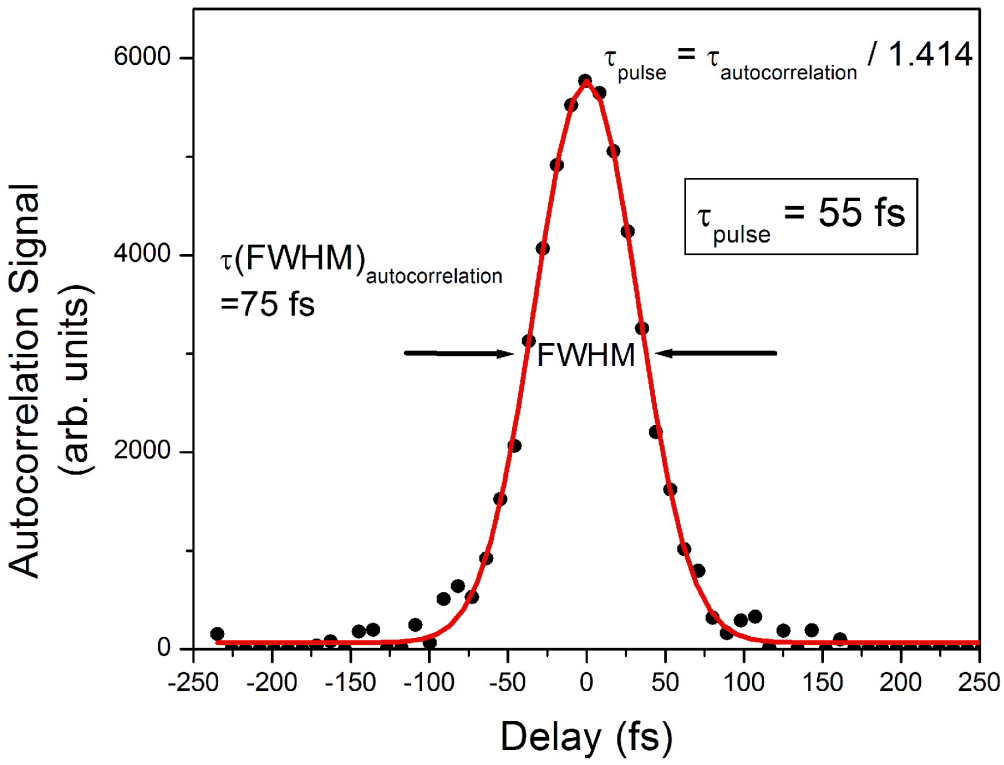

Figure 1.5.8: Example of a second order autocorrelation measurement to determine the pulse duration. The full width at half maximum (FWHM) is corrected for Gaussian pulses by dividing by the $\sqrt{2} = 1.414$ to give the pulse duration.

Chapter 2

Internuclear Separation Resolved Asymmetric Dissociation of I_2 in a Two-Color Laser Field

2.1 Introduction

Atoms and molecules have been studied in strong laser fields for decades with many kinds of experiments including above threshold dissociation [6], symmetric and asymmetric dissociation [7–12], electronically excited fragments [13–16], and the dependence of ionization on internuclear separation [17–22]. Molecules also possess an extra degree of freedom in the form of nuclear motion which gives rise to avoided potential energy crossings when a laser field is applied [23–25]. Furthermore, many of the dynamics observed in molecules have a strong dependence on the internuclear separation, perhaps most notably in the phenomena of enhanced ionization at a critical internuclear distance, R_c [20]. Homonuclear diatomics are particularly interesting as they exhibit charge-resonance (CR) states which

couple strongly to electromagnetic fields and have no analogue in atoms [26]. Understanding of these phenomena is critical to providing a description of the complex dynamics of molecules in strong laser fields.

The CR states of a diatomic molecule play an important role in the ionization of the molecule by a strong laser field and have been extensively studied theoretically [17, 30]. In a 1-electron system, the CR states are the lowest lying states and along with electron localization produce a large increase in the ionization rate at a critical internuclear separation R_c. This phenomenon of charge-resonance enhanced ionization (CREI) [17] appears to be universal in diatomic molecules and R_c is consistently found to be 2-3 times the equilibrium distance of the neutral molecule [20]. The CR states of an even-charged molecule are the excited ionic states which correlate to a dissociation limit with a charge difference of 2 between the fragments (e.g. $I_2^{2+} \rightarrow I^{2+} + I$). In this example, the ionic states are roughly 8 eV above the covalent ground state, although the $N_2^{6+} \rightarrow N^{4+} + N^{2+}$ dissociation channel has been observed [27] which lies 30 eV above the ground state. On the one hand, these ionic states have been identified as doorway states to ionization of even-charged molecules and produce a similar effect of R_c in odd-charged molecules. On the other hand, the charge asymmetric dissociation channels which correlate with the ionic states are observed in all strong field ionization experiments, so the ionic states are not simply doorway states but are themselves populated by the laser field. Given the high degree of excitation possible with near-IR laser fields, it is natural to ask how exactly are they populated. Unfortunately, typical time-of-flight (TOF) experiments studying the ionization and dissociation of molecules in strong laser fields simply do not have the energy resolution to separate the gerade and ungerade states that make up the CR pair, although it is the dynamics of these states that determines the response to the laser field. However, information about these states can be obtained by using $1\omega 2\omega$ fields which are created by coherently adding the fundamental

and second harmonic of a laser field:

$$E(t) = E_\omega(t)cos(\omega t) + E_{2\omega}(t)cos(2\omega t + \phi), \tag{2.1.1}$$

where ϕ is the relative phase between the pulses and E_ω and $E_{2\omega}$ are the envelopes of the fundamental and second harmonic, respectively (Fig. 2.2.1). This combined field can break the spatial symmetry of the interaction, which, in turn, can lead to a spatial asymmetry in the dissociation of the ionic states. From this, the amplitude and phase of the populations in the CR states can be determined.

The spatial asymmetry of the ion yield, $\beta(\phi)$, is found by calculating the ion yield for the forward (Y_F) and backward peaks (Y_B) and is conventionally defined as:

$$\beta(\phi) = \frac{Y_F(\phi) - Y_B(\phi)}{Y_F(\phi) + Y_B(\phi)}. \tag{2.1.2}$$

The asymmetric electric field will preferentially ionize more strongly in one spatial direction over the other resulting in a measurable difference in the ion yields between the ions with initial velocities toward or away from the detector. The asymmetry depends on ϕ and the dissociation channel. However, the difference in detection efficiency of the forward and backward ions affects $\beta(\phi)$: the backward-going ions have a larger transverse spread when they reach the extraction pinhole than the forward-going ions. As a result, the backward peaks have a smaller chance of passing through the extraction pinhole and being detected. This angular acceptance results in larger forward peaks than backward peaks since the molecules in these experiments are not perfectly aligned. However, this difference in angular acceptance was measured and accounted for.

Asymmetries produced by two-color fields have been studied theoretically [32] and ex-

perimentally [33–36] in primarily light molecules. The asymmetric dissociation of D_2 in a two-color field has been observed at ion energies identified with bond softening, rescattering and above threshold dissociation [36]. Similar ion yield asymmetries have been seen in H_2, N_2, HD, O_2, and CO_2 [33, 34]. In these light molecules, the dynamical processes of interest occur on time scales which are on the order of the pulse duration (around 30-50 fs). One immediate consequence is that ionization and dissociation are happening in parallel. It is therefore difficult to resolve the dynamics and important information may be obscured.

This chapter presents internuclear separation resolved measurements of the ionization of I_2 in a two-color laser field with 35 fs laser pulses, allowing us to decouple ionization and dissociation. We do this by creating a vibrational wavepacket (VWP) with a pump pulse in the B state of I_2, which evolves in time. The two-color probe pulse then ionizes the molecule at later times corresponding to different values of R. In this way, we can measure field-induced spatial asymmetries in the subsequent dissociation as a function of R. We find that the spatial asymmetry of a particular ion has a strong dependence on R, increasing from close to zero to almost 0.5. Moreover, the $1\omega 2\omega$ phase which produces the maximum asymmetry is independent of R. We compare these results to two models: a simple two-level model of the ionic states of a doubly charged molecule and a more complete three-level model which also includes the ground state and multiphoton excitation. We find good qualitative agreement with the two-level model, which implies direct ionization from the previous charge state to the field-dressed ionic states. However, we do find evidence of a breakdown in our quasistatic model which may be due to mechanisms such as non-adiabatic effects, electron localization, or dephasing.

Contrary to other experiments [34], we do not see any spatial asymmetry in dissociation channels where the charge difference, Δq, is one, such as the (1,0), (2,1), and (3,2) channels. In addition, we observe new features in the TOF spectrum, namely that the well-known

(2,0) dissociation channel appears to consist of two distinct channels with different kinetic energy releases and different dependences of the ionization rate into the channels as a function of R.

2.2 Experiment

2.2.1 R-resolved measurements

The B state ($B^3\Pi_u^+$) of the iodine molecule is well known and is used as an intermediate state to control the internuclear separation of the molecule. The method described here and schematically represented in Fig. 2.2.2 has been studied and verified in Ref. [37]. Since the inner turning point of the B state is dependent upon the wavelength, we also have some additional control over the VWP. The wavelength of the pump pulse couples the neutral X and B states and determines the initial R position in the B state at which the vibrations begin. The vibrational period of the B state at 513 nm is around 700 fs. The pump beam resonantly excites the neutral I_2 to the B state and the $1\omega 2\omega$ probe pulse ionizes the B state at a variable time delay with a resolution of 10 fs.

The probe pulse ionizes the molecule and, depending on the intensity, can create molecular ions including I_2^+, I_2^{2+} and I_2^{3+} [40]. Generally, the ionized molecules dissociate and the kinetic energy release of the ion fragments is measured through TOF. Identification of all measured dissociation channels of I_2 and its ions have been previously determined through correlation measurements [11]. Finally, knowing the potential curve of the B state allows us to convert from time delay to internuclear separation.

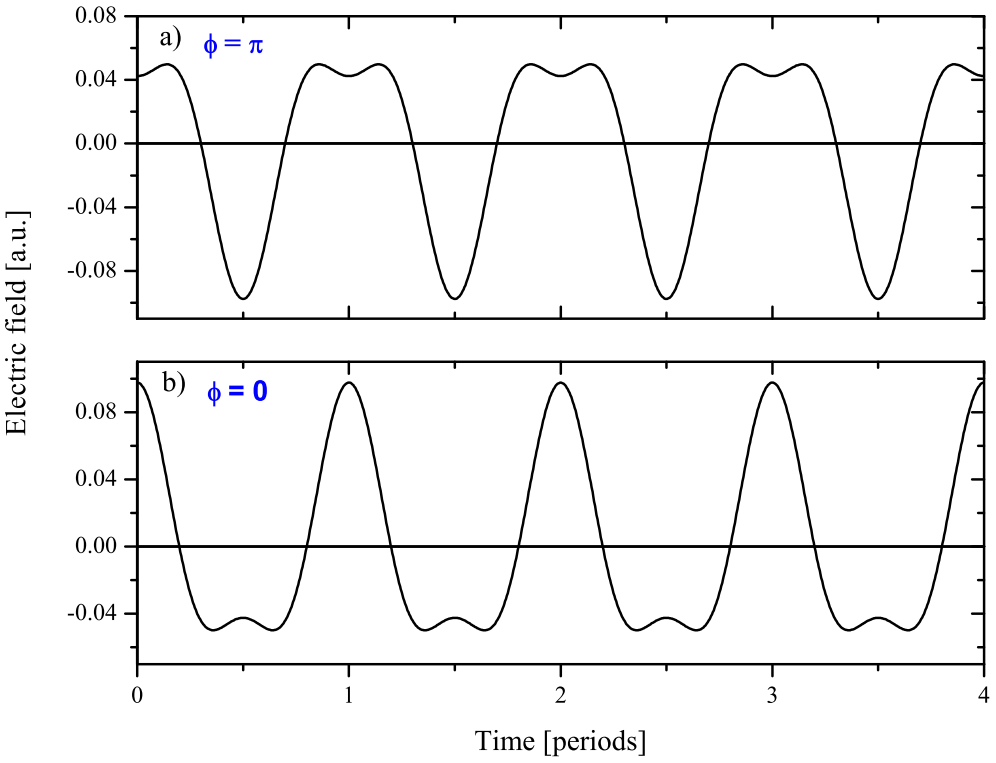

Figure 2.2.1: Two-color electric field $E(t) = E_\omega cos(\omega t) + E_{2\omega} cos(2\omega t + \phi)$ for a) $\phi = \pi$ and b) $\phi = 0$. The amplitudes are $E_\omega = 2E_{2\omega}$, which produces the maximum field asymmetry.

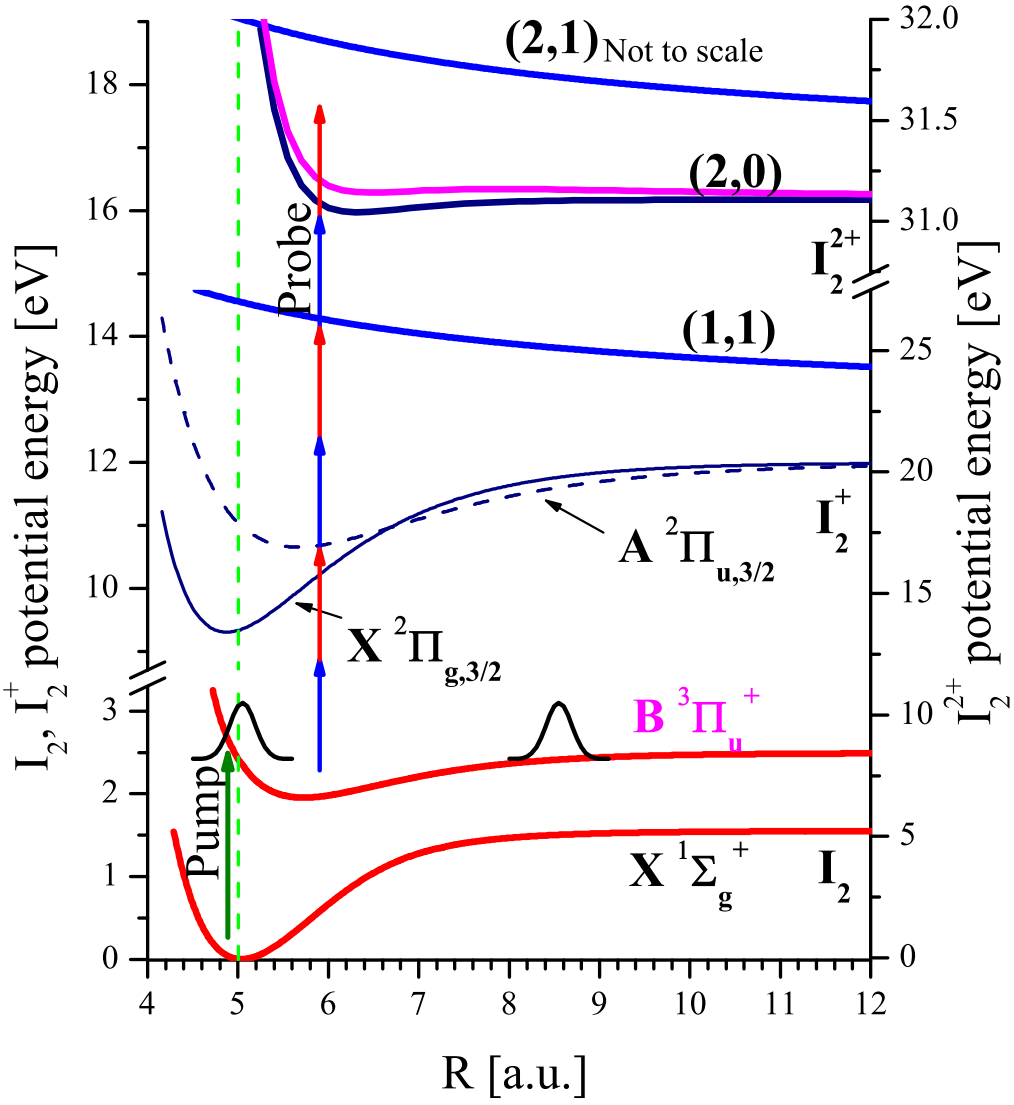

Figure 2.2.2: Schematic potential curves and pulse sequence. Note the two curves of the (2,0) channel corresponding to the gerade (upper) and ungerade (lower) states.

2.2.2 Experimental setup

The data collected for I_2 were obtained using a Ti:Sapphire laser system. The system produces 800 μJ in 35 fs at a wavelength of 800 nm and a 1 kHz repetition rate. The beam is split by an 90/10 beam splitter to send 10% of the beam through a two-color ($1\omega 2\omega$) arm and 90% through a TOPAS (traveling-wave optical parametric amplifier of superfluorescence) system. The TOPAS is tuned to a wavelength of 513 nm and produces about 2 μJ in 50 fs. The pump and probe pulses are parallel to the TOF axis but offset in space and focused by a silver spherical mirror inside the TOF chamber to obtain spatial overlap. The pump pulse is about 1 μJ and the probe pulse has energies of 2.6 μJ and 0.4 μJ for the 800 and 400 nm light, respectively. The intensities used are 4.3x10^{13} W/cm^2 for the 800 nm beam, 5.2x10^{13} W/cm^2 for the 400 nm beam, and 1.6x10^{13} W/cm^2 for the 513 nm beam. The 800 nm and 513 nm beams are both dispersion compensated with prism pairs. A computer controlled motorized stage is used to change the time delay between the pump and probe pulses.

The iodine is introduced into the vacuum chamber effusively from a stainless steel bulb. Experiments are done using a typical Wiley-McLaren TOF spectrometer [43]. Once the ions are produced they are extracted by a dc electric field of 223 V/cm through a 1 mm pinhole and accelerated by an additional 800 eV. They are then sent through a 10 cm field-free drift tube giving both symmetric velocity dispersion and high resolution. A microchannel plate is used to detect the ions and the signal is amplified, discriminated, sent to a time-to-digital converter and then readout to a computer. The molecules in the TOF chamber are at room temperature with a pressure of around 1x10^{-6} torr and a base pressure better than 10^{-9} torr.

The resulting TOF spectra for a particular dissociation channel consist of two peaks

which are symmetric about the arrival time of the zero-kinetic-energy ion. The "forward" ("backward") peak represents ions with initial velocities toward (away from) the detector. An example of the TOF spectrum is shown in Fig. 2.2.3. The separation of the peaks is proportional to the initial momentum of the dissociating fragments.

2.2.3 Mach-Zehnder interferometer and phase measurement

The $1\omega 2\omega$ beam is produced by frequency doubling the 800 nm light with a 250 μm thick BBO crystal to generate 400 nm light. Immediately after the crystal, the 800 and 400 nm beams are separated spatially and recombined with a Mach-Zehnder interferometer designed for maximum stability (Fig. 2.2.4). Once recombined, the spatial overlap is optimized by focusing the beams and imaging them with a camera. The arm of the interferometer containing the 800 nm beam contains a $\lambda/2$ waveplate to rotate the polarization so that it is parallel with the TOF axis and the 400 nm beam. A variable attenuator in the 800 nm arm allows intensity ratios of $1\omega/2\omega$ from 1:1 up to 10:1 and controls the path difference of the two beams. Spectral interference is used to determine the relative phase of the two colors. As shown in Fig. 2.2.4, a surface reflection from the TOF vacuum chamber window is used to send the primary 800 and 400 nm beams into a spectrometer. In order to measure the spectral interference between the two beams, the polarizations and wavelengths must be the same. To achieve this, a second BBO crystal is utilized to produce a secondary vertically polarized 400 nm beam. A polarizer projects the polarizations of the primary and secondary 400 nm beams onto the same axis and the beams can then interfere. This surface reflection allows real time measurements of the relative phase.

When the beams are properly overlapped, the interference spectrum at zero time delay shows no fringes - the overall amplitude simply goes up and down with the phase of

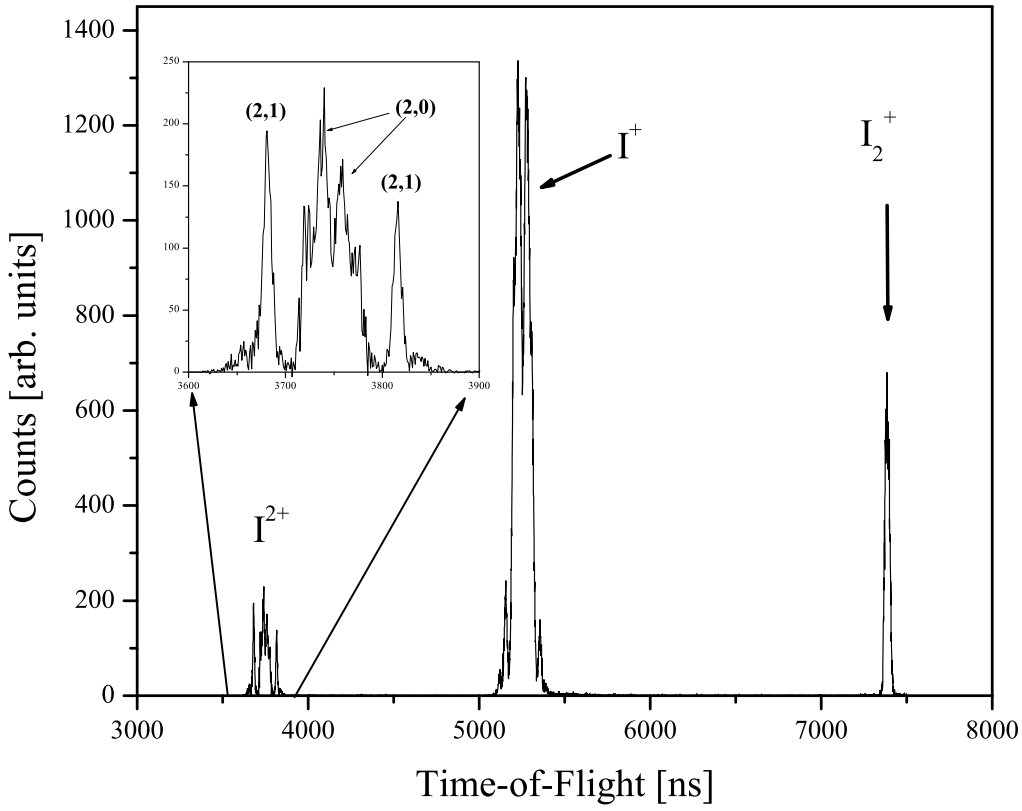

Figure 2.2.3: TOF spectrum for a given time delay and phase showing all channels produced for the intensities used.

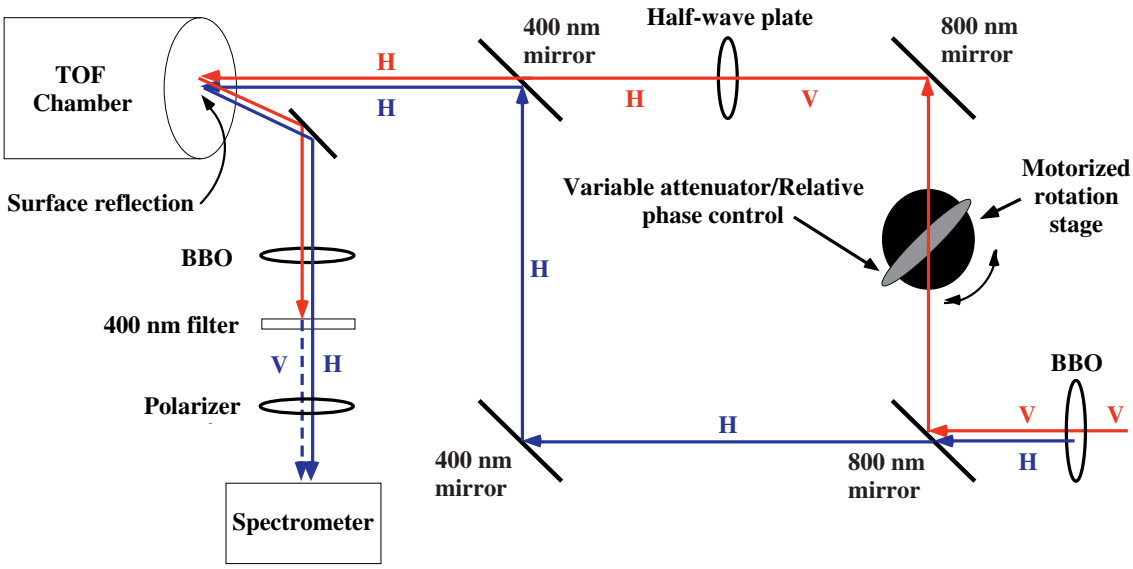

Figure 2.2.4: The Mach-Zehnder interferometer designed to control the relative phase of the 800 and 400 nm pulses. The polarizations of the beams are labeled as ”H” and ”V” for horizontal and vertical, respectively. The motorized rotation stage can change the relative phase by a minimum of 0.5 rads (about 30 degrees).

the pulses. Thus, in order to more accurately measure the phase, fringes are produced in the spectrum by temporally offsetting the two beams with a thin piece of glass before the secondary doubling crystal. An example interference spectrum is shown in Fig. 2.3.1. The resulting spectrum is then fit with a sinusoidally modulated Gaussian and the parameter describing the relative phase is recorded for each TOF measurement. The control of the relative phase of the beams is obtained by mounting a glass variable attenuator on a motorized rotation stage which can change the phase by about 0.5 rads with each step. The interferometer has proven to be phase stable over periods of hours to better than $\pm$ 5 degrees.

2.3 Experimental Results and Models

2.3.1 Asymmetric Ion Yields in I^{2+}

Generally, the phase of the $1\omega 2\omega$ pulse is set and the TOF spectra are recorded for time delays of 0 to 200 fs in 10 fs steps. This is repeated for up to 18 different phase values. With this, the spatial asymmetry of any dissociation channel can be determined as a function of delay or R.

The resonant excitation to the B state is about 20% efficient, leaving roughly 80% of the population in the ground X state. Thus, the $1\omega 2\omega$ pulse can continue to ionize the X state and there are (2,0) peaks present in the TOF which are from the X state. This background is measured by blocking the 513 nm beam and subtracted from the pump-probe data, taking into account the depletion of the X state.

A typical TOF delay scan for a particular phase is presented in Fig. 2.3.3. Several features are immediately apparent. First, the image is fairly symmetric about a horizontal

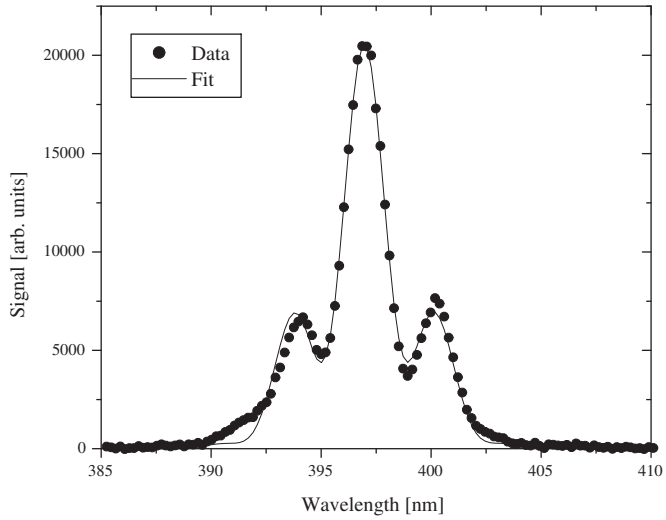

Figure 2.3.1: Example interference spectrum used to calculate the relative phase ϕ of the $1\omega 2\omega$ field. The solid line is a sinusoidally modulated Gaussian fit.

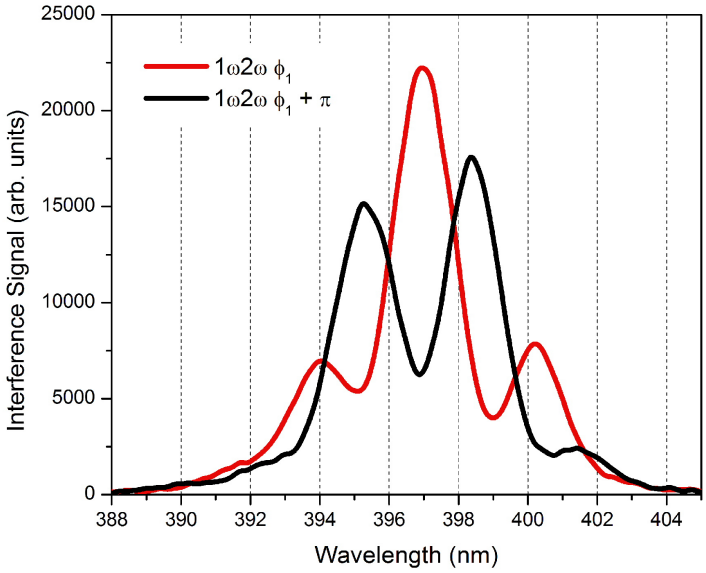

Figure 2.3.2: Examples of the interference spectrum produced by the $1\omega 2\omega$ field at two different relative phases, ϕ.

line at a TOF of 3748 ns corresponding to an I^{2+} ion with zero kinetic energy. The data above this line are the late (backward) ions, and below are the early (forward) ions. Second, the data form "tracks": the TOF or kinetic energy release (KER) smoothly changes with time delay as can be seen for both the (2,0) and (2,1) states. From Fig. 2.2.2 we see that the molecule expands in time on the *B* state and *R* increases generally leading to lower KER's. We identify the higher KER track as the (2,1) channel, and the lower as the (2,0) channel. In fact, we verify the motion on the *B* state with the KER of the (2,1) channel [37]. Finally, the (2,0) channel has substructure which appears to result from two separate states. The tracks in the TOF produced from these states are shown Fig. 2.3.5. The clear difference in the kinetic energy release observed in the TOF shows that two different (2,0) channels are being populated.

The disappearance of the (2,0) signal around 200 fs has been attributed to population trapping in the slightly bound region of the (2,0) potential curve [37]. The pump wavelength sets the inner turning point of the VWP and allows access to a large range of *R* values where trapping becomes possible. In order to discuss the experimental results in terms of *R*, a simulation was conducted to find the expectation value of *R* on the *B* state as a function of pump-probe delay. The results of the simulation shown in Fig. 2.3.4 allow conversion from pump-probe time delay to *R*. We find that the outer turning point on the *B* state is at a pump-probe delay of about 400 fs or about 8.7 a.u. as seen in Fig. 2.3.4. The range over which we observe the signal from I^{2+} in this experiment is from a delay of 0 to about 200 fs (solid line in Fig. 2.3.4), or equivalently about 5 to 8 a.u..

The asymmetry of the (2,0) channel is found from Eq. (2.1.2). The measurement of the asymmetry for each of the (2,0) channels is found by fitting the pairs of peaks from the TOF with Gaussian curves and using the areas of the curves as the ion yield (Fig. 2.3.6). The peaks are labeled as "slow" and "fast" to distinguish the two channels. Typically, the

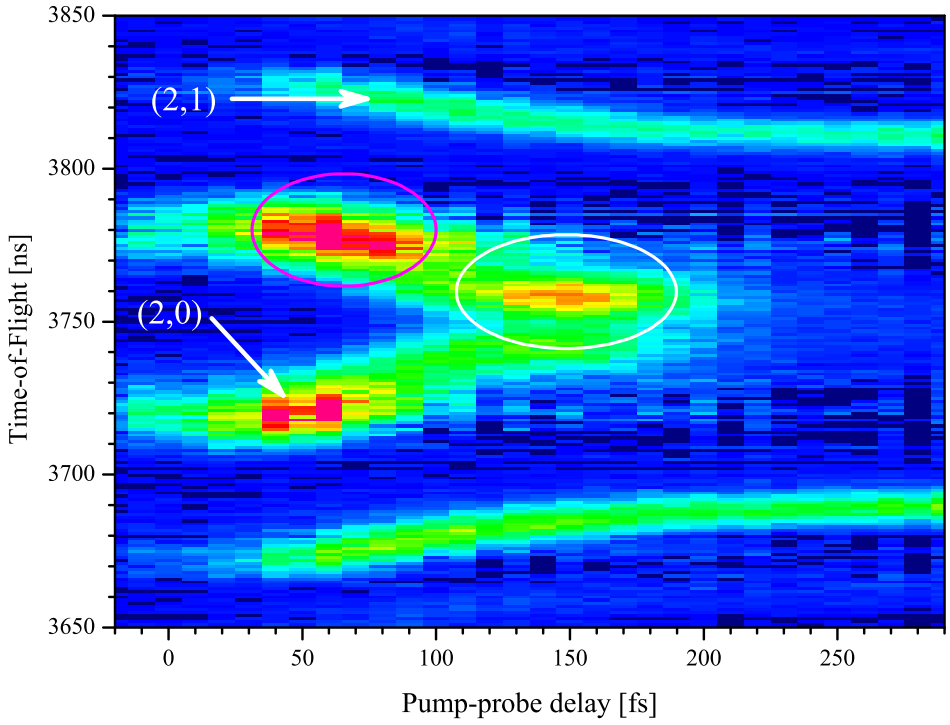

Figure 2.3.3: TOF as a function of the delay between the 513 nm and $1\omega 2\omega$ pulses at relative phase $\phi \approx 0$. The KER tracks for the (2,0) and (2,1) channels are labeled and the (2,0) substructures are circled. The color represents ion counts with red for higher count number and blue for lower count number.

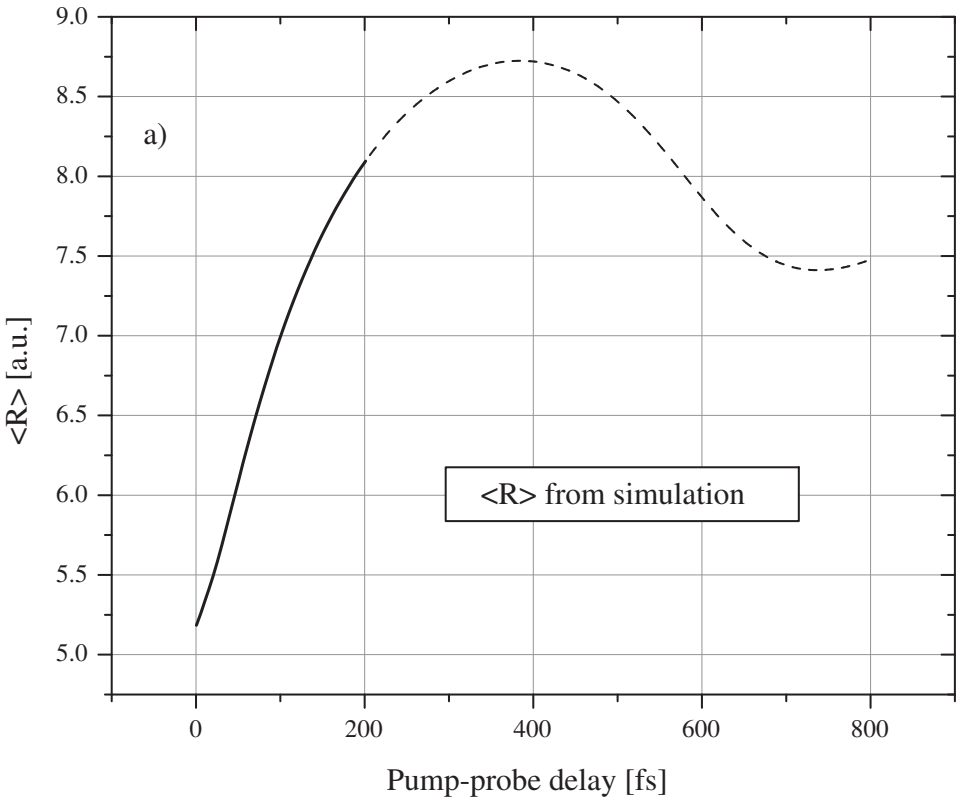

Figure 2.3.4: Simulation results for the expectation value of R vs. Pump-probe delay for a VWP on the B state used to convert from time delay to R. The solid line highlights the region over which the I^{2+} signal is observed experimentally.

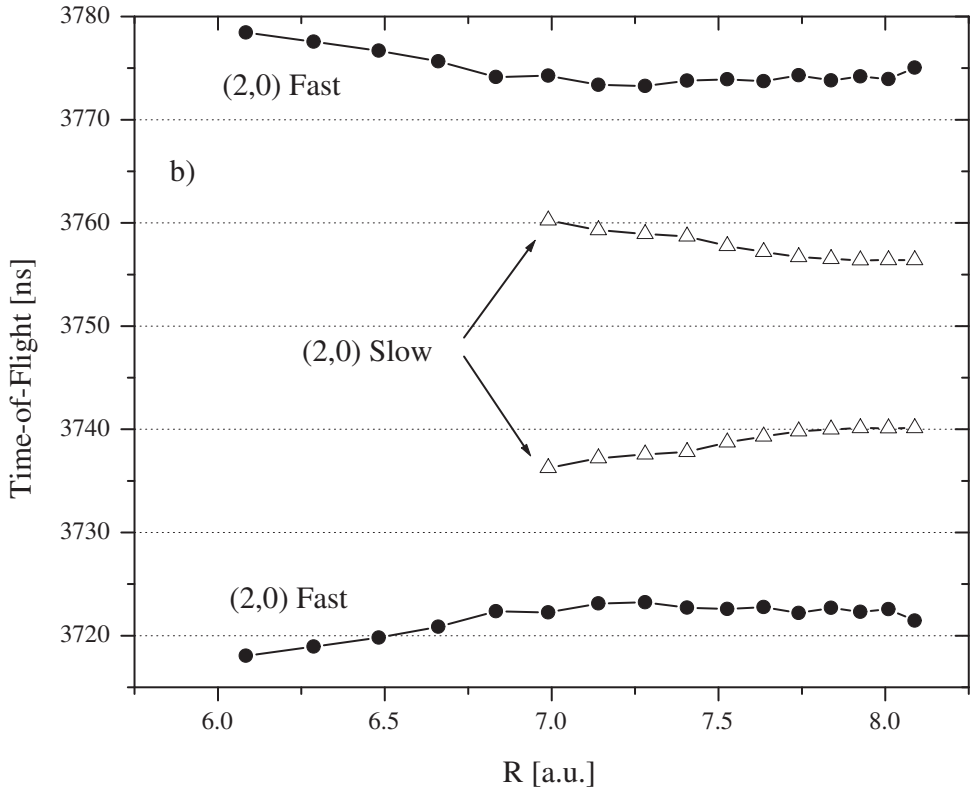

Figure 2.3.5: Centers of peaks for each of the (2,0) channels portraying the tracks seen in the TOF (Fig. 2.3.3) now as a function of R. The centers are found by fitting each of the peaks with a Gaussian.

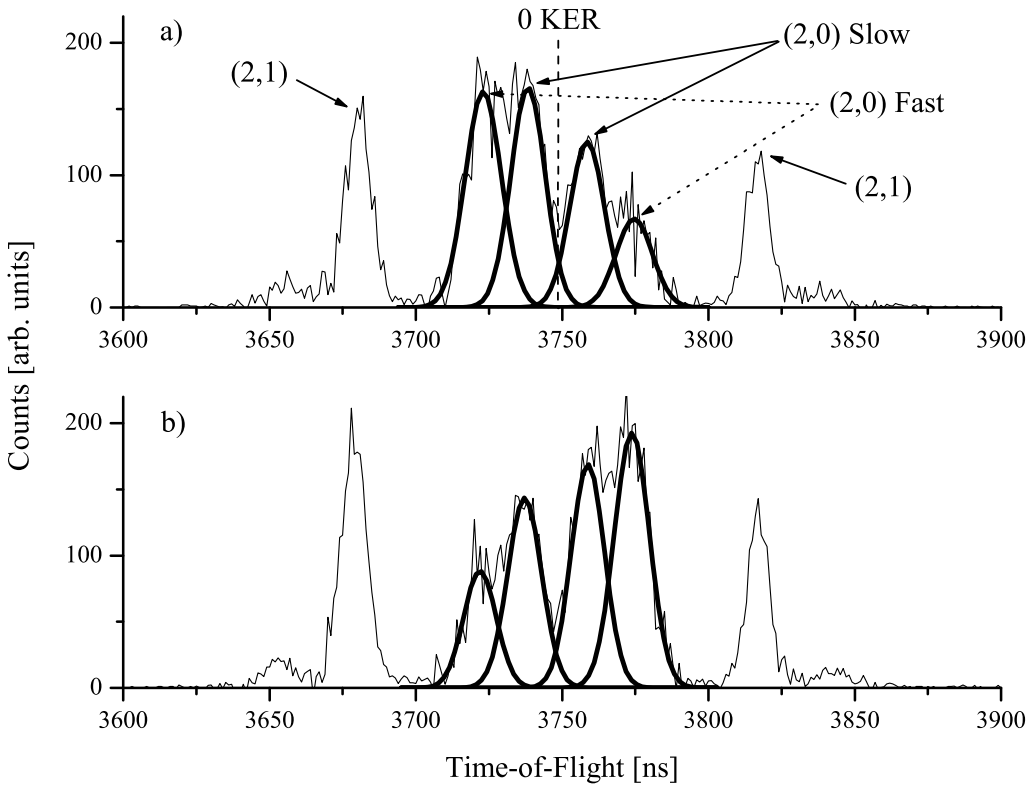

Figure 2.3.6: TOF data showing the two sets of peaks associated with the (2,0) channel at a pump-probe delay of 130 fs ($R = 7.4$ a.u.). The peaks are symmetric about the 0 kinetic energy release (KER) line. The solid lines represent Gaussian fits to each pair of peaks for a) TOF at $\phi = \pi$ and b) TOF at $\phi = 0$

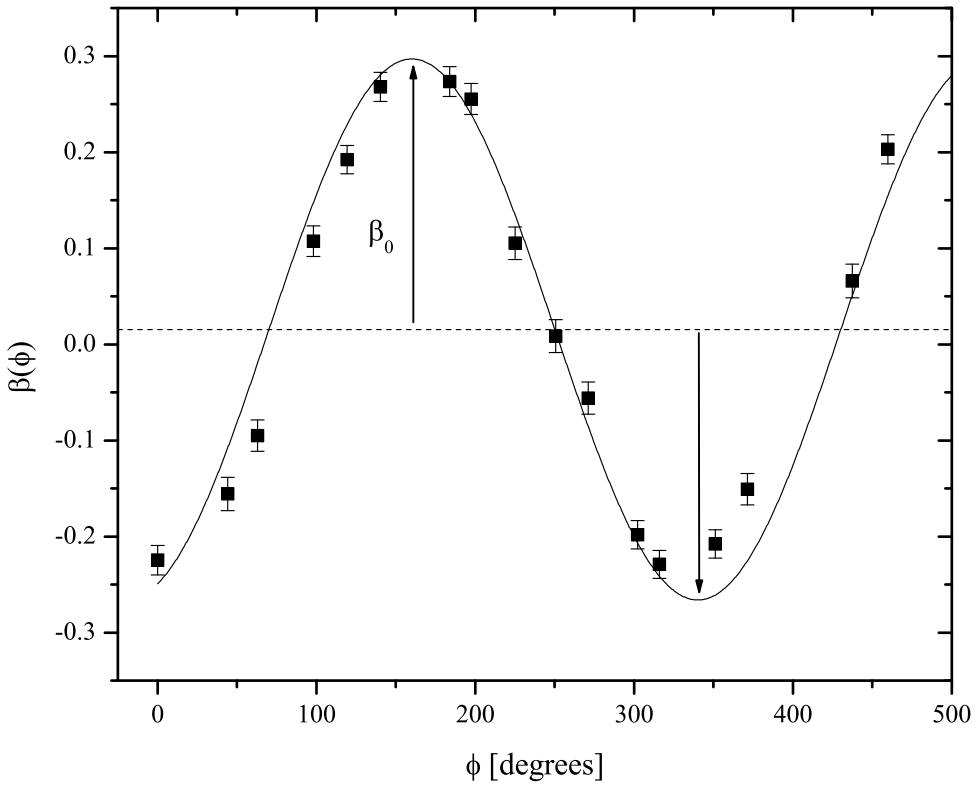

Figure 2.3.7: Example of the left/right asymmetry vs. relative phase ϕ for the (2,0) channel at 130 fs pump-probe delay. The solid line is a sinusoidal fit using Eq. (2.3.1). The arrows indicate the amplitude of the asymmetry β_0.

total "left/right" asymmetry is measured [34]. Here, the left (right) is defined as the two (2,0) peaks immediately to the left (right) of the 0 KER (3748 ns). Fig. 2.3.7 shows an example of the left/right asymmetry of the (2,0) channel as a function of relative phase. The asymmetry shows a clear dependence on the phase of the $1\omega 2\omega$ field with the maxima and minima separated by π, as expected. Interestingly, the (2,1), (1,0), and (3,2) do not show an asymmetry while the (3,1) channel does, in addition to the (2,0).

2.3.2 Amplitude of Spatial Asymmetry

To examine the asymmetry dependence on internuclear separation, data sets at each R are fit to find the maximum amplitude of the asymmetry β_0 and the relative phase of the maximum ϕ_0:

$$\beta = \beta_0 sin(\phi + \phi_0) + \beta_{off} \tag{2.3.1}$$

where β_{off} is the offset resulting from the difference in the detection efficiency between the forward and backward-going peaks. For left/right asymmetry, β_0 increases with R until about 7.5 a.u. when the amplitude reaches a maximum of about 0.3 (Fig. 2.3.8) and agrees qualitatively with the results of our two-level model (see Appendix) presented in Fig. 2.3.9 and discussed below. Although the amplitudes in the experimental results (Fig. 2.3.8) and the two-level calculations (Fig. 2.3.9) are different, clearly there is a region of R in which β_0 increases monotonically and a larger R region where β_0 approaches a constant maximum value. Further, the phase ϕ_0 of Eq. (2.3.1) shows no R dependence so the maximum asymmetry occurs at the same $1\omega 2\omega$ phase for each pump-probe delay (See inset of Fig. 2.3.8). This observation is in agreement with the experiments of Ref. [34] and the simple model of a two-level system presented here in which the maximum asymmetry will occur when the field itself has maximum asymmetry.

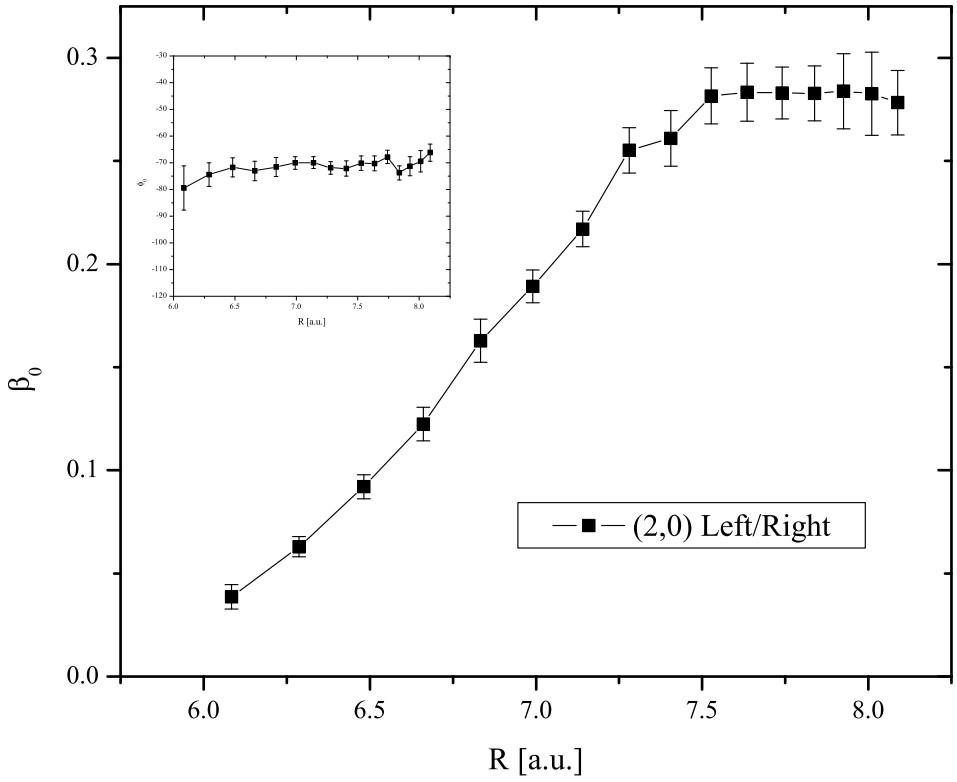

Figure 2.3.8: Measured amplitude of the asymmetry β_0 for the left/right asymmetry of the (2,0) channel. The inset shows the phase ϕ_0 vs R with a vertical scale of 90 degrees.

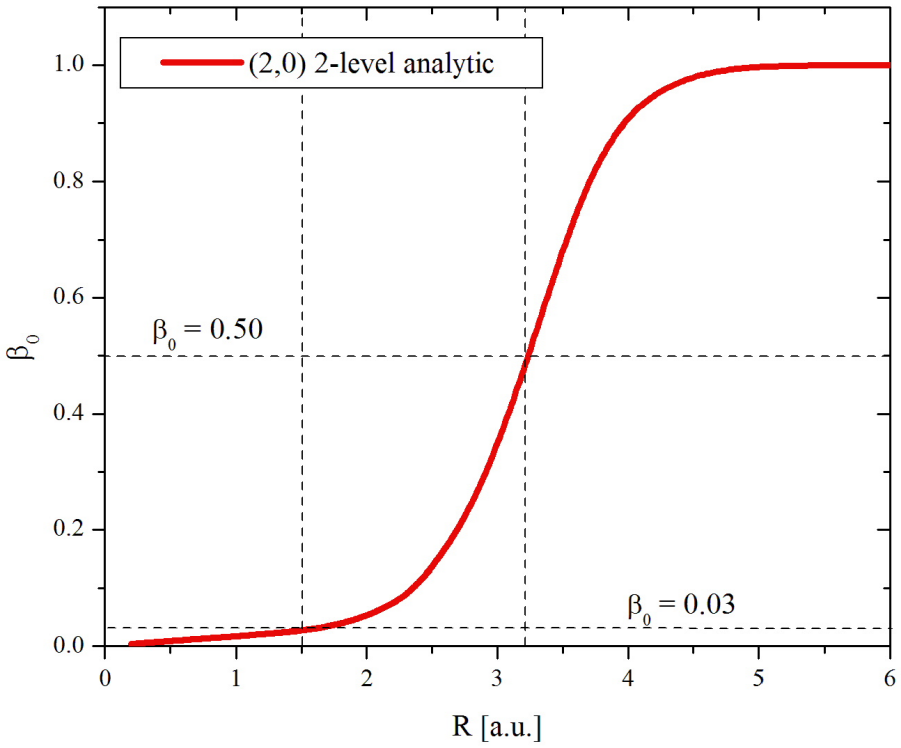

Figure 2.3.9: Analytic calculation of the amplitude of the asymmetry, β_0, for one (2,0) channel. The minimum and maximum asymmetries measured experimentally are indicated by the dashed horizontal lines.

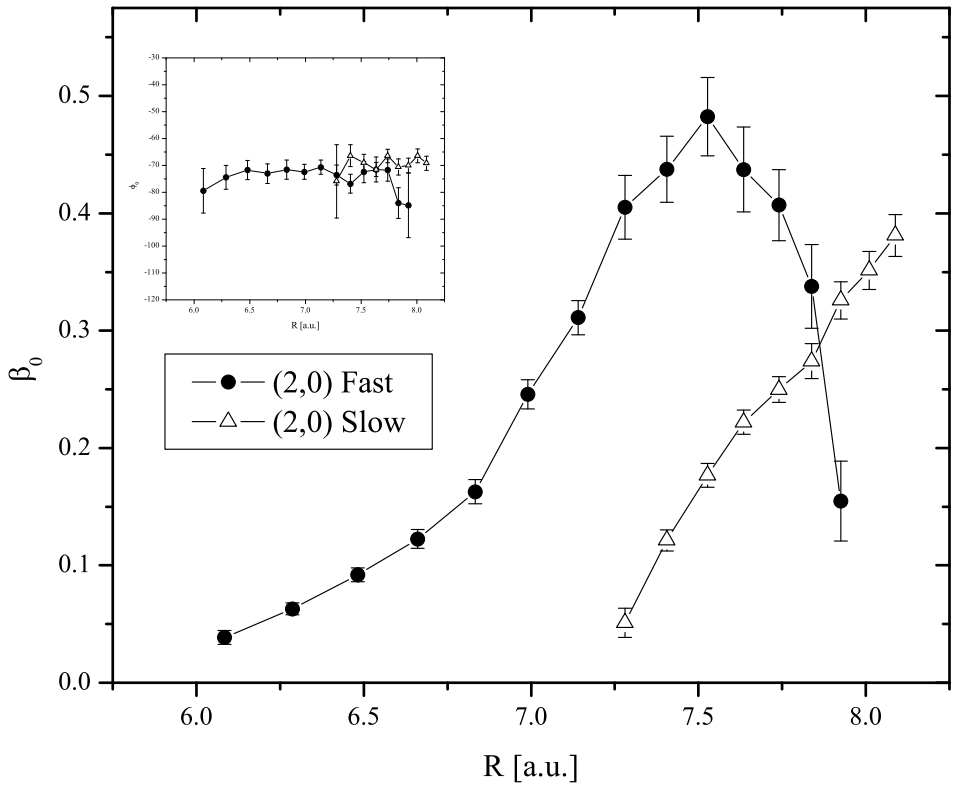

Figure 2.3.10: Measured amplitude of the asymmetry β_0 for each of the observed (2,0) channels. The inset shows the phase ϕ_0 vs R with a vertical scale of 90 degrees.

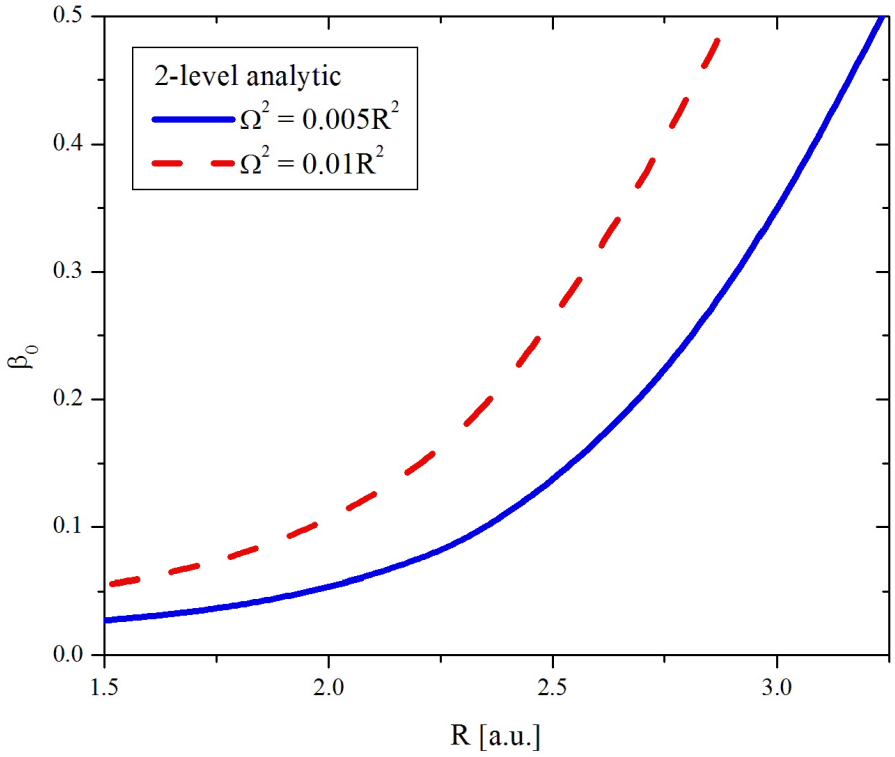

Figure 2.3.11: Analytic calculation of β_0 for two different couplings in the range of values measured experimentally. The asymmetry is monotonically increasing with R in this region. The different couplings of the CR states may be related to the results of Fig. 2.3.10.

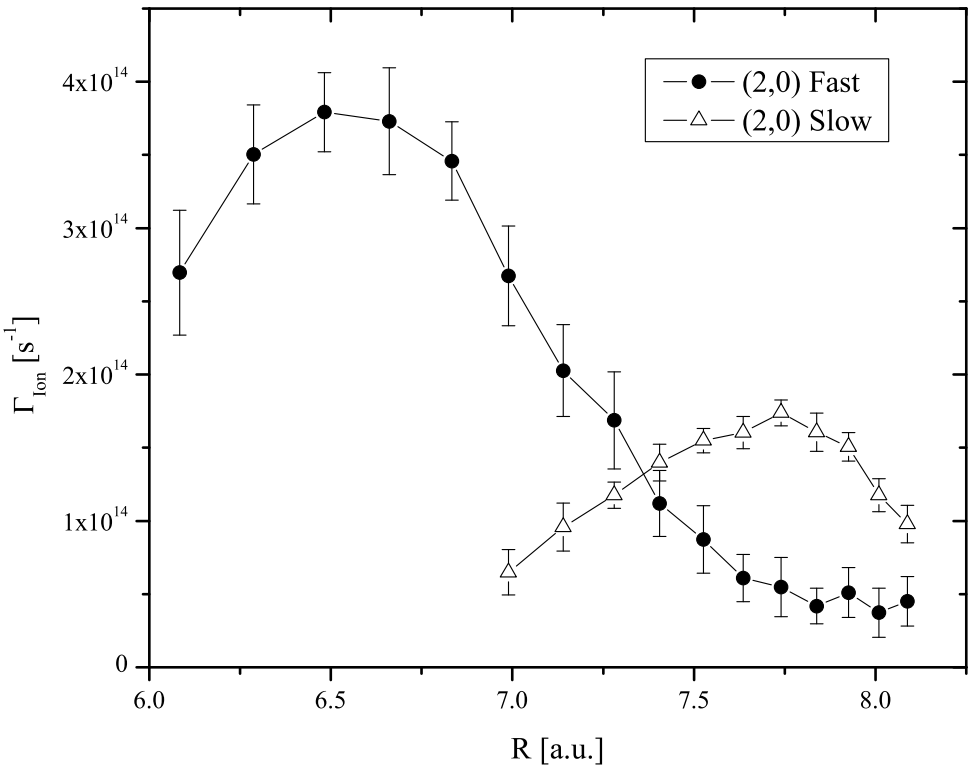

Figure 2.3.12: Ionization rates vs internuclear separation for each of the (2,0) channels. Each (2,0) state has a different critical internuclear separation.

The initial measurement of the left/right asymmetry provides evidence that β_0 increases with R and ϕ_0 is constant with R as well as qualitative agreement with our two-level model. However, the left/right asymmetry measurement does not fully take advantage of our time-of-flight resolution: it simply provides a measurement of all the detected ions within a range of KER which are initially toward or away from the detector. In fact, closer examination of the (2,0) TOF measurements reveals that multiple peaks which we attribute to two different (2,0) channels can be resolved (Fig. 2.3.6). It is therefore pertinent to examine each of the (2,0) channels and perform calculations which are analogous to those done in the left/right asymmetry scenario.

Fitting each set of (2,0) peaks with Gaussians as shown in Fig. 2.3.6 results in two different sets of data: the slow (low energy) and fast (higher energy) channels. The asymmetry of both the slow and fast channels show a clear dependence on the $1\omega 2\omega$ phase similar to Fig. 2.3.7. The amplitude of the asymmetry β_0 as a function of R for each (2,0) channel is presented in Fig. 2.3.10. Here β_0 is also an increasing function of R at small R. The slow channel is just resolved at about 7.25 a.u. and β_0 increases monotonically with R up to about 8 a.u. when the signal from the (2,0) disappears. The fast channel also increases with R up until about 7.5 a.u. when it reaches a maximum. As R increases, β_0 increases from 0 up to about 0.50 for the (2,0) channels as shown in Fig. 2.3.10, while ϕ_0 stays constant within the error bars (see inset).

Although our two-level model predicts a maximum asymmetry of 1, our experimental setup is not optimized for measuring spatial asymmetry due to the difference in angular acceptance for the forward and backward peaks, discussed above. Therefore, the resulting measured asymmetries may be slightly lower than expected. Some groups use velocity map imaging (VMI) to measure ion yields resulting in asymmetry measurements as high as ± 0.7 [34]. Nevertheless, both of the (2,0) channels show an increase in the amplitude of

the asymmetry as a function of R and a constant ϕ_0. Each channel has a distinct dependence as seen in Fig. 2.3.10, again suggesting the presence of two distinct pairs of CR states. Fig. 2.3.11 shows the results of the β_0 based on the two-level model for two different dipole couplings. The offset in $\beta_0(R)$ as seen in Fig. 2.3.10 could be due to the different dipole couplings of the two states.

Up to this point, the results of the two-level model are still in qualitative agreement with the experimental data and describe the left/right asymmetry measurements. However, the maximum in the amplitude of the asymmetry is not predicted by the model. The molecule *must* approach the separated atom limit at which point there can be no asymmetry, although non-adiabatic effects and dephasing may play a role as well. The R at which the molecule begins to behave as two separated atoms is not well known and the physics in this region may be important in understanding molecules on a fundamental level. The observation of a maximum in β_0 may indicate this transition region at which point our two-level model loses validity as it assumes adiabatic following of the field.

The R dependence of the ionization into the (2,0) channels is also measured. Fig. 2.3.12 shows the ionization rates into the (2,0) channels based on the total counts measured in the TOF. The total counts are found by summing each pair of forward and backward peaks (i.e. the (2,0) slow peaks). The most prominent features are the two peaks of (2,0) occurring at different R's. The R at which the slow peaks show a maximum is around 6.5 a.u. (70 fs) and the fast peaks show a maximum at around 7.7 a.u. (160 fs). Again, the observation of two peaks in the ionization is evidence for populating two different (2,0) channels [21].

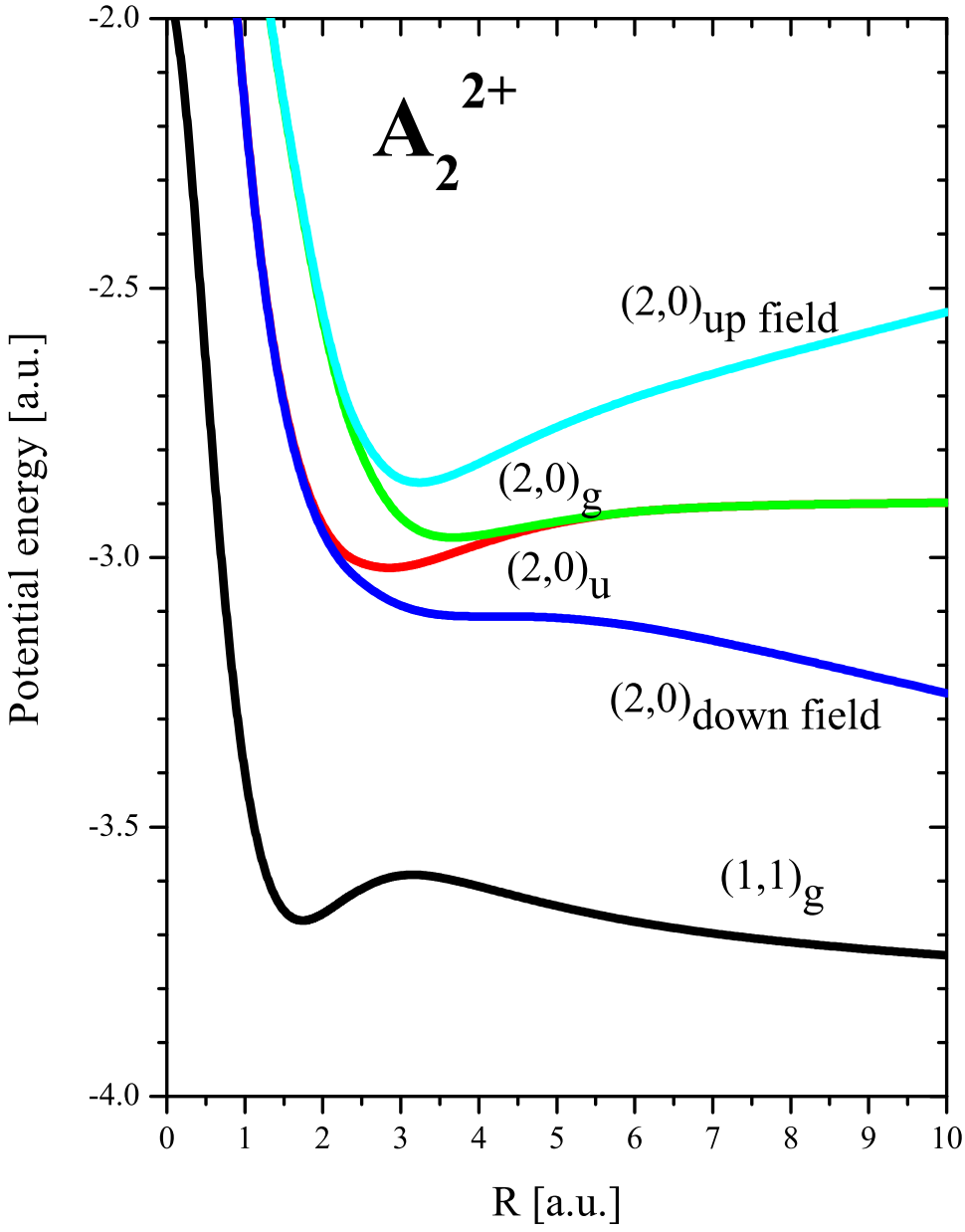

Figure 2.4.1: Quasistatic potential energy curves for arbitrary molecular ion A_2^{2+} without field (*g* and *u* curves) and with an external static field (up field and down field) of 0.07 a.u.

2.4 Discussion

The observation of charge asymmetric dissociation (CAD) channels in homonuclear diatomic molecules presents an interesting challenge to understanding the behavior of molecules in strong laser fields. Most work in this field focuses on the ionization rate of the ground state of the molecule as a function of internuclear separation and alignment and one would not necessarily consider the possibility that this would lead to excitation of the resulting molecular ion. Nevertheless, as mentioned in the Introduction, the ionic states leading to CAD are indeed electronically excited and this excitation energy can be quite substantial (up to 8.7 eV in I_2^{2+} and 30 eV in N_2^{6+}). Thus, we would like to get a better understanding of the mechanism behind this extraordinary degree of excitation.

There are two possible routes to populating the states leading to CAD in even-charged molecules: 1) ionization of the previous charge state directly populates the ionic states, and 2) ionization of the previous charge state leaves the ion in the covalent charge-symmetric ground state and the ion is further excited by the laser field to the high lying ionic states. Both possibilities have connections to prior theoretical work. Bandrauk et al. found that the ionic states play an important role in the ionization of even-charged molecules, but they did not consider ionization *into* the ionic states. It has also been shown that the covalent ground state and gerade/ungerade ionic states form an interesting three-level system that can support very high-order ($>$10) multiphoton transitions [42]. Indeed, evidence was found for a resonant three-photon transition in I_2^{2+} [41]. Nevertheless, we think that it is unlikely that the (2,0) states are being populated by resonant multiphoton transitions in this experiment.

This simple observation of spatially asymmetric dissociation means that both the gerade and ungerade states must be coherently populated such that they add or subtract to produce

the higher charged ion going either forward or backwards with respect to the detector (see Appendix). Since the singlet covalent ground state has gerade symmetry, a single color laser field will resonantly couple to only one of the ionic states (gerade or ungerade), depending on the number of photons involved. This is why a single color cannot produce spatial asymmetry. If the second harmonic is added, the selection rules change, raising the possibility that both gerade and ungerade states can be populated, but only under very restrictive conditions: the number of photons absorbed from the 2ω beam must be odd, so that the number of photons from the 1ω beam is even. With our 800/400 nm $1\omega 2\omega$ beam, this is not possible considering our knowledge of the potential energy curves of the I_2^{2+} molecule, within the range of R that we can probe. Even if an appropriate R existed where both the gerade and ungerade states could be resonantly populated, it would not explain the systematic dependence of the asymmetry on R.

Thus, we return to the first possibility mentioned above. A simple two-electron 1-D model reveals the basic structure of an even-charged molecular ion (Fig. 2.4.1 and Appendix). The (1,1) channel forms the covalent ground state and the (2,0) gerade/ungerade states are the excited CR pair of states. The CR states have two distinctive features. They become completely degenerate at large R and the dipole coupling between them approaches R as R gets large [42]. Thus, if a dc field is applied, the states are barely perturbed at small R and become quite distorted at large R. Moreover, at small R, the states will only be slightly mixed whereas at large R, they become fully mixed. To include ionization, we make the ansatz that the lower of the two field-induced states will be preferentially populated when this charge state is created through ionization. With this ansatz, we can predict the amplitude of the spatial asymmetry as a function of R as follows (Fig. 2.3.9). At small R, there is little mixing of the CR states and only the ungerade state will be populated. Since this state has equal probability of having the electrons on either ion, there will be no spatial

asymmetry. At large R, the states are completely mixed and the lower field-induced state receives all the population. However, this field-induced state is a coherent superposition of the field-free states and this will lead to a maximum spatial asymmetry. Thus, we predict that the spatial asymmetry will start very small at small R and reach a maximum value of 1 at large R. A quantitative calculation of the asymmetry as a function of R is given in the Appendix, within the context of our model. Another consequence of this model is that the phase of the maximum asymmetry will not change as a function of R. This is because the maximum asymmetry will always occur when the field asymmetry is, itself, a maximum. Note, this would not necessarily be true for a resonant multiphoton transition [36].

The above description considered a dc field. In the presence of a single color ac field, the coherent sum of the field-free states will reverse as the field reverses. In other words, the lower field-induced state will lead to a left-going ion for one direction of the field and a right-going ion for the other direction of the field. In this way, the left and right-going states will be equally populated leading to no spatial asymmetry. In the two-color field, one direction is preferred over the other, leading to a preference for the left or right-going ion which will then show a spatial asymmetry.

Our data are consistent with both predictions of the two-level model: the amplitude of the spatial asymmetry β_0 increases with R up to a point and the phase giving rise to the maximum asymmetry ϕ_0 is independent of R. Thus, we conclude that the ionization of I_2^+ can directly populate the excited ionic states of I_2^{2+}. Of course, this implies that if the ionic states are populated, the least bound electron could not have been the one ionized, as, by definition, that would have left the ion in the ground state. This is another example of a phenomena gaining attention lately, namely excitation through ionization [39]. However, we do not see the asymmetry reach the predicted value of 1 at large R. Instead, we find that β_0 goes through a maximum and then decreases toward zero at large R and our model

does not capture this behavior. This is perhaps not so surprising as we have used a dc field and the time independent Schrödinger equation to study dynamics only as a function of R. A more detailed two-level calculation in which the time dependence of the $1\omega 2\omega$ field is applied may provide insight into the observed maximum and subsequent decrease in β_0 as a function of R.

Finally, we return to our observation of additional structure in the TOF spectrum around the (2,0) channel. From the KER measurements, the ionization rates as a function of R, and the spatial asymmetries, we must conclude that we are populating two distinct (2,0) states, each of which is a CR pair. While it is not surprising that there could be many states connected with the (2,0) dissociation limit, to the best of our knowledge, this is the first time more than one state has been identified as a (2,0) dissociation channel.

2.5 A Model Two-Level System

To model the spatial asymmetry of the (2,0) channel, we use the following Hamiltonian that corresponds to two electrons in a 1-D double well potential and captures the ground and ionic state three-level structure of a dication [42]: $H(t) = H_s(t) + H_p(t)$, where $H_p(p_1, p_2, t) = p_1^2/2 + p_2^2/2$ and

$$\begin{aligned} H_s(x_1, x_2, t) \quad = \quad & \frac{-Z}{\sqrt{(x_1 - d)^2 + a^2}} + \frac{-Z}{\sqrt{(x_1 + d)^2 + a^2}} + \\ & \frac{-Z}{\sqrt{(x_2 - d)^2 + a^2}} + \frac{-Z}{\sqrt{(x_2 + d)^2 + a^2}} + \\ & \frac{1}{\sqrt{(x_1 - x_2)^2 + a^2}}, \end{aligned} \tag{2.5.1}$$

$R = 2d$ is the internuclear separation, a is a smoothing parameter, $Z = 2$ is the charge on each atom, and r_1, r_2 (p_1, p_2) are the positions (momenta) of the electrons. This Hamiltonian produces the field-free potential curves show in Fig. 2.4.1.

We then consider just the two-level subsystem, namely the (2,0) g and u states:

$$H_0(R) = \begin{pmatrix} E_u(R) & 0 \\ 0 & E_g(R) \end{pmatrix} \tag{2.5.2}$$

where the eigenstates are $(2,0)_g$ and $(2,0)_u$ (Fig. 2.4.1) and are defined as $|g\rangle$ and $|u\rangle$ as follows:

$$\begin{aligned} H_0 |u\rangle &= E_u |u\rangle \\ H_0 |g\rangle &= E_g |g\rangle \\ |u\rangle &= \begin{pmatrix} 1 \\ 0 \end{pmatrix} \\ |g\rangle &= \begin{pmatrix} 0 \\ 1 \end{pmatrix}. \end{aligned} \tag{2.5.3}$$

The strong field couples the two states resulting in the Hamiltonian:

$$H = \begin{pmatrix} E_u & \Omega \\ \Omega & E_g \end{pmatrix} \tag{2.5.4}$$

where $\Omega \approx \alpha R$ in atomic units and α corresponds to the electric field. For $R > 2$, the dipole matrix element $\langle u| \, r_1 + r_2 \, |g\rangle$ is approximately R [42]. In the presence of the electric field, the potential curves will be modified as shown in Fig. 2.4.1 and are defined as the up field

and down field states. The static field breaks the degeneracy of the g and u levels and the states in Eq. (2.5.3) are no longer eigenstates of the Hamiltonian Eq. (2.5.4). To find the new eigenstates in the field we first find the eigenvalues of Eq. (2.5.4) and define them as:

$$\lambda_{\pm} = \Sigma \pm \Delta \sqrt{1 + \left(\frac{\Omega}{\Delta}\right)^2} \tag{2.5.5}$$

$$\Sigma \equiv \frac{E_u + E_g}{2}$$

$$\Delta \equiv \frac{E_u - E_g}{2} \tag{2.5.6}$$

where λ_+ (λ_-) corresponds to the up field (down field) quasistatic energy. We define the eigenstates of Eq. (2.5.4) as $|\psi^+\rangle$ for the upfield state associated with λ_+ and $|\psi^-\rangle$ for the downfield state associated with λ_- in terms of the original basis states in Eq. (2.5.3) as:

$$\begin{aligned} \left|\psi^+\right\rangle &= C_{g+}\left|g\right\rangle + C_{u+}\left|u\right\rangle \\ \left|\psi^-\right\rangle &= C_{g-}\left|g\right\rangle + C_{u-}\left|u\right\rangle . \end{aligned} \tag{2.5.7}$$

Eqs. (2.5.5) and (2.5.7) allow us to solve for the amplitudes under the normalization condition that

$$C_{g\pm}^2 + C_{u\pm}^2 = 1 \tag{2.5.8}$$

where the amplitudes in Eq. (2.5.7) are defined as

$$\begin{aligned} \frac{C_{g+}}{C_{u+}} &= \frac{1 + \sqrt{1 + \left(\frac{\Omega}{\Delta}\right)^2}}{\left(\frac{\Omega}{\Delta}\right)} \equiv N_+ \\ \frac{C_{g-}}{C_{u-}} &= \frac{1 - \sqrt{1 + \left(\frac{\Omega}{\Delta}\right)^2}}{\left(\frac{\Omega}{\Delta}\right)} \equiv N_- . \end{aligned} \tag{2.5.9}$$

The amplitudes in Eq. (2.5.7) can then be found from Eqs. (2.5.8) and (2.5.9):

$$C_{g\pm} = \frac{N_\pm}{\sqrt{1+N_\pm^2}}$$
$$C_{u\pm} = \frac{1}{\sqrt{1+N_\pm^2}}. \tag{2.5.10}$$

The eigenstates of Eq. (2.5.4) in terms of the field-free $|g\rangle$ and $|u\rangle$ basis are therefore

$$\left|\psi^+\right\rangle = \frac{N_+}{\sqrt{1+N_+^2}}|g\rangle + \frac{1}{\sqrt{1+N_+^2}}|u\rangle$$
$$\left|\psi^-\right\rangle = \frac{N_-}{\sqrt{1+N_-^2}}|g\rangle + \frac{1}{\sqrt{1+N_-^2}}|u\rangle\,. \tag{2.5.11}$$

At this point we have a full description of the the two-level system in the laser field. We propose that there will be preferential ionization to the down field state $|\psi^-\rangle$ since it lies at a lower energy than the up field state of the system. Since $|\psi^-\rangle$ contains both $|u\rangle$ and $|g\rangle$ components, population of this state can lead to spatially asymmetric dissociation. In the laser field, the eigenstates are a coherent superposition of the field-free states according to:

$$|L\rangle = \frac{|g\rangle + |u\rangle}{\sqrt{2}}$$
$$|R\rangle = \frac{|g\rangle - |u\rangle}{\sqrt{2}} \tag{2.5.12}$$

where $|L\rangle$ and $|R\rangle$ are left and right going states.

The sudden projection of the down field $|\psi^-\rangle$ onto this basis gives us the amplitudes of

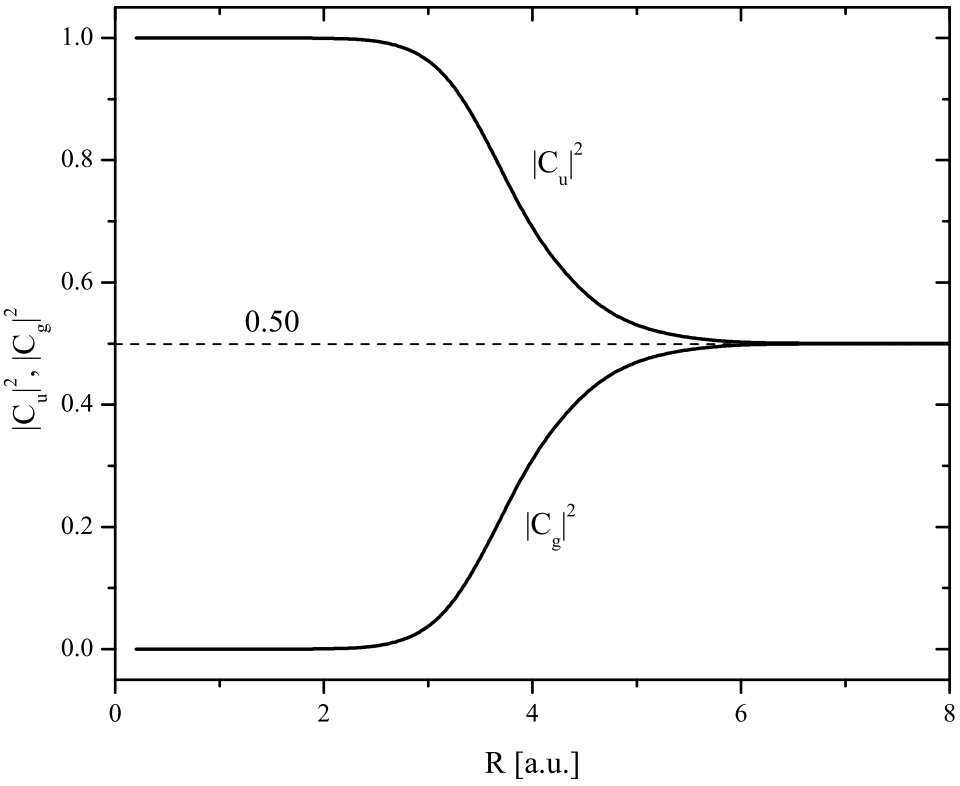

Figure 2.5.1: Probabilities based on the coefficients of the field-induced state $|\psi^-\rangle$ in Eq. (2.5.7). As the states become degenerate, the populations approach 50%.

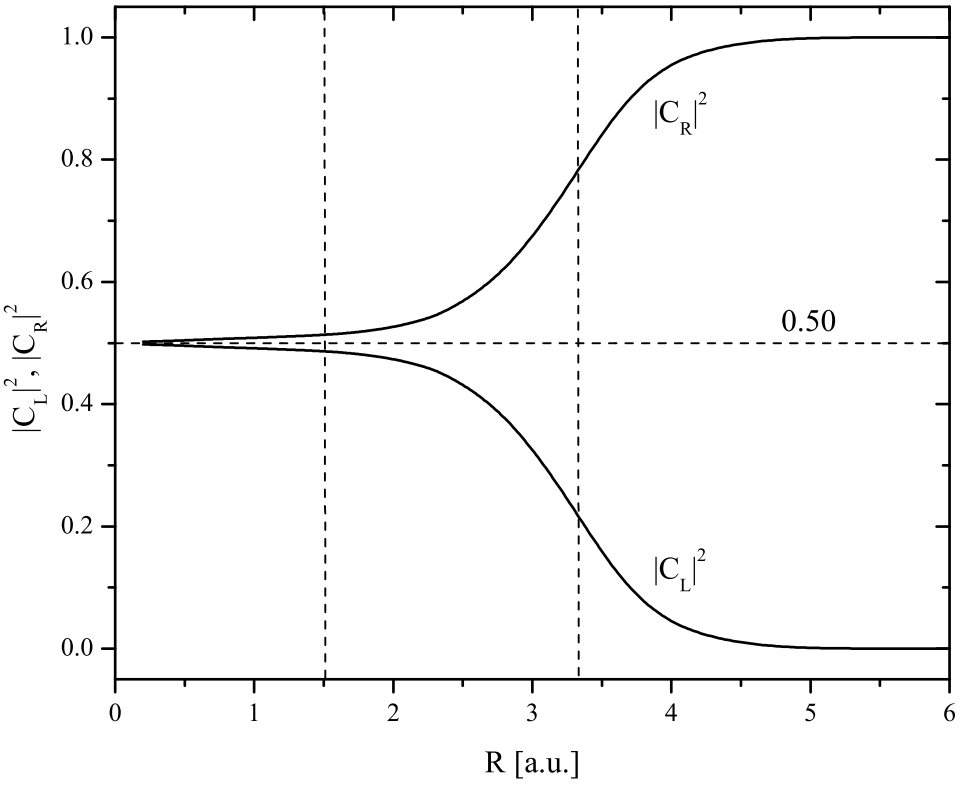

Figure 2.5.2: Probabilities based on the coefficients of Eq. (2.5.13) which are used to calculate β_0. The range for the minimum and maximum asymmetries measured experimentally are indicated by the dashed vertical lines. At small R β_0 is small and as R increases β_0 approaches a maximum of one as shown in Fig. 2.3.9.

the electronic wavefunctions going to the left and right:

$$\langle L|\ \psi^{-}\rangle = \frac{C_{g-} + C_{u-}}{\sqrt{2}} \equiv C_L$$
$$\langle R|\ \psi^{-}\rangle = \frac{C_{g-} - C_{u-}}{\sqrt{2}} \equiv C_R \tag{2.5.13}$$

where C_L is the amplitude of the wavefunction in the left well and C_R is the amplitude of the wavefunction in the right well. Finally, we can calculate the spatial asymmetry based on the two-level system by squaring the amplitudes found in Eq. (2.5.13) and using Eq. (2.1.2). The populations in the left and right wells are shown in Fig. (2.5.2). The amplitude of the asymmetry β_0 using the results of Eq. (2.5.13) is shown in Fig. 2.3.9.

2.6 Conclusion

We have measured the spatial asymmetry of the CAD channel of I_2^{2+} as a function of internuclear separation by first exciting the neutral molecule to the B state and letting it evolve in time. By varying the delay of a $1\omega 2\omega$ probe pulse, we measure the asymmetry as a function of internuclear separation for different values of the $1\omega 2\omega$ phase. The maximum amplitude of the spatial asymmetry increases with R, goes through a maximum, and then decreases while the phase of the maximum asymmetry is constant. By comparing these results to a simple two-level model in a dc field, we conclude that the molecules are ionized directly into the field-dressed ionic states of the dication. Although our two-level model captures many of the characteristics of the spatial asymmetry, it appears to break down as it does not predict the behavior of the asymmetry for all observed values of R. In addition, we find evidence for two different states correlating with the I^{2+} + I dissociation limit.

Finally, we observe spatial asymmetries for the states with dissociation limits with a charge difference of 2, but not for a charge difference of 1.

Chapter 3

Multielectron Effects in Charge Asymmetric Molecules Induced by Asymmetric Laser Fields

3.1 Introduction

The interaction of molecules with a strong laser field can lead to interesting nonperturbative effects such as inner-orbital ionization [44–49], high-harmonic generation (HHG) [50–52], enhanced ionization (EI) [53–59], and charge asymmetric dissociation (CAD) of ionic fragments [61–63]. The CAD channels are particularly interesting as they indicate a high degree of electronic excitation over the ground state charge symmetric dissociation (CSD) channels [61], involve electron charge transfer and electron rearrangement [64–68], and have been used to demonstrate theories of EI and electron localization (EL) [55]. Further, the ion fragments produced through CAD exhibit spatial asymmetry (SA) in two-color, asymmetric $1\omega 2\omega$ laser fields [69–72]. This is significant because it allows us to directly

observe charge transfer interactions which may otherwise go unnoticed.

Charge transfer in ionization processes has proved to be an important and unavoidable mechanism in strong field physics. The intense laser field can cause field-induced charge transfer between the nuclei and result in a strong electron-electron correlation [65]. It has been shown that charge transfer is possible between the symmetric and asymmetric states of even-charged diatomic molecules [73]. Further, upon ionization by a strong field the ionized electron may still interact with the parent ion and studying the amplitude and phase of this interaction has led to significant progress in understanding HHG [74, 75] and in turn, molecular structure and electronic rearrangement [52, 68]. For diatomics, the single-active-electron approximation has often been used as a first step in characterizing ionization, but the application to more complicated multi-electron polyatomic molecules is unlikely to result in an accurate model [76, 77]. As such, studying charge transfer in simpler systems like diatomics is an important step in understanding multi-electron dynamics not only in ionization and dissociation, but in applications of attosecond physics and HHG.

In this work, we study the *R*-dependence of charge transfer through the ionization of the (2,0) to (2,1) dissociation channel in I_2 [throughout this work (n,m) designates the $I_2^{(n+m)+} \rightarrow I^{n+} + I^{m+}$ dissociation channel and indicates if the charge is on the left (n) or the right (m) atom]. In a symmetric (single color) field it would not be clear if the I^{0+} were simply ionized to I^{1+} (Fig. 3.1.1(a)) or if there was an electron rearrangement with ionization where $I^{0+} \rightarrow I^{2+}$ and $I^{2+} \rightarrow I^{1+}$ (Fig. 3.1.1(b)). Schematically, these different ionization

pathways are described by Eq. (3.1.1):

$$\begin{array}{ccccc} & A & & B & \\ (0,2) & \Longrightarrow & (1,2) & \longleftarrow & \\ & \Longrightarrow & (2,1) & \longleftarrow & (2,0). \\ & B & & A & \end{array} \tag{3.1.1}$$

With symmetric fields, the (1,2) and (2,1) signals will always be equal, providing no indication of the relative strengths of the single-electron ionization (A) and charge transfer with ionization (B) mechanisms in Eq. (3.1.1). However, a $1\omega 2\omega$ field can preferentially ionize one well over the other, enhancing, for example, the double arrows over the single arrows in Eq. (3.1.1), immediately revealing the relative strength of the two processes.

An added complication is that molecular ionization in a strong field is also sensitive to the laser pulse duration, as a molecule will expand at different rates depending largely on its mass. Although CAD has been seen with long and short pulses [63, 78], in both light [62, 71] and heavy molecules [61, 64], the R-dependence of a process cannot be seen directly if ionization and dissociation occur at the same time during the laser pulse. For this reason, we chose to study I_2 in a pump-probe configuration.

In previous experiments [72], we studied SA in the *production* of the (2,0) CAD channel in I_2 as a function of internuclear separation R in a $1\omega 2\omega$ field. We found that while the (2,0) channel is produced at R_e, there is no SA. As the molecule dissociates from R_e, the SA increases reaching a maximum around R_c and drops off at larger R. These results would appear to support recent measurements in N_2 [71], where both the (2,0) and (2,1) channels showed SA. While the experiments performed in I_2 are time-resolved and the measurements described for N_2 are not, there are still two problems. We have shown [78]

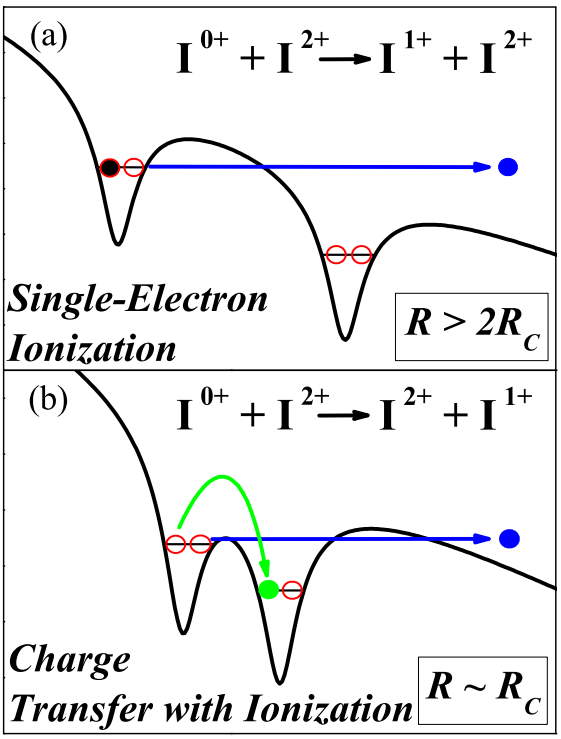

Figure 3.1.1: One-dimensional double-well potential schematic showing the (a) single-electron ionization and (b) ionization with charge transfer processes near R_c and $2R_c$. The initial charge state (0,2) has two electrons in the upfield well so that the upfield atom has a 0^+ charge and the downfield ion has a 2^+ charge. The straight arrow indicates ionization and the curved arrow indicates charge transfer of the electron which occurs near R_c and is suppressed at larger R.

that there is no expansion of the N_2 molecule to R_c until *after* N_2^{2+} is produced and therefore the (2,0) must be produced near R_e. Also, SA in (2,1) was not seen in I_2. Thus, SA cannot result from the spatially asymmetric *production* of (2,0) at R_c in N_2.

To resolve these issues, we study the possibility of SA in the *depletion* of the (2,0) channel as a function of R in I_2 [72]. If depletion occurs, SA in N_2 could be explained by the spatially symmetric (SS) production of (2,0) at R_e and SA depletion at R_c as the N_2^{2+} molecule expands on the (2,0) potential energy curve during the laser pulse. Any SA depletion of (2,0) must appear as SA enhancement in (2,1). In fact, the depletion of (2,0) in I_2^{2+} has been observed and used to demonstrate theories of one-electron EI at R_c [55]. In the simplest interpretation, the neutral atom is ionized to I^{1+} and, if done so with an asymmetric laser field, both the (2,0) and (2,1) channels would show SA but in opposite directions (based on the direction of the I^{2+} ion). Since the (2,0) and (2,1) channels in N_2 show the same direction for the asymmetry [71], either depletion is not the mechanism for the SA, or the EI experiment has a more subtle interpretation than previously thought. We will show that, indeed, the (2,0) channel can be depleted asymmetrically, the (2,1) channel does show SA, and that, at R_c, two-electron charge transfer is so strong that the induced asymmetry in the (2,1) channel is in the counter-intuitive direction (in the context of depletion and Fig. 3.1.1(b)) and, thus, consistent with the directions observed in N_2 [71]. These conclusions are supported by time-dependent calculations of two-electrons in a double-well potential.

3.2 Experiment and Results

The experiments are performed with a Ti:sapphire laser system (Spectra-Physics) at a 1 kHz repetition rate producing up to 800 μJ per pulse in 45 fs with a central wavelength of 800 nm. The beam is split to allow for pump-probe measuerments. Both the pump and probe pulses are linearly polarized parallel to the time of flight (TOF) axis. The 800 nm pump pulse intensity is 2.0×10^{14} W/cm^2 and the $1\omega 2\omega$ probe intensity is 1ω: 6.5×10^{13} W/cm^2 and 2ω: 1.6×10^{13} W/cm^2. The $1\omega 2\omega$ pulse is produced by frequency doubling the 800 nm (1ω) beam in a 250 μm-thick β-barium borate (BBO) crystal and spatially separating the two colors in a Mach-Zehnder interferometer (details in [72]). To produce the maximum field asymmetry, the energies of the probe pulses are set at a 4:1 1ω:2ω ratio. The relative phase ϕ between the two pulses is stable to within 5°. The beams are focused by a spherical silver mirror inside an ultra-high vacuum chamber with a base pressure of 10^{-9} torr. Iodine gas is effusively leaked into the chamber at room temperature to a pressure of 10^{-7} torr. The I^{2+} ion signals are detected with a Wiley-McLaren [79] TOF spectrometer. We record pump-probe TOF spectra for two phases of the $1\omega 2\omega$ field differing by π as well as the single pulse $1\omega 2\omega$ TOF spectrum.

A typical TOF data set for a single $1\omega 2\omega$ phase is shown in Fig. 3.2.1. The pump pulse launches dissociating wavepackets in the (2,0) channel. As the molecule dissociates, the time delayed probe pulse further ionizes (2,0) to (2,1) (see Fig.3.2.2). This ionization appears as ”tracks” in the TOF spectrum from about 100 to 450 fs in a region where the kinetic energy release (KER) is between the (2,0) and (2,1) channels observed with a single pulse [80]. The (2,1) KER decreases as the probe delay increases. There is a region of EI of (2,0) from around 120 fs to 220 fs in which the molecule passes through R_c. Here, the (2,0) channel is depleted by approximately 50% relative to the asymptotic population observed

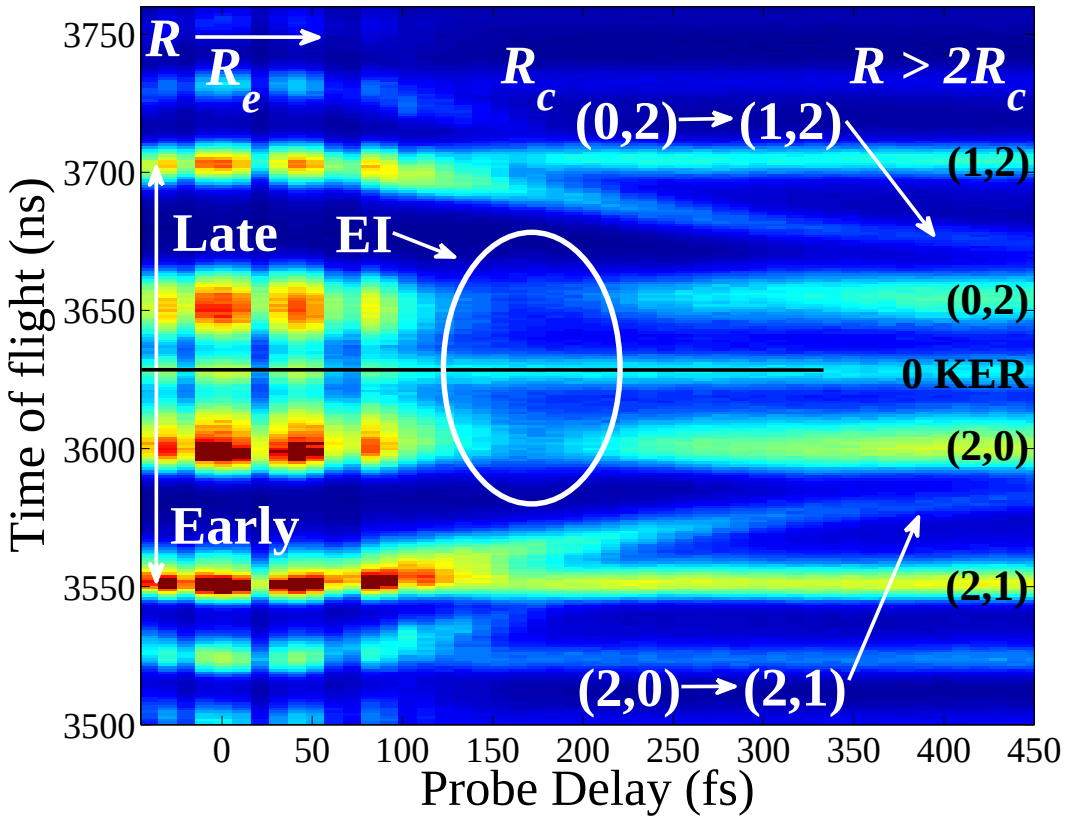

Figure 3.2.1: Time of flight spectrum for I^{2+} at a single phase of the $1\omega 2\omega$ field as a function of probe delay with a step size of 10 fs. The three regions of R correspond approximately to R_e (0 fs), R_c (120-220 fs), and $R > 2R_c$ ($\sim$350-450 fs). The coherent structure from -50 fs to 100 fs is due to the interference of the pump and probe pulses near zero time delay.

at large time delays. The depletion reaches a maximum at ∼170 fs, consistent with the first observation of EI in I_2 [55] and subsequent observations [63, 80]. Starting at about 100 fs delay, there is an enhancenment of (2,1) population which peaks at the maximum depletion of (2,0).

The SA of the (2,0) and (2,1) channels is highlighted by changing the phase of the $1\omega 2\omega$ field by π and subtracting one data set from the other, shown in Fig. 3.2.3. Clear asymmetry is seen between the early and late arriving I^{2+} signals coming from the (2,0) channel, resulting from SA in the depletion of this channel. The depletion of the (2,0) signal must end up in the (2,1) signal and, as the depletion shows SA, the increase in the (2,1) signal should also show SA, as is observed. The remarkable feature of these data is that the SA of the (2,1) signal changes sign relative to the (2,0) signal as a function of pump-probe delay or, correspondingly, R.

The data can be divided into three regions: R_e, R_c, and $R > 2R_c$ (as labeled in Fig. 3.2.1). The behavior at R_e is best captured with a single $1\omega 2\omega$ pulse and while the (2,0) dissociation channel is observed, no SA is seen in this signal (not shown). At $R > 2R_c$, the SA of the (2,1) signal is in the opposite direction of the (2,0) asymmetry (Fig. 3.2.3). This is easily explained in a one-electron picture: assume the maximum electric field points to the left (Fig. 3.1.1(a)). Then, the left potential well will be the upfield well (for an electron). If the two electrons start out in the left well, which we will designate as (0,2), this configuration will be preferentially ionized over the (2,0) configuration, where the two electrons are on the right. The (0,2) configuration will be depleted relative to the (2,0) and the (2,0) signal will dominate. At the same time, the (0,2) configuration will ionize to the (1,2), which will, in turn, dominate over the (2,1). So, the (2,0) and (1,2) signals will be the largest and the I^{2+} ions will come out in opposite directions, as is seen at large R (400 fs) in Fig. 3.2.4.

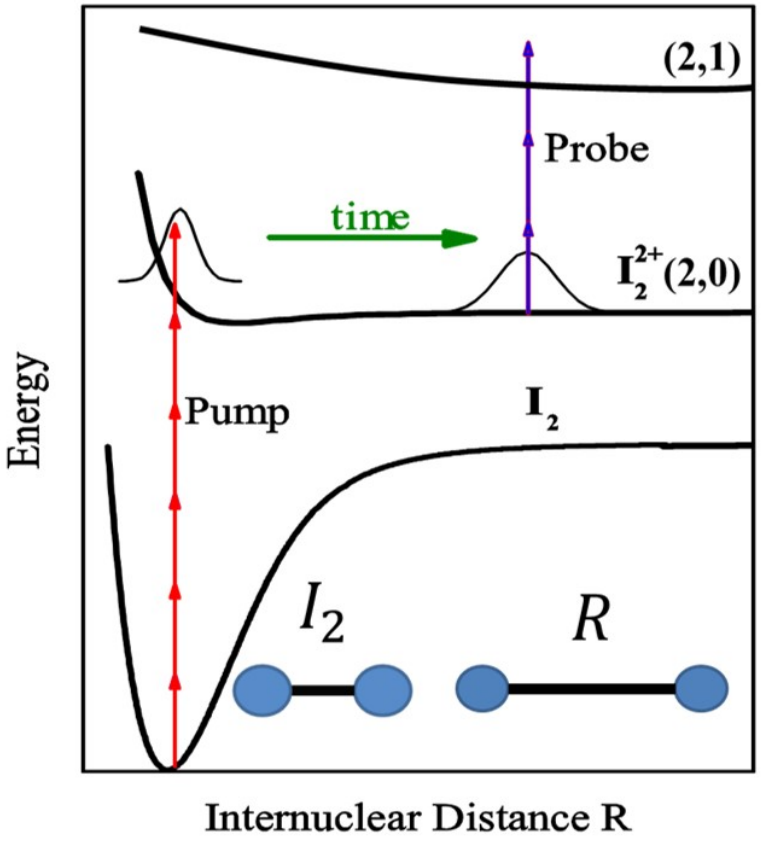

Figure 3.2.2: Schematic of the pump-probe measurement in I_2.

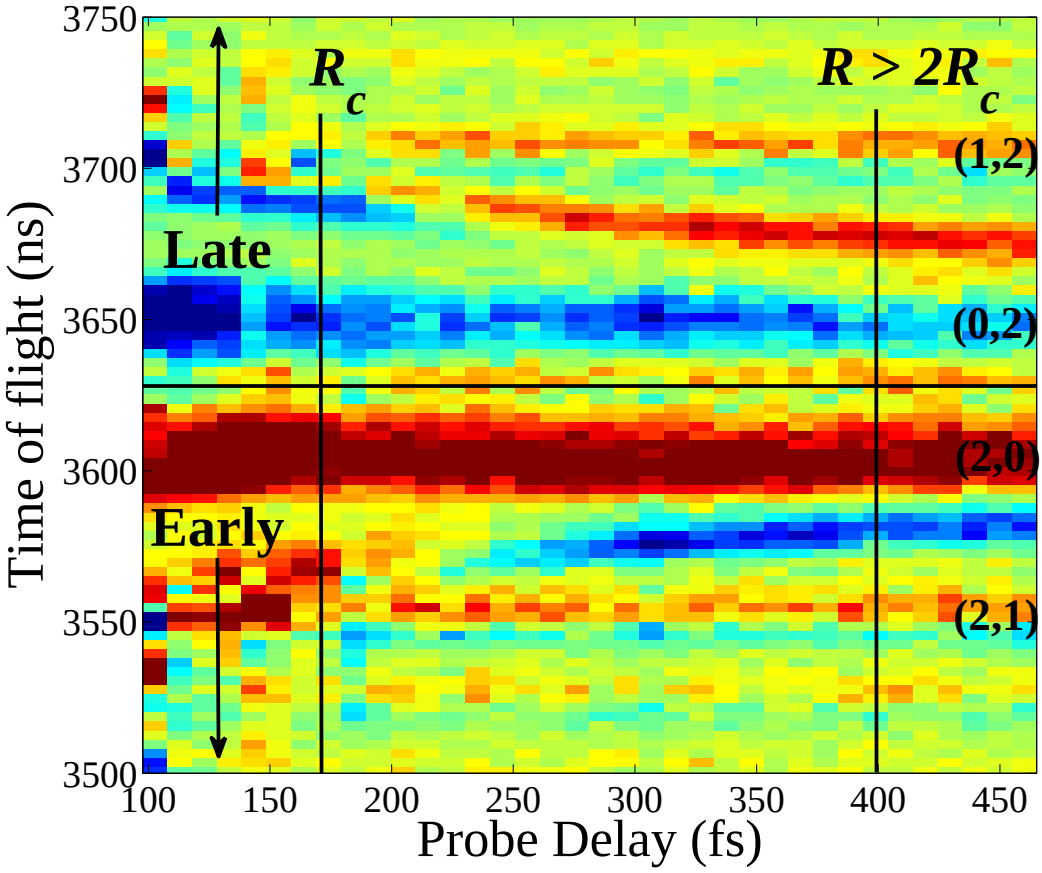

Figure 3.2.3: Difference between I^{2+} signals when the $1\omega 2\omega$ phase ϕ is rotated by π showing the spatial asymmetry (SA) as a function of probe delay. Red is positive signal and blue is negative. The vertical lines correspond to 170 fs ($\sim R_c$) and 400 fs ($\sim 2R_c$).

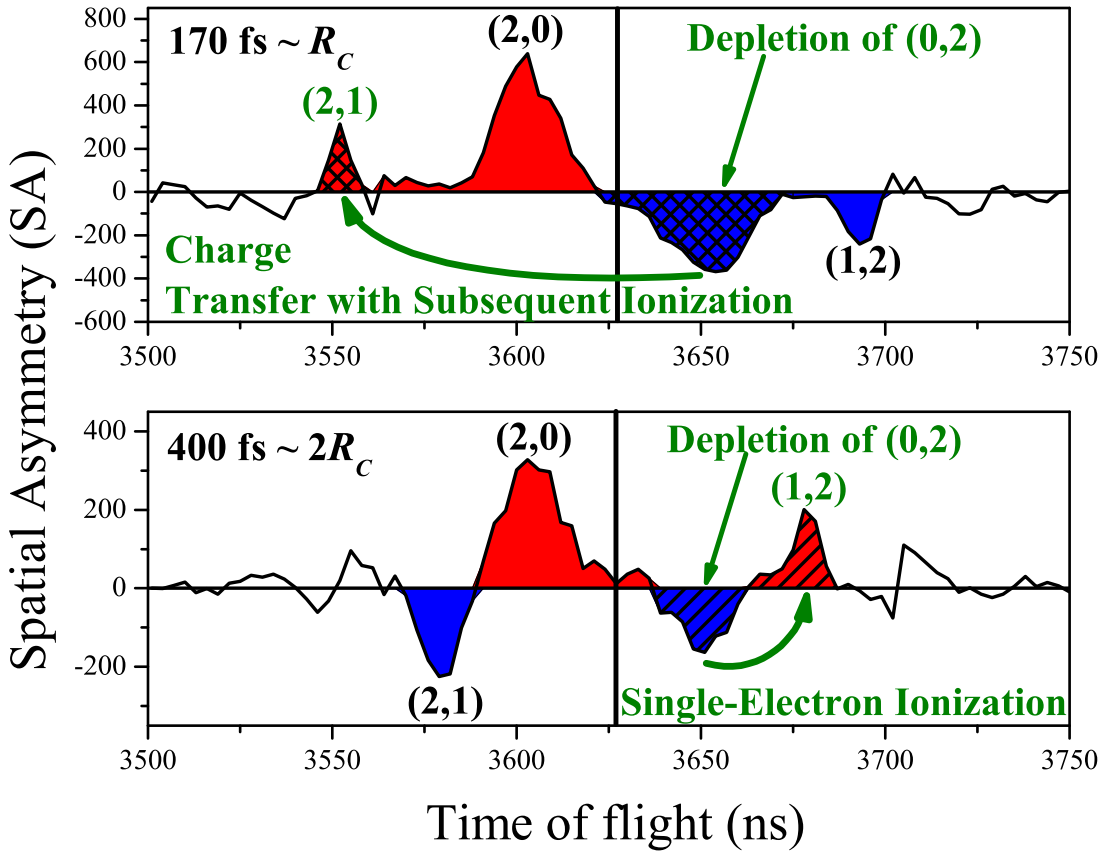

Figure 3.2.4: Spatial asymmetry for I^{2+} for probe delays of 170 fs and 400 fs as noted in Fig. 3.2.3. The SA of (2,1) at 170 fs (top) is in the same direction as (2,0) , while the SA of (2,1) at 400 fs (bottom) is in the opposite direction of (2,0). The curved arrows indicate the ionization pathways based on the depletion of (0,2). Near R_c the depletion of (0,2) corresponds to an enhancement of (2,1). As R increases beyond R_c the depletion of (0,2) corresponds to an enhancement of (1,2).

Finally, at R_c, the situation is quite different. As before, the (0,2) configuration will be preferentially ionized, leaving the (2,0) signal stronger than the (0,2). As expected, this aspect is independent of R as seen by the relatively constant asymmetry in Fig. 3.2.3. However, at the same time, we find that the (2,1) signal is stronger than the (1,2). The only way this is possible is if the (0,2) configuration ionizes to the (2,1). This must involve a two-electron process: one of the electrons on the left ionizes while the second electron transfers to the right well (Fig. 3.1.1(b)). This additional charge transfer step cannot be detected with a spatially symmetric (1ω) pulse. A direct comparison of the SA observed at 170 fs ($\sim R_c$) and 400 fs ($\sim 2R_c$) is given in Fig. 3.2.4.

3.3 Simulations and Discussion

Given the counter-intuitive nature of this last observation, we solved the time-dependent Schrödinger equation (TDSE) through the wave packet propagation of two electrons in a one-dimensional double-well soft Coulomb potential for a model molecular ion A_2^{2+} in an asymmetric $1\omega 2\omega$ field [65, 81–83]. Within this model, electron correlation is included exactly. The two-electron wavefunction is spatially symmetric resulting in singlet states only. A pulse duration of 10 fs was used, but runs with longer pulse durations exhibited qualitatively similar results. We kept the maximum field direction constant (to the left) and calculated the total ionization probability for the (2,0) and (0,2) configurations. An absorbing region is placed around the edge of the spatial grid to simulate ionization. Single electron ionization is characterized by one electron coordinate becoming large while the other coordinate remains small. When one electron reaches the absorber, we record the position of the second, still bound electron, to determine which well it is left in. This

information is plotted around the edges of the grids in Fig. 3.3.1. We are then able to observe the two-electron wavefunction evolution as a function of time for various R while monitoring the ionization.

The results of the simulations are given in Fig. 3.3.1 for two different R values at the beginning, peak and end of the laser pulse. The peak electric field is shown in Fig. 3.3.1 (b) and (e) pointing to the left in the direction of the upfield well. The two-electron wavefunction is initially placed in the upfield well of the molecule as shown in Fig. 3.3.1(a) and (d). We also ran the simulations for ionization in the downfield well. The ionization probability of the molecule is identified by absorption at the grid boundary as shown in Fig. 3.3.1(b), (c), (e), and (f) and allows us to see which ionization pathway (described by Eq. (3.1.1)) is dominant as a function of R. In this figure, ionization leaving the bound electron with a positive coordinate requires electron transfer in addition to ionization.

The values of $R = 6$ and 10 au correspond qualitatively to small (between $\sim R_c$ and $2R_c$) and large R ($R > 2R_c$), respectively. In both trials of R, the (0,2) configuration had a greater ionization probability than the (2,0), consistent with the observed constant SA in the (2,0) channel in Fig. 3.2.3. We find that for $R = 10$ au (Fig. 3.3.1(d)-(f)), single-electron ionization is dominant from the upfield well as the ionization probability found at the absorber in Fig. 3.3.1(f) is much higher at A than at B (A and B are as defined in Eq. (3.1.1)). The (0,2) channel is ionized to the (1,2) and is in agreement with the observations of EI in which the upfield well ionizes more strongly than the downfield well. Here, the 2^+ ion helps the laser to ionize the upper well. If the molecule starts in the downfield well, the 2^+ ion works against the field and inhibits ionization. The large separation of the nuclei results in a broad internal barrier such that electron localization occurs in the upfield well and any two-electron effects become negligible. Thus, at large R, the bound electron stays in the same well as was initially populated (Fig. 3.3.1(f)). At $R = 6$ au or

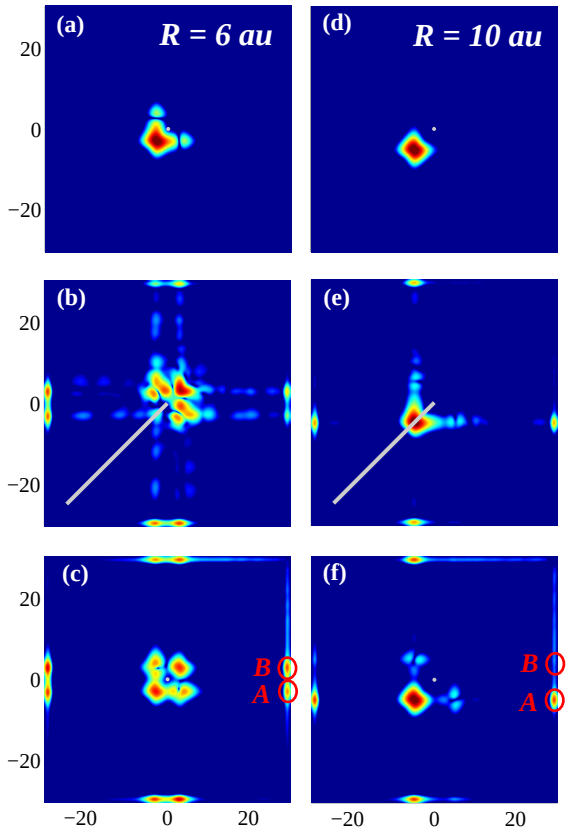

Figure 3.3.1: Simulation results for the two-electron wavefunction probability densities (plotted on log scale) initially placed in the upfield well (0,2) at $R = 6$ and 10 au (a),(d) prior to the pulse, (b),(e) at the peak of the pulse, and (c),(f) at the end of the pulse. The bar in (b) and (e) represents the peak electric field strength and direction. The ionization probabilities are circled in (c) and (f) showing single-electron ionization (A) and ionization with charge transfer (B) where A and B are defined in Eq. (3.1.1). The axes are the coordinates of the two electrons in atomic units. The peak electric field is 0.05 au ($I \approx 9 \times 10^{13}$ W/cm^2) and the pulse duration is 10 fs.

equivalently, the region around R_c, (0,2) is still ionized more strongly than (2,0), but ends up as (2,1) more often than (1,2). As shown in Fig. 3.3.1(a)-(c), there is a large amount of electronic charge transfer between the upfield and downfield wells of the molecule. In fact, this two-electron charge transfer is the dominant mechanism through which ionization proceeds. The ionization probability found at the absorber boundary is actually larger for the ionization with charge transfer pathway (*B* in Fig. 3.3.1(c)) than for the single-electron ionization pathway (*A* in Fig. 3.3.1(c)) and leaves the remaining electron in the opposite well. Close inspection of the time-dependent calculations suggest that the covalent ground state (1,1) is first strongly populated, moving one electron across the molecule. Then, the upper well is further ionized leading to the counter-intuitive (2,1) channel. It should be noted that this two-electron effect is observed in the simulations even with a symmetric laser field. The simulations support the experimental results shown in Fig. 3.2.4 where strong electronic charge transfer is the mechanism responsible for the observed SA of (2,0) near R_c.

Our results impact the interpretation of two previous experiments: observations of SA in N_2 [71] and measurements of EI in I_2 [55]. It has been suggested that the SA in N_2 is produced at R_c. This is reasonable as our previous work [72] shows that (2,0) can be produced asymmetrically at R_c. However, the N_2 molecule does not expand to R_c until *after* N_2^{2+} is created [78]. Since the N_2^{2+} molecule is created before expansion to R_c, the (2,0) channel must first be created spatially symmetric near R_e. Based on our new measurements, we propose that the observed SA comes from the spatially asymmetric depletion of (2,0) once it moves through R_c. However, EI and EL were originally discussed as one-electron effects where (2,0) would ionize to (2,1) and not (1,2) although these two possibilities, the latter being a two-electron effect, could not be distinguished without a $1\omega 2\omega$ field. This description would lead to (2,0) and (2,1) coming out in opposite directions, based

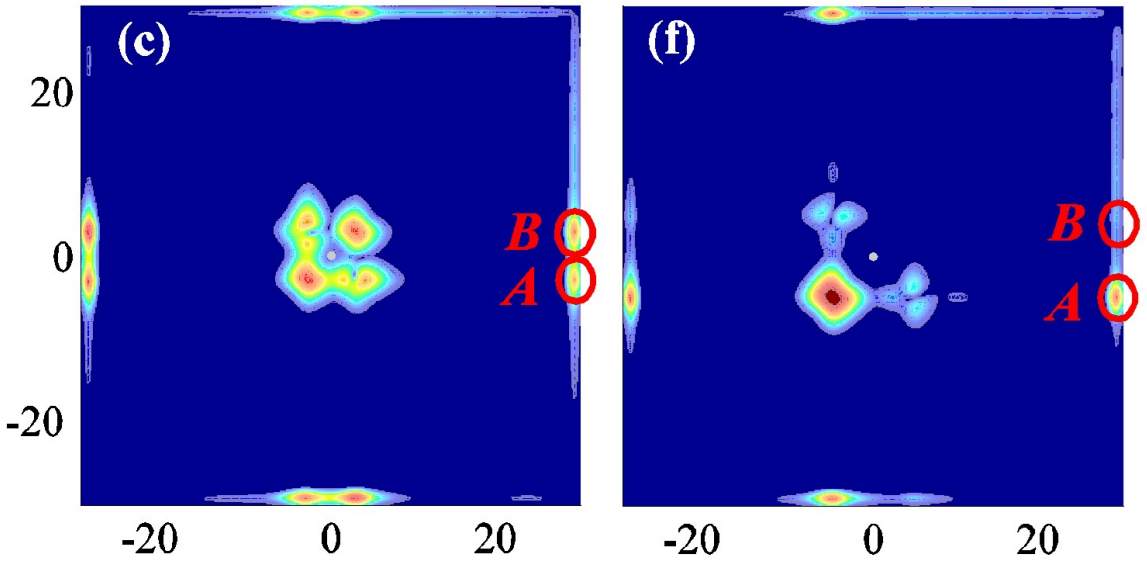

Figure 3.3.2: Close up of simulation data. The ionization probabilities are circled showing single-electron ionization (A) and ionization with charge transfer (B) where A and B are defined in Eq. (3.1.1). The axes are the coordinates of the two electrons in atomic units.

on measurements of the I^{2+} ion. The results of our experiment and simulations indeed show that at large R, two-electron effects are negligible and single electron ionization is an accurate description of the dynamics such that (2,0) ionizes to (2,1), consistent with [55]. However, the single electron description gives the wrong directions based on observations of N_2 where (2,0) and (2,1) come out in the same direction. Our conclusions based on the measurements of I_2 and simulations near R_c are actually consistent with observations in N_2 as the strong two-electron charge transfer results in counter-intuitive ion yields and the (2,0) and (2,1) are in the same direction. Therefore, two-electron charge transfer must be the mechanism by which (2,0) is asymmetrically depleted near R_c and ionized to (1,2).

3.4 Conclusion

In conclusion, we have directly observed multi-electron effects both experimentally and theoretically in the asymmetric depletion of the (2,0) channel of I_2^{2+}. The dynamics of two-electron charge transfer produce the dominant pathway for ionization of the molecule at small internuclear separations around R_c. As R gets larger and the molecule expands, the two-electron effects become negligible and the one-electron description of EI sufficiently describes the ionization dynamics.

Chapter 4

Velocity Map Imaging of the HOMO and HOMO-1 Orbitals of I_2 using Fourier Transform Spectroscopy

4.1 Inner Orbital Ionization

The use of a strong laser field to ionize molecules can result in multiple electrons being removed from the valence orbitals. Since the first observation of inner orbital ionization of N_2 by strong laser pulses [89], there has been much interest in the influence of inner orbitals in ionization and high harmonic generation (HHG). The highly excited states associated with charge asymmetric dissociation (CAD) are expected to be from ionizing orbitals which lie deeper than the outer most valence (those with the lowest ionization potential) [80], [64]. Interference of molecular orbitals [90] depends sensitively on the orbital structure and electron recombination with parent orbitals [91] in harmonic generation can be used to recreate the three-dimensional orbital structure. Although multiple electrons may be ionized by the

strong field, single electron ionization is the critical first step in high harmonic generation as it is the recollision of this electron with its parent ion that is used in imaging and orbital reconstruction. Further, understanding the influence of molecular orbitals will help to improve the computational efforts used in describing ionization and molecular dynamics including molecular-ADK and density functional theory (DFT).

In general, the spectra obtained in strong field ionization of molecules are believed to be dominated by the ionization of the highest occupied molecular orbital (HOMO). Many experiments operate in the tunnel ionization regime (with near IR laser pulses, for example) such that the ionization rate depends exponentially on the ionization potential. The orbitals with the lowest ionization potentials will therefore be preferentially selected. This has been observed to be true in general, but recent work in HCl, N_2, and O_2 has shown that the HOMO is not the only contributor to harmonic generation [92, 93, 97] and that the inner orbitals are important as well.

Although the contribution of the inner orbitals is often small in the diatomics such as HCl and N_2, our recent work in I_2 has shown that the inner orbitals are actively and strongly involved in ionization. The four valence orbitals of I_2 are $\sigma_g^2\pi_u^4\pi_g^4\sigma_u^0$ and are pictured in Fig. 4.2.1. The most deeply bound HOMO-2 σ_g orbital has been identified in ionizing the neutral [49]. Although this is an inner orbital, the branching ratio of single electron ionization shows that this is actually the dominant pathway with a single near-IR ultrafast laser pulse. This orbital also exhibits a critical region of ionization as a function of R, R_c, where the ionization rate shows a large increase. The σ_u orbital, or the lowest unoccupied molecular orbital (LUMO) has been identified as the B state of I_2. This orbital also shows evidence of an R_c in which the ionization rate is strongly enhanced. The angular distribution measurements of the σ_u orbital showed a $cos^2(\theta)$ dependence, as expected for this symmetry, confirming the orbital from which the ionization occurred. We are left with

the task of characterizing the HOMO (π_g) and HOMO-1 (π_u) orbitals of I_2 which exhibit different symmetries. A schematic of the inner orbitals of I_2 is given in Fig. 4.2.2.

The ionization yields and angular distributions of the ionic fragments allow for identification of the structure of the molecular orbital from which the electron was removed. Recent work has argued that measuring the ionization rates from molecules can be used to map the geometry of the orbital being ionized [93, 94]. The method of laser-induced electron diffraction (LIED) and tunneling can ionize electrons, accelerate them, and create recollisions and diffraction from the parent ion within a half cycle of the laser period. The electrons may then provide detailed structural information about the molecular orbitals by investigating the momentum distribution. A simplistic and intuitive picture of the ionization rate is then a minimum ionization when the laser field lies along (parallel) the nodal plane of an orbital and a maximum when aligned with the most spatially extended components of the orbital [95]. However, disagreements between experiment and theory, in CO_2 for example [96], have led to developing the picture of ionization further such that multiple orbitals may need to be included in the theoretical description [97]. The large branching ratio of the HOMO-2 observed in I_2 and the evidence of inner orbital ionization in the above mentioned smaller molecules indeed suggest that multiple orbital ionization is an important effect in strong field ionization and HHG.

4.2 Motivation and Background

In order to investigate state-specific ionization of molecular orbitals, we have developed a velocity map imaging (VMI) detector to record ion signals with pump probe spectroscopy. As discussed earlier, the VMI detector is capable of measuring a projection of a 3-D mo-

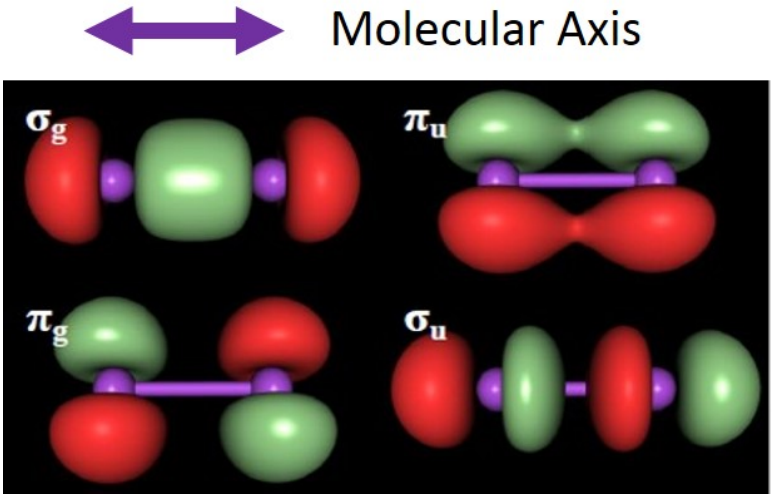

Figure 4.2.1: The four valence orbitals of I_2 showing the spatial structure of the electronic distribution. The red and green colors indicate opposite sign.

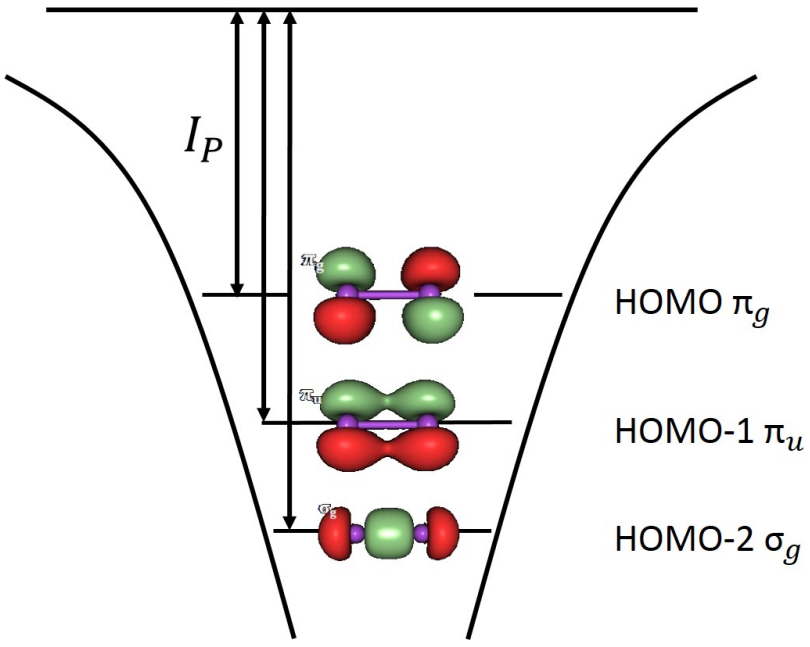

Figure 4.2.2: Ionization of inner orbitals of I_2 results in removing electrons from the HOMO, HOMO-1, and HOMO-2 which are identified as the X, A, and B states of I_2^+, respectively.

mentum distribution of ions onto a 2-D detection surface. Producing a dissociation event with the strong laser pulse results in ions with different momentum components. The VMI plates then act as an ion lens such that particles with the same initial velocity vector at the laser focus are mapped to the same point on the detector [88]. The strong field pulse will dissociate the molecules along the molecular axis producing a series of concentric spheres of ionization. The size of the sphere is directly related to the kinetic energy release of the ionization step and can be mapped onto the VMI detector. Since all of the ions created at or near the focus of the laser will be captured by the detector, the full distribution of velocities is also observed. The VMI data contains information about all dissociation events at all orientation angles and results in a measurement of the spatial (angular) structure of the dissociating molecules.

An image taken with a single pulse has information about the dissociation of the molecule including the momentum and angular distributions. However, we are interested in studying dynamics as a function of internuclear separation, as the molecule dissociates. Lighter molecules such as N_2 and HCl dissociate quickly and the dynamics of the ionization all occur during the laser pulse. By studying the heavier and relatively slow dissociating molecule I_2, we can separate the ionization and dissociation events in time and may then incorporate a pump-probe technique to study the exact ionization mechanism. The ionizing pump pulse removes electrons from inner orbitals, resulting in excited states of the ion. The probe pulse then detects the states which the molecule is left in while providing information about the orientation. Images are taken at intervals of time which are much shorter than the vibration or dissociation times of the ions. We are then able to study vibrational motion with a Fourier transform from time to frequency to identify the non-dissociating states produced through ionization.

This work studies the first ionization step of $I_2 \rightarrow I_2^+$. This first step is critical in

understanding the subsequent ionization which may follow to higher charge states as well as understanding the orbital structure of removing one electron from the neutral, again, as this is the method for producing HHG. Therefore, the probe pulse used is weak in intensity compared to the pump pulse so that dissociation is incited through mechanisms other than ionization, such as bond softening (BS) [98]. BS, for example, does not involve the removal of any electrons. Instead, dissociation occurs through avoided crossings created by single or multiphoton resonances resulting in molecular fragments emerging with kinetic energies typically less than one photon [99]. The dissociating fragments of $I_2^+ \rightarrow I^+ + I$ (defined as the (1,0) channel) are then a direct measurement of the products produced by ionization. This BS mechanism has been observed for inner orbital ionization of HCl [92] and we propose a similar mechanism for the inner orbital ionization of I_2 as shown in Fig. 4.2.3.

Previous work in I_2 [38] studied inner orbital ionization by producing a wave packet in the A(3/2) state of I_2^+ and probing the motion by ionizing to the dissociating (2,0) state of I_2^{2+}. The pump and probe pulses may be polarized parallel or perpendicular to the detector axis such that four different polarization configurations of pump/probe are possible: parallel/parallel, parallel/perpendicular, perpendicular/perpendicular, and perpendicular/parallel. Although this work used a wavelength of 400 nm for the pump-probe measurements, the conclusion was that ionization into the A(3/2) state is stronger when the laser polarization is perpendicular to the molecular axis, defined as a perpendicular transition. The current work also supports these findings. However, the probe mechanism in [38] was ionization and the probe in the current work produces dissociation through bond softening (no ionization) discussed below and first seen in [98]. Even with polarizations of the pump and probe pulses parallel to each other, the bond softening probe in the current work shows modulation in the I^+ signal at the A(3/2) frequency. The ionizing probe of the previous work does not show any modulation. It appears that the A(3/2) state of I_2^+ may be a path-

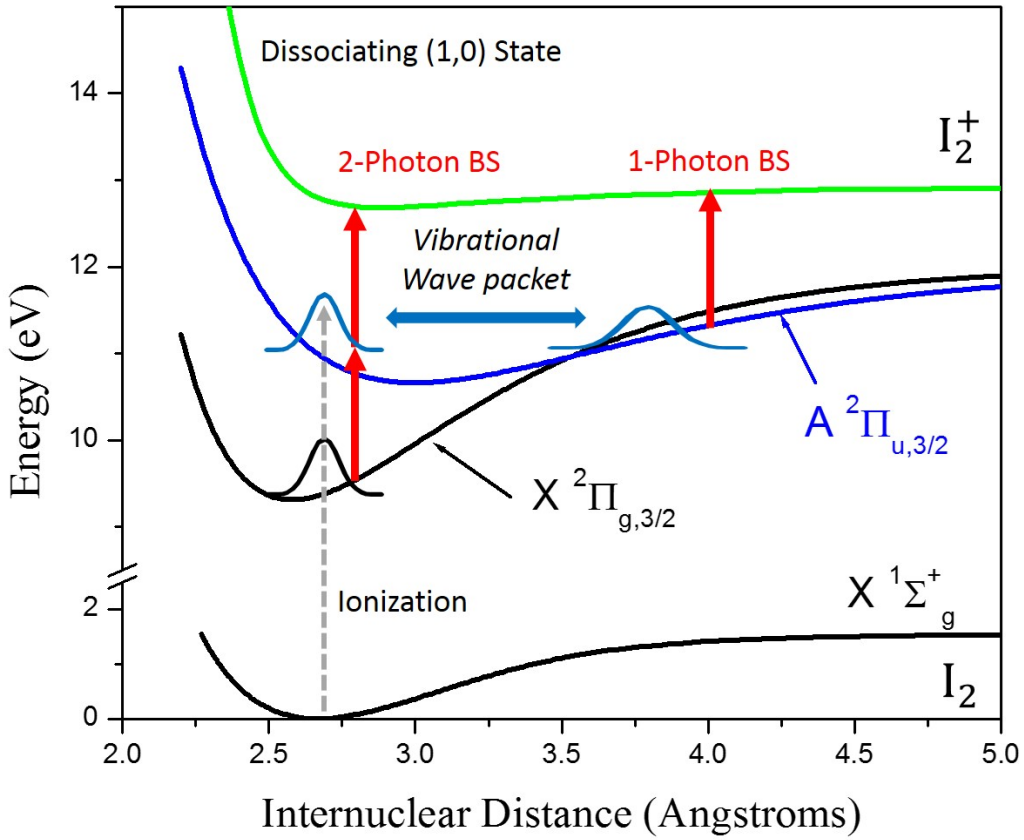

Figure 4.2.3: Ionization produces vibrational wave packets in bound states of I_2^+. These states can be detected through a dissociating state via bond softening (BS) with a probe pulse. The X state of the ion can BS with a two-photon transition and the A state through a one-photon transition.

Table 4.2.1: Vertical Ionization energies, equilibrium positions, and vibrational frequencies for I_2^+ from [100]. The notation *klmn* is used for the electronic configurations of the valence orbitals $\sigma_g^k \pi_u^l \pi_g^m \sigma_u^n$.

Property Electron Configuration	X $^2\Pi_g(3/2)$ 2430	X $^2\Pi_g(1/2)$ 2430	A $^2\Pi_u(3/2)$ 2340	A $^2\Pi_u(1/2)$ 2340	B $^2\Sigma_g^+$ 1440
I_P (eV)	9.34	9.98	10.96	11.81	12.95
ω_e (cm^{-1})	220 ($\pm$ 8)	214 ($\pm$ 8)	138 ($\pm$ 2)	112	72
Period (fs)	152 ($\pm$ 6)	156 ($\pm$ 6)	242 ($\pm$ 4)	298	463
This Work (fs)	143 ($\pm$ 10)		270 ($\pm$ 10)		
R_e ($\AA$)	2.58	2.58	2.99	2.98	3.62

way to the (2,0) state of I_2^{2+}, but only in certain geometries. The physics of the probe step of these experiments may lead to further understanding of the ionic states produced and may be a sensitive tool for indentifying states through either bond softening or ionization.

4.3 FFT Spectroscopy and Vibrational Structure

Ionization of I_2 can lead to bound states of I_2^+. Some possible states produced through ionization are given in Table 4.2.1 and the potential curves are shown in Fig. 4.3.1. These states have different vibtaional periods, ionization potentials, and equilibrium positions about which the vibration occurs. The vertical ionization into the ionic states assumes that the ionization occurs much faster than any nuclear motion such that the internuclear separation does not change during the ionization step. This is an accurate assumption for heavier molecules like I_2. Since the equilibrium positions of these states are different than for the neutral ground state R_e (2.66 $\AA$) the wave packets produced in these states will vibrate at a characteristic frequency. The ionization of multiple inner orbitals means that several frequencies of vibration may be observed in an ion signal. In order to understand which states are produced through ionization, a second probe pulse is needed to interrogate the vibration at different times throughout the period. By using this pump-probe spectroscopy, we are able to identify which orbitals are ionized by performing a fast Fourier transform (FFT) of the modulated ion signal as a function of probe time delay which results in a frequency spectrum. The peaks in the FFT spectrum provide the frequency of the signal modulation as well as information about population in each state and are used to determine which states are produced through ionization.

Inner orbital ionization can result in different electronic configurations. For example,

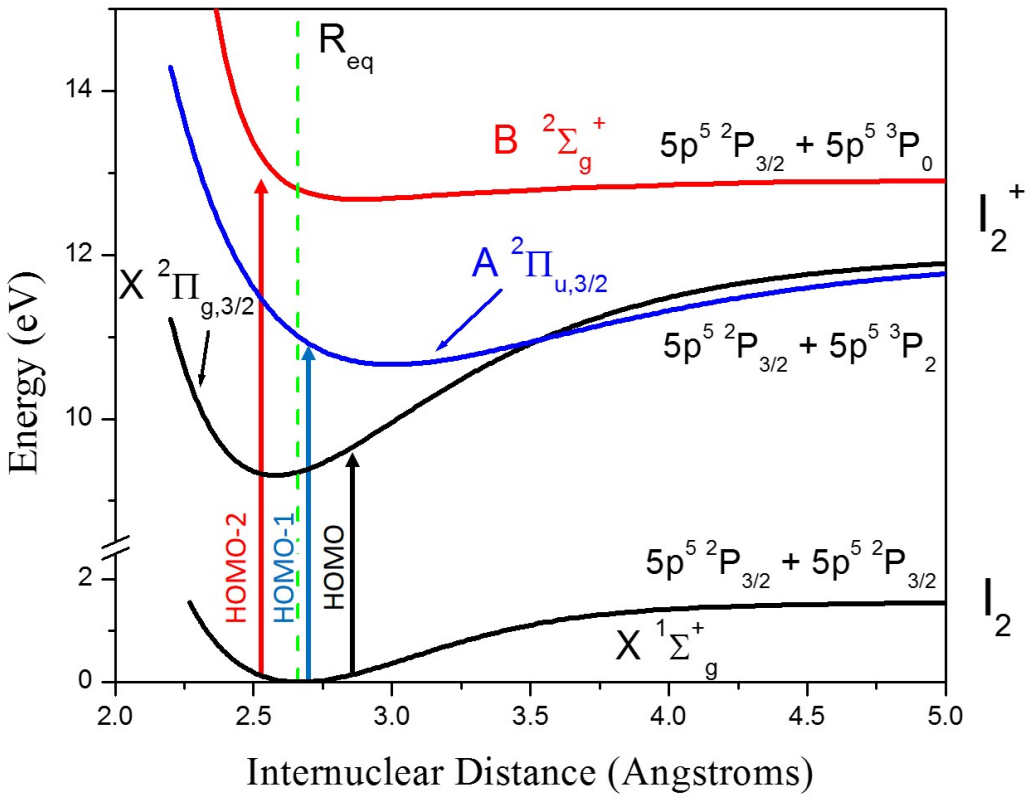

Figure 4.3.1: Relevant potential curves for I_2 and I_2^+. The relativistic dissociation limits are shown on the right hand side of the figure. Ionization of inner orbitals of I_2 results in removing electrons from the HOMO, HOMO-1, and HOMO-2 which are identified as the X, A, and B states of I_2^+, respectively.

this chapter.

4.4 Velocity Map Imaging

4.4.1 Imaging Assembly and Ion Detection

The experiments are performed in a high vacuum chamber with iodine gas effusively leaked into the chamber. The base pressure of the chamber is typically 10^{-9} torr and is maintained by a turbo pump. The pressure of the iodine in the chamber is set between $\sim$5x10^{-8} to $\sim$5x10^{-7} torr depending on the ion fragments being imaged and the pulse energy. Higher charge states will have a weaker signal upon detection so the pressure may be increased without saturation of the detector. Increasing the pressure does not change the physics and results in better statistics at lower pulse energy and higher charge states. Pressures should be kept below 10^{-6} torr to avoid saturation or damaging the MCP. The laser repetition rate is 1 kHz set by the oscillator and the pulse duration is typically 50 fs. The ionizing laser is focused by a 3 inch spherical mirror inside the chamber to a spot size of less than $\sim$10 μm to produce the high intensity focal volume needed for ionization. In the following experiments, intensities of 10^{13} to 10^{14} Wcm^{-2} are typically used.

The ions produced by the laser are extracted by the electrostatic grid assembly as shown in Fig. 4.4.2. There are 3 stainless steel plates used for the ion optics grid system, each one 100 mm in diameter and 0.76 mm in thickness. The extractor and ground plates are separated by 14.6 mm and each have a hole in the center with a diameter of 19.05 mm to allow the ions to pass through to the detector. The distance from the laser focus where the ions are produced to the detector is 240 mm. This is the distance associated with the time of flight. The ions pass through a time of flight region and are detected by an imaging detector

consisting of a chevron multi-channel plate (MCP) and a 40 mm diameter phosphor screen (Beam Imaging Solutions BOS-40). The front and back of the MCP can have voltages applied up to 1000 V each and the phosphor up to 5000 V. The potential difference between the back of the MCP and the phosphor accelerates the electrons onto the phosphor screen which fluoresces to produce the VMI data. The signal strength can by increased slightly by increasing the phosphor voltage. Optimum voltages for the MCP and phosphor are approximately 1900 V and 4500 V, respectively. There is a current limiting 8.2 MΩ resistor in series with the high voltage power supply for the phosphor to prevent current reaching the power source. This allows for higher applied phosphor voltages without tripping the power supply and damaging the coating of the phosphor.

For laser polarizations parallel to the detector surface (perpendicular to the flight axis) defined here forward as ”vertical” polarization, the dissociating fragments will reach the detector at the same time for a given charge state. In order to image a particular ion fragment or charge state, the MCP must be turned on at the flight time associated with the ions of interest. This is determined by the time of flight of the system. A TOF spectra may also be obtained by recording the total emission from the phosphor with a photo-multiplier and an oscilloscope, although we have not implemented this design yet. Here, the phosphor screen may be used as an anode and the electron current from the MCP to the phosphor can be recorded with an oscilloscope to provide a TOF spectrum. A higher mass-to-charge ratio will have a shorter flight time than a lower ratio. For example, the time of flight for I^+ ions is 6910 ns and for I^{2+} is 4780 ns. By applying a timed voltage pulse using a high-voltage switch (DEI PVX-4140 Pulse Generator), the gain of the MCP can be gated to select ions of a particular mass (Fig. 4.4.1). The gate is typically open for 400 to 700 ns which is long enough to ensure all fragments of a specific mass will be collected in the gate window. The gate window may be shortened to 150 to 200 ns, but below that will start to be too short for

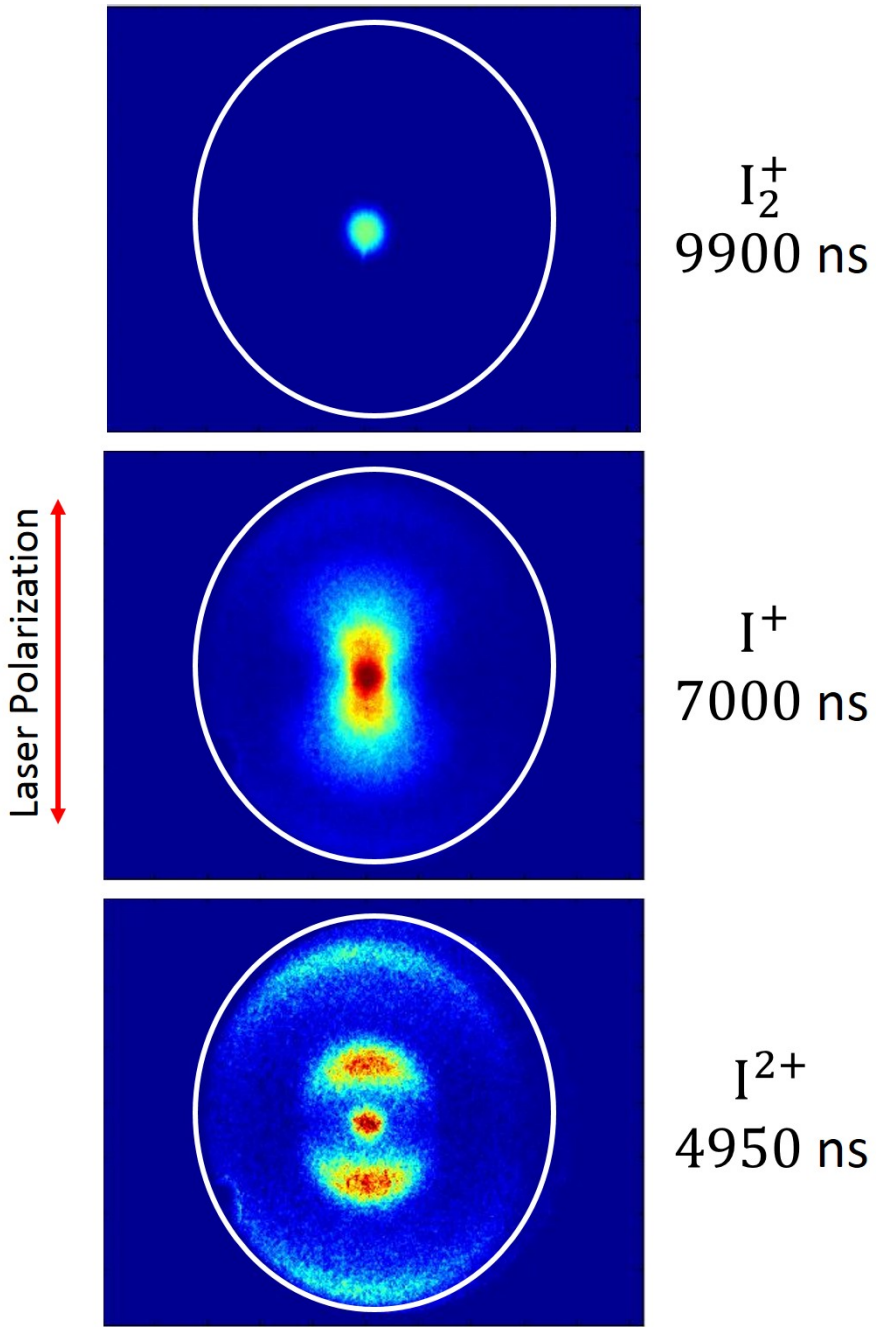

Figure 4.4.1: Example of VMI images produced for several ions by gating the MCP at different times.

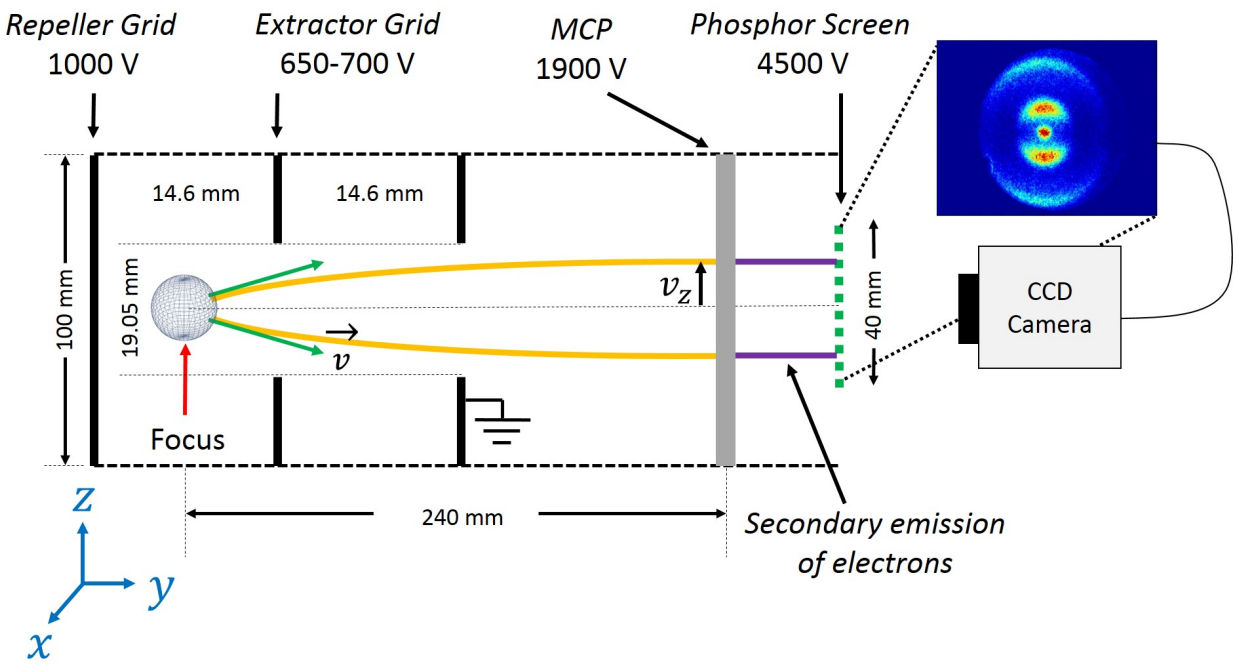

Figure 4.4.2: Schematic of the VMI setup and detection method with relevant dimensions and voltages (not to scale).

complete ion detection as some dissociation channels have shorter separations in time.

The spatial 2D images on the phosphor screen produced by fluorescence are then recorded with a USB CCD camera (Pixelink PL-B953U) with a resolution of 1024x768 pixels. An objective lens is used to image the phosphor with f=16 mm. The data are collected at a rate of 20 Hz and a 50 ms exposure set by the CCD camera. Since a typical image records thousands of laser shots over the period of about 1 minute, the data must have a threshold applied. With a threshold set, pixels with values falling below the set value will be counted as 0, and above the threshold will be 1, resulting in a binary image selection equivalent to "chopping" the image signal at the threshold. The threshold is set by measuring the pulse height distribution and is set to 30 (out of 256 for the CCD camera) for data acquisition.

4.4.2 Optimization and Calibration

The repeller and extractor voltages must be carefully set to image ion velocities. These voltages set the flight time of the ions as well as the magnification of the image and the proper ratio for ion imaging must be determined. Both voltages are positive for imaging ions, thus creating an electric field between the plates and forcing the ions toward the detector. The ion optics should be set to a) produce an expanding ion cloud along the TOF axis b) produce an image that is linearly proportional to the expansion velocity for any dissociation energy and c) map ions produced with different angles and velocities to different points on the detector. It is also important that ions with the same velocities and angles, but produced at different positions in the laser focus, map to the same detector position. These criteria will result in the proper ion velocity imaging mode of the assembly where the sensitivity to velocity is optimized and the blurring of the ionization due to the focal volume is minimized. The velocity imaging mode then maps all ions with the same

initial velocity component parallel to the detector to the same point on the detector as shown in Fig. 4.4.3. There is an angular dependence for the velocity distribution which, due to the cylindrical symmetry, can be removed with an inverse Abel transformation to study the kinetic energy of the detected ions.

A good starting point for the repeller voltage (V_R) is 1000 V and for the extractor voltage (V_E) 500 V, or a ratio of extractor to repeller of 0.5. At this ratio, the ion lens is out of focus such that the focal plane is not at the detector and a blurring will occur since ions with equal velocities will be detected at different positions. This can be checked by adjusting the focusing mirror in the chamber while observing a non-dissociating ion (such as I_2^+) which produces a well defined spot-like signal at zero KER on the detector. If there is any sensitivity of the ion position on the detector to the position of the laser focus, then the voltage ratio is not correct for ion imaging. By increasing V_E and continuing to monitor the ion position, an optimal voltage can be found so that there is no sensitivity to the position of the laser focus. For the current VMI ion optics, a ratio of 0.7 is close to optimal. Once the grid voltages are set for optimum focusing, the overall size of the image on the detector can be set to the desired size by adjusting V_R and keeping the ratio the same. As long as the laser position and ratio are kept the same, the ion imaging will remain focused as the focusing parameters are independent of the mass-to-charge ratio. Images can be magnified for increased kinetic energy resolution by simply decreasing the repeller voltage while, again, maintaining the optimized focusing voltage ratio.

The voltage ratio for ion imaging can be confirmed with ion simulations with the parameters of the VMI and plate voltages and is shown in Fig. 4.4.4. In the simulations, ions produced at different positions will all reach the same point on the detector and ions of different velocities (energy) will be at points linearly proportional to their velocities. The optimal voltage ratio from the ion simulations is 0.675 +/- 0.05. This agrees well with the

ratio of 0.7 obtained experimentally. By using the simulated ion data, a calibration for the energy as a function of detection position in mm from the detector center can be developed. This will allow for converting the number of pixels on the camera to energy (eV) so that images may be presented in terms of the more relevant dissociation energy rather than pixel number. Ions with different energies (or velocities) will be detected at different positions or pixel numbers. The simulation can provide a range of energy values which correspond to trajectories arriving at different detector positions and a calibration can be obtained. Since the energy goes as the square of the momentum, the simulation data can be fit with a quadratic. Since a camera is used with a specific resolution, the number of pixels/mm must first be determined. The camera array is 1024x768 pixels and in the current experimental setup, the vertical direction (or perpendicular to the flight axis) contains 768 pixels while the horizontal contains 1024. The detector size is 40 mm in diameter giving a theoretical calibration of 768 pixels/40 mm = 19.2 pixels/mm. However, the detector does not fill the entire vertical range of the CCD (768 pixels). An example image taken with the camera shows it fills only 716 pixels/40 mm yielding a calibration of 17.9 pixels/mm. The results of the energy calibration using m=127 amu and q=1 (for I^+) and a grid ratio of 0.675 are given in Fig. 4.4.5. The simulation was also performed for m=127 and q=2 (for I^{2+}) and the results of the fitting are given in Eq. 4.4.1. The calibration can be generalized to any ion with charge q as shown in Eq. 4.4.1 as well.

$$
\begin{aligned}
I^+ &: E(eV) = (5.1 \pm 0.3) x 10^{-5} n_{pixels}^2 \\
I^{2+} &: E(eV) = (8.6 \pm 0.7) x 10^{-5} n_{pixels}^2 \\
I^{q+} &: E(eV) = q(5.1 \pm 0.3) x 10^{-5} n_{pixels}^2
\end{aligned}
\tag{4.4.1}
$$

The time of flight can be calibrated by identifying several ion fragments and their as-

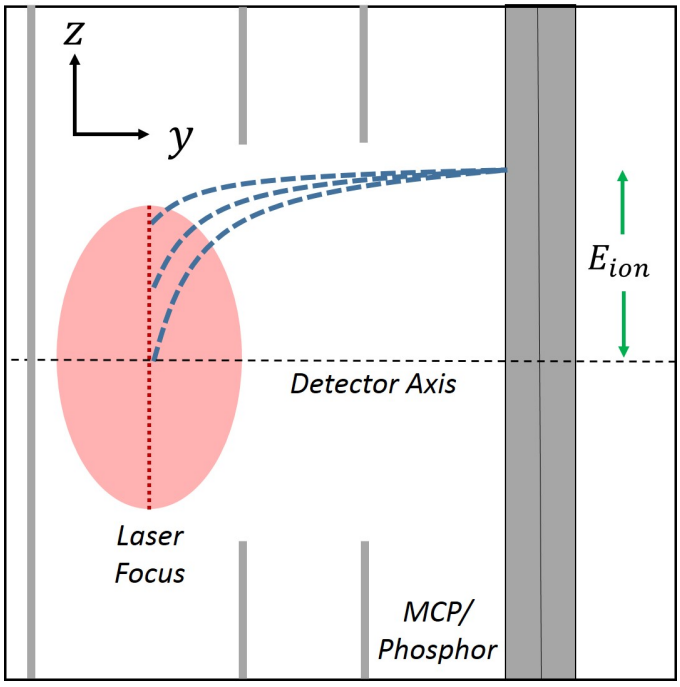

Figure 4.4.3: Velocity mapping principle. Ions produced at different positions in the laser focus with the same initial velocity component parallel to the detector v_z are mapped to the same position from the center of the detector. The kinetic energy release, E_{ion}, may then be determined from the velocities.

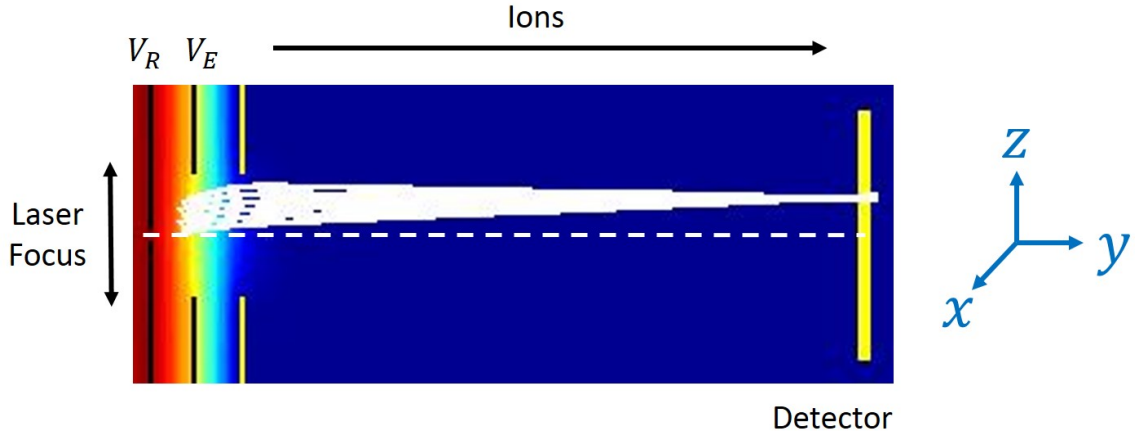

Figure 4.4.4: Simulation of ion trajectories for the VMI. Ions of the same initial velocity, but produced at different points in the laser focus, are mapped to the same point on the detector for the proper ratio of V_E/V_R. The ratio for the simulations is 0.675.

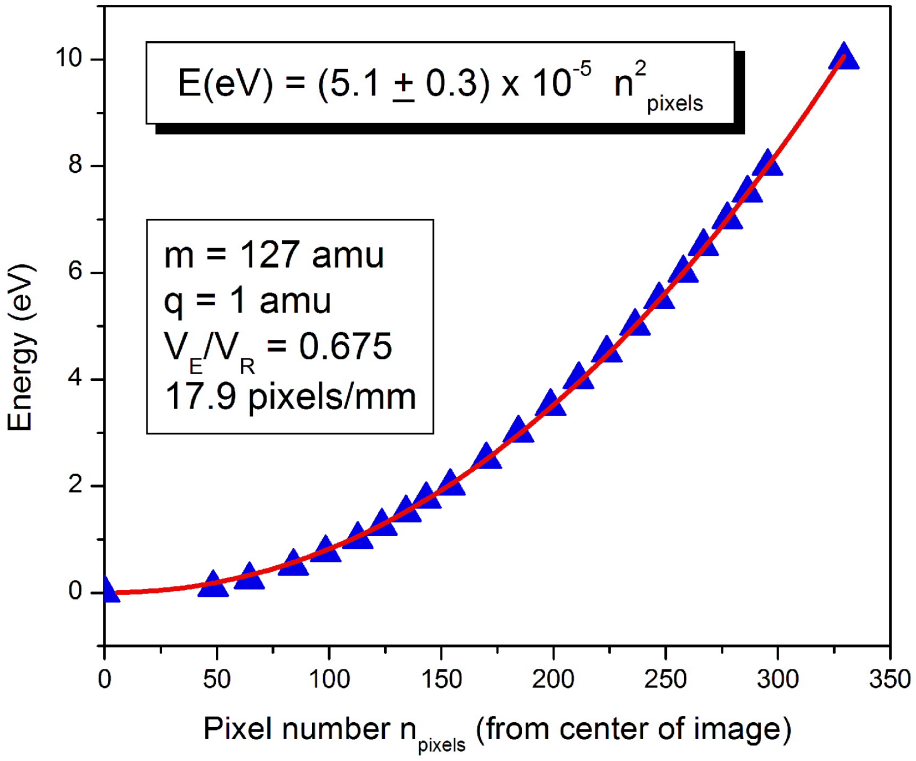

Figure 4.4.5: Energy (eV) vs. pixel number calibration based on ion trajectory simulations. The ratio for the simulations is 0.675.

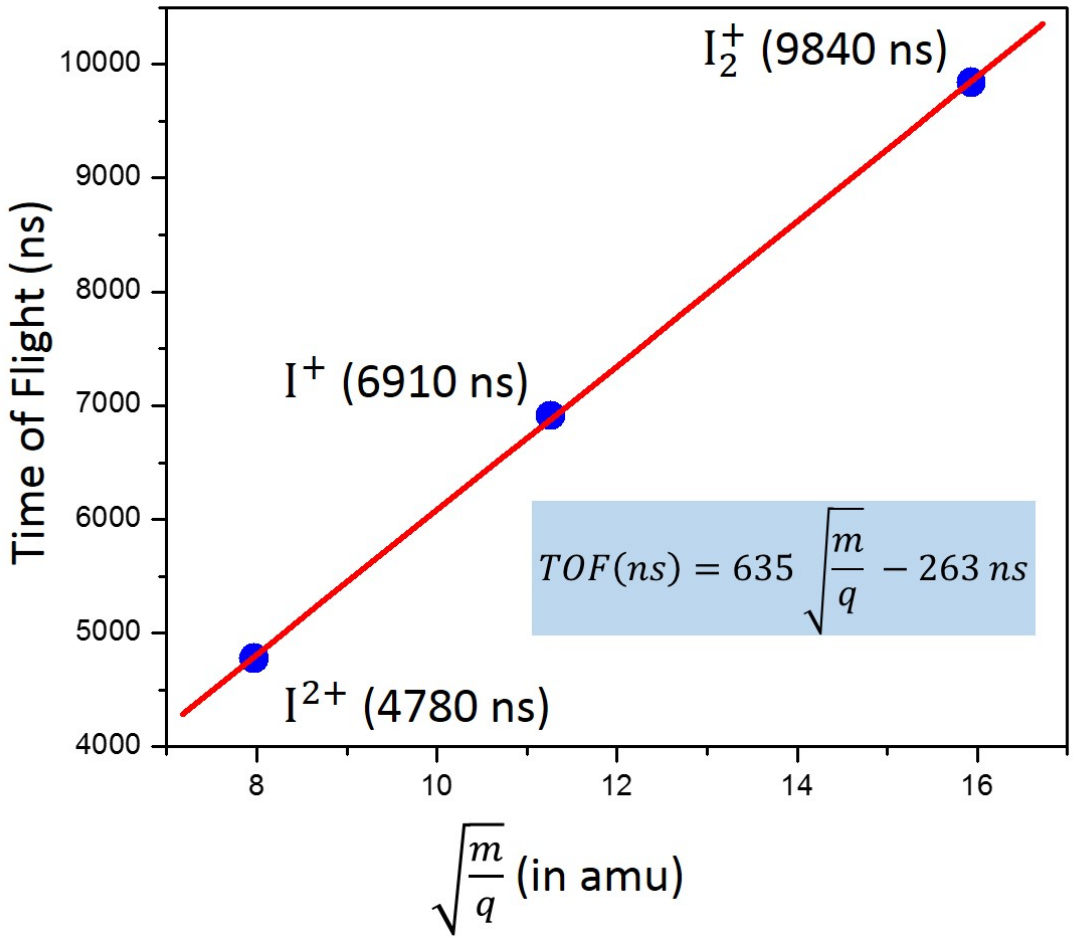

Figure 4.4.6: Calibration for the time of flight used in VMI. Points are shown for 3 ions and their flight times are plotted as a function of the mass-to-charge ratio (in amu). The time of flight for any ion can be calculated from the equation inset in the graph by providing the mass and charge.

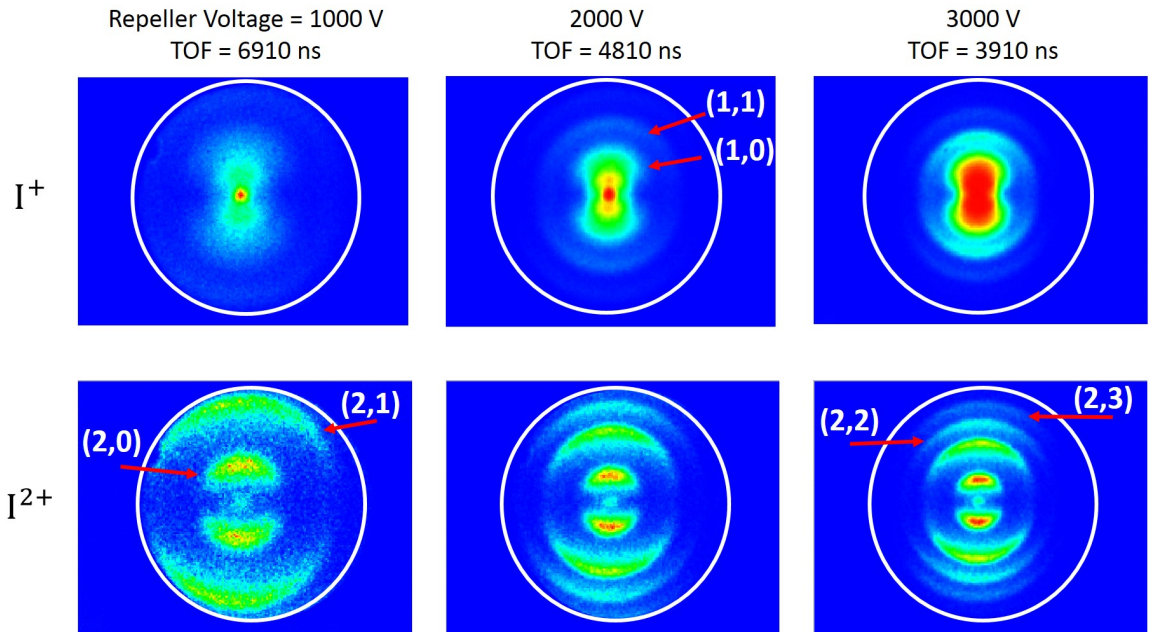

Figure 4.4.7: Ion images taken at 3 repeller voltages. Higher charge states are observed as the repeller voltage is increased. The data was recorded at a pressure of 2.5 x 10^{-7} torr with a single 10 μJ pulse at 800 nm. The laser polarization is parallel to the detector surface (perpendicular to the time of flight axis).

sociated flight times and performing a linear fit of the form of Eq. 1.5.1. This calibration is shown in Fig. 4.4.6 for a repeller voltage of 1000 V. The flight time of the ions t is $t \propto \sqrt{\frac{m}{qV_R}}$ such that a higher voltage decreases the flight time. A shorter flight time due to the higher voltage results in a smaller ion cloud at the detector and the ion fragments will be more tightly spread from the center of the detector. This is useful for imaging higher charge states as they will dissociate with a larger energy than lower charge states. Several images at different repeller voltages are shown in Fig. 4.4.7 with the corresponding flight times. As the repeller voltage is increased, the ion distribution becomes more closely spaced and higher charge states can be observed and the ion flight times become shorter. However, information in the low energy region of the detector is more difficult to resolve and some information may be obscured or less obvious. For imaging the I^+ and I^{2+} ions, a repeller voltage of 1000 V is sufficient and is used for the following data collection. Flight times for different V_R may be obtained by dividing the flight times at 1000 V by $\sqrt{V_R}$ in keV.

4.5 Experimental Results

4.5.1 Probe Energy Dependence in Bond Softening I_2^+

The experiments are performed with pump/probe pulse energies with a typical ratio of 2/1. A higher intensity pump pulse ensures that the pump pulse is ionizing the neutral and producing I_2^+. The lower intensity probe is then acting to bond soften the bound states of I_2^+ without completely ionizing the system to a higher charge state. With bond softening (BS), as described first in [98], the moleuclar bond "softens" such that the internuclear potentials become gently repulsive and no electrons are removed in the process. This mechanism involved both multiphoton absorption and stimulated emission and results in slow

ion fragments. Since BS is a resonant process, the transition can be saturated by a probe of sufficiently high intensity. Further, BS may occur from different bound states and the number of photons required for the process may be different. In particular, we investigate the dependence of the FFT amplitude of the X(3/2) and A(3/2) states on the energy of the probe pulse which produces the BS. Since the amplitude of the FFT is related to the population in these states, any dependence on the probe energy provides information about the efficiency of the bond softening. The ionization rate in this regime scales with the number of photons, n, as I^n where I is the probe pulse intensity. By plotting the FFT amplitude as a function of the probe energy and fitting the data with this ionization model, the order of the bond softening process may be determined. For example, a slope of I^1 is a one-photon process, I^2 is a two-photon process, etc.

The probe energy dependence to determine the number of photons involved in shown in Fig. 4.5.1. The pump pulse is fixed at 18 μJ and the probe is varied from 1 to 18 μJ in 1 μJ increments. The polarizations of both pulses are vertical. For each pump/probe energy, a probe delay scan is recorded over 1.5 ps in 25 fs steps. Data is collected at 300 camera frames per step at a pressure of 2.4 x 10^{-7} torr. The I^+ signal is integrated at each time step producing a signal vs. probe delay plot which is then Fourier transformed to the frequency domain. The amplitudes of the X and A states are recorded for each pump/probe data set and plotted on a log-log scale as a function of probe energy. Linear fits to the data show two different slopes. This is confirmation that indeed we are populating two different states of the ion since they have different dissociation mechanisms. The energy dependence of the probe also shows that both the X and A states are produced over a wide range of energies. For lower probe energy, the A state is the dominant signal in I^+ while at higher probe energy, the X state is the stronger signal. At a pump/probe ratio of 2/1 the amplitudes of the X and A FFT signals are approximately equal. Thus, by changing

the probe energy one could optimize the signal of interest (the X or A state) to study the structures independently.

The slope of the linear fit to the A state FFT peak amplitude data is 0.40 andn that for the X state is 1.30. Further, the slopes differ by nearly one (1.30 - 0.40 = 0.90). Since the slope is related to the number of photons involved in the bond softening process, we conclude that the X state BS is one photon higher in order than the A state BS. By examining the potential curves of Fig. 4.2.3, a one-photon BS is most likely for the A state since the one-photon resonance with the dissociating (1,0) state is near the outer turning point. The probe pulse energy is likely saturating the one-photon transition for the A state, decreasing the slope, although this cannot be seen in the current data. Saturation may also be occuring for the two-photon transition of the X state. To inspect this furhter, a complete intensity dependence from much lower probe pulse energies (0.1 μJ or less) needs to be completed.

4.5.2 Pump-Probe Measurements and Fourier Spectroscopy

The ionization of the neutral results in different final states of the I_2^+ ion. In order to determine which states are produced a pump-probe measurement is used. As the method for dissociation of the bound X(3/2) and A(3/2) states of the ion appears to be bond softening, the probe pulse must be weaker than the pump pulse so that ionization is mostly avoided. To study both the X and A states, a 2/1 pulse energy is used. Previous work in I_2 used the opposite energy ratio of 1/2 to study Lochfrass, or *R*-dependent ionization, in the neutral I_2 [39]. Here, the weak pump pulse still ionizes the neutral, but the strong probe pulse can further ionize the coherent hole in the neutral produced by ionization. To avoid Lochfrass and to study bond softening, a strong pump/weak probe measurement is invoked.

Data are collected at a 2/1 pump/probe energy for probe time delays of about 1.5 ps in

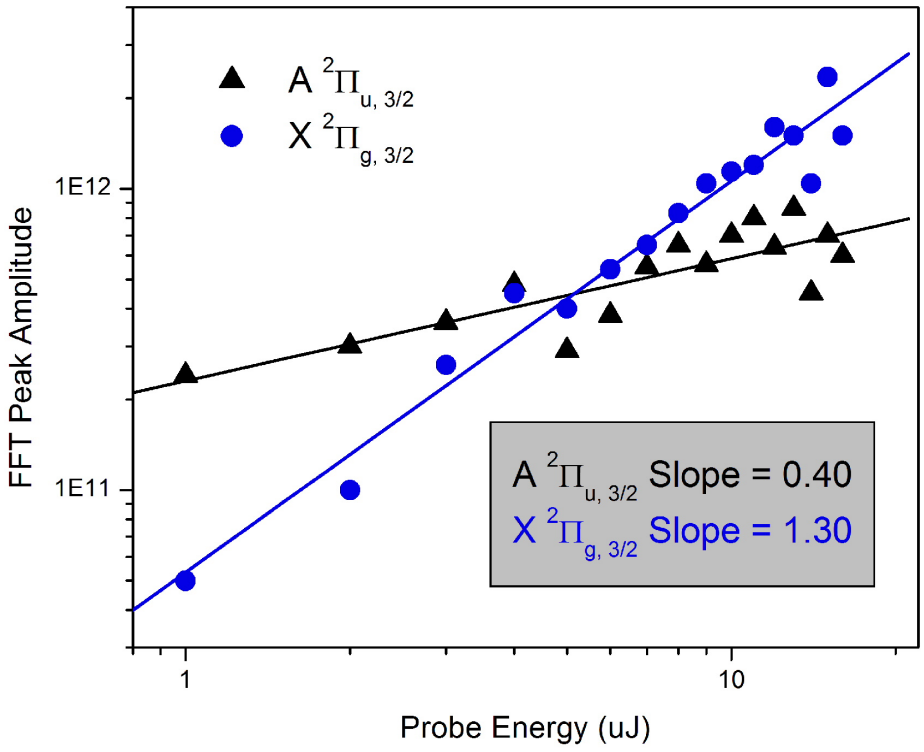

Figure 4.5.1: Peak FFT amplitude dependence on probe pulse energy for the X and A states of I_2^+. The slopes differ by approximately one. The A state shows a saturated one-photon transition and the X state shows an A state + one-photon transition, or two-photon transition.

25 fs/step. As shown in Fig. 4.5.2, the pump pulse ionizes the molecule to bound states of I_2^+ at R_e. This starts wave packets vibrating in the X and A states at the outer and inner turning points, respectively. The A state will then reach the outer turning point (large R) in the potential well at about 140 fs after ionization. The I^+ signal shows peaks with a periodicity of about 270 fs, consistent with the A(3/2) period. The X(3/2) period is nearly half the A(3/2) period, or about 145 fs. The vibrational wave packet in the X state starts at the outer turning point upon ionization. It reaches the inner turning point after about 70 fs and returns to the outer turning point 70 fs later, at $\approx$140 fs. The ion signal then shows two different frequencies although the factor of $\approx$2 between the X and A state periods results in both being at the outer turning point of the wells at the same probe delay so the independent signals cannot clearly be seen. However, the ion signal shows peaks in between the A state modulation of 270 fs which occur at 270, 540, 820 fs, etc. This is the dissociation of the X state at the outer turning point of the well where the two-photon BS is occuring.

The overlapping dissociation of the X and A states in the time-based pump-probe signal makes it difficult to accurately measure the periods of vibration directly. However, a Fourier transform can clearly resolve the two distinct vibrations in the frequency domain. The resolution of the FFT spectrum is equal to the inverse of the total time measurement. To get high resolution FFT spectra, a long time scan must be recorded. For example, a pump-probe delay scan over 1.25 ps has an FFT resolution of 0.8 THz while a longer scan of 5 ps has a resolution of 0.2 THZ. To get a well-resolved measurement of the frequencies of the X and A states, a 5 ps time scan in increments of 25 fs/step is recorded and shown in Fig. 4.5.3. Two frequencies are now clearly resolved in the frequency domain at 3.7 THz (270 fs) and 7.0 THz (143 fs) which are in agreement with the assignment of the A(3/2) and X(3/2) states, respectively.

To further confirm that these states are indeed populated and responsible for the ob-

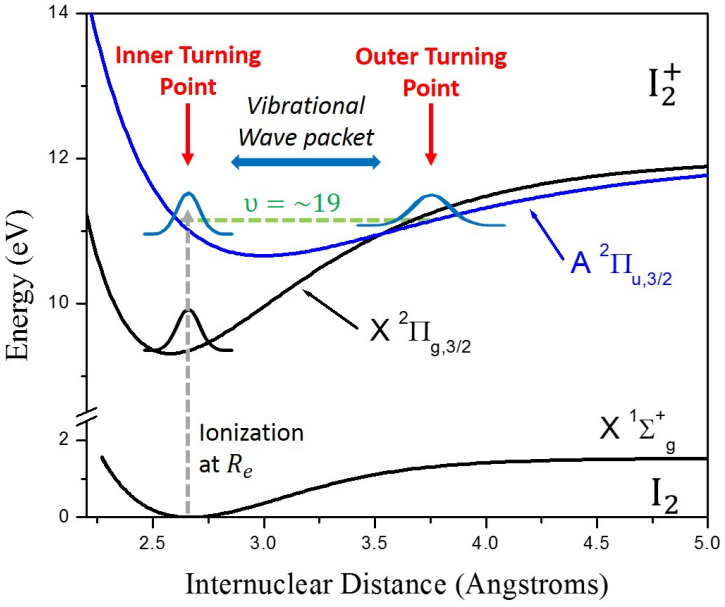

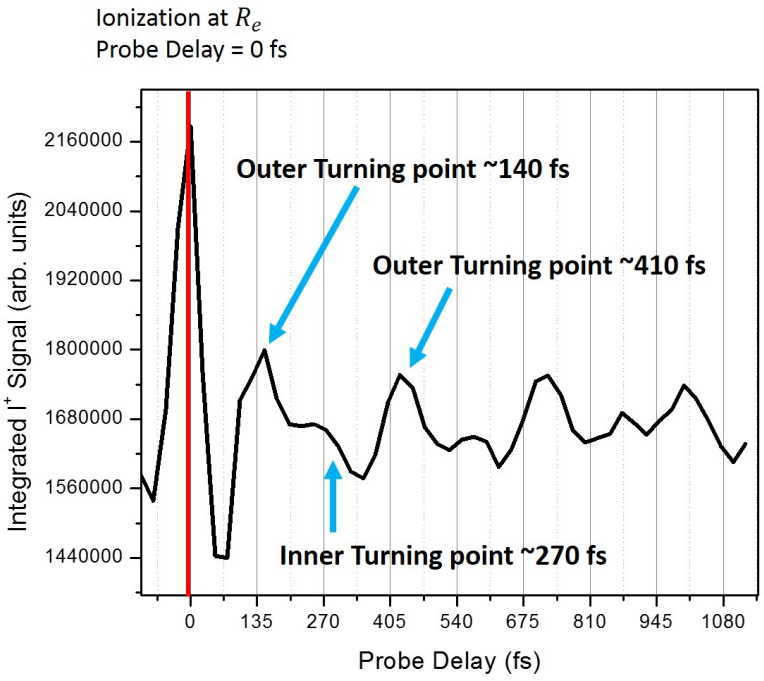

Figure 4.5.2: Tracking vibrational motion of the wave packet. The wave packet produced in the A state starts at the inner turning point near the vibrational energy level of v=19 and reaches the outer turning point a half-period later (top). The ionization is strongest at the outer turning point and shows structure with a period of 270 fs (bottom).

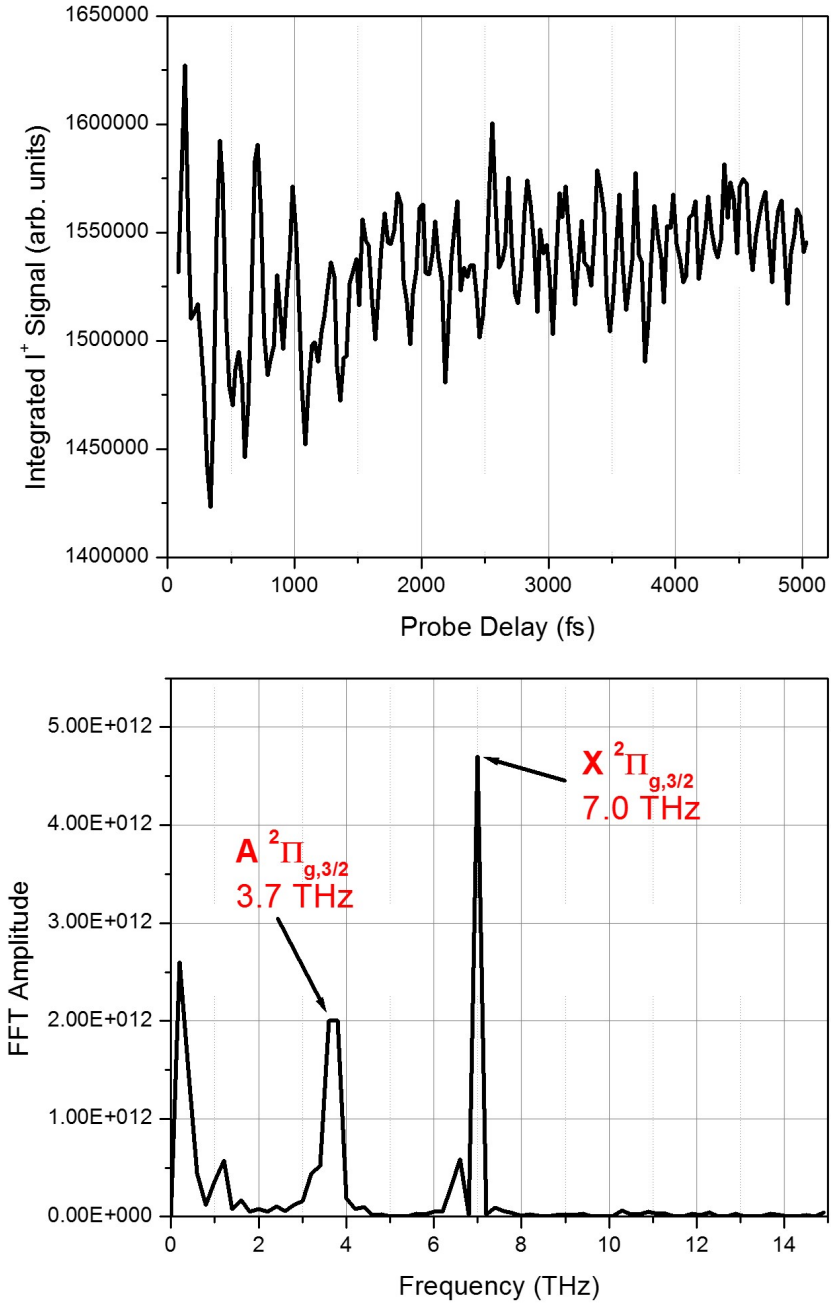

Figure 4.5.3: Pump-probe data for I^+. The pump pulse is horizontal and the probe is vertical. The probe is delayed over 5 ps in 25 fs steps. The pump/probe pulse energies are 18 μJ/9 μJ. The signal is summed to include all I^+ ions and 0 KER I_2^{2+} ions in the region of interest. Two peaks are prominant at 3.7 and 7 THz, which are identified as the A(3/2) and X(3/2) states, respectively.

served modulation in the ion, the FFT can be broken into two regions from 0 to 2.5 ps and 2.5 to 5 ps as shown in Fig. 4.5.4. In the first half of the pump-probe time domain data, the A state shows stronger modulation than the X state. However, the amplitude of the ion signal is decaying over the 2.5 ps. This decay has been studied in [38] and was measured to have a decay time constant of 0.78 ps. It is attributed to the dephasing of the vibrational wave packet in the anharmonic potential well of the A state. In a harmonic potential, the wave packet would vibrate indefinitely since the phases of the superposition of eigenstates which make up the wave packet would not dephase (or dephase very little) while oscillating in the well. These vibrations would persist for a long period of time when measured with a pump-probe experiment. Interestingly, we are able to observe such long-lived coherent vibration in the X state of the ion. Here, the wave packet is produced very close to the bottom of the X(3/2) potential well where the well itself is more harmonic than the A(3/2) state. By examing the longer time delay data from 2.5 to 5 ps, we find that the A state modulation has almost completely vanished due to dephasing as the FFT amplitude is 10x lower than in the short time delay data. The X state modulation remains and the FFT amplitude is nearly the same as in the shorter time delay. This again confirms that we are observing the X(3/2) and A(3/2) states in the I^+ signal.

To investigate the orbital structure of these states, the pump and probe pulses can be set for different configurations. The configurations are pump and probe parallel to each other (horizontal/horizontal polarization and vertical/vertical polarization) or perpendicular to each other (horizontal/vertical polarization and vertical/horizontal polarization). The FFT spectra produced by these four geometries are shown in Fig. 4.5.5. From the symmetry of the X and A state orbitals, we expect a preference for the ionization step. The X(3/2) state has a π_g symmetry (Fig. 4.2.1) such that there are two nodal planes in the orbital, one along the molecular axis and one perpendicular. Along the nodal planes, there is little to no elec-

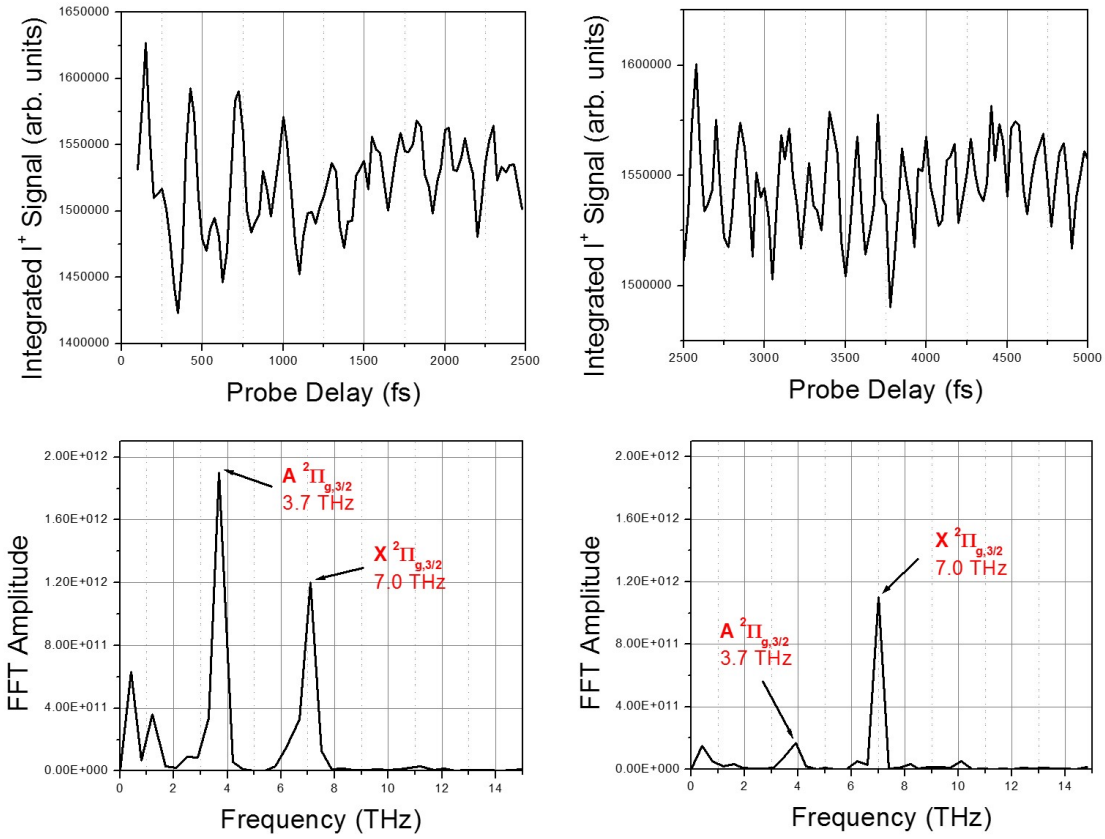

Figure 4.5.4: Pump-probe data for I^+. The pump pulse is horizontal and the probe is vertical. The pump/probe pulse energies are 18 μJ/9 μJ. For the left column, the probe delay is from 135 fs to 2.5 ps in 25 fs steps. The right column shows data for a probe delay of 2.5 ps to 5 ps. The signal is summed to include all I^+ ions and 0 KER I_2^{2+} ions in the region of interest. At shorter time delays, the A state is the dominant frequency (left column) while at longer delays, the X state is dominant (right column).

tronic distribution. The current understanding of orbital ionization predicts that the orbitial should ionize most strongly when aligned with the most spatially extended components of the orbital [95]. The X state would then ionize most strongly about 30-45 degrees from the molecular axis and have minimal ionization along the nodes. Ionization parallel or perpendicular to the molecular axis should yield the same rate and be reflected in the amplitude of the FFT spectrum. Indeed, for all four polarization measurements, the amplitude of the FFT is nearly constant for the X state. The ionization of the X state appears fairly isotropic as the data do not support a clear preference perpendicular or parallel to the molecular axis. The A(3/2) state has a π_u symmetry which has a nodal plane parallel to the molecular axis. There is electronic distribution perpendicular to the molecular axis and so the A state is expected to ionize more strongly when the ionization occurs perpendicular to the molecular axis. Ionization of this orbital should be dominant when the pump and molecular axis are perpendicular to each other. In the case of a vertical probe (Fig. 4.5.5) the FFT amplitude is about 3x larger in the perpendicular polarization geometry compared to parallel. This supports the picture of a stronger perpendicular ionization for the A state. However, when the probe is horizontal the results are not consistent with the vertical probe. Here, the parallel polarization configuration gives a stronger amplitude than the perpendicular. This is an ongoing question, but may be due to a different sensitivity of the detector when probing parallel to the detector axis compared to perpendicular. Further, the cylindrical symmetry of the VMI results in contributions from ions at different angles decreasing the resolution. Methods of Abel transformation and polar onion peeling [86] exist to remove these contributions and incorporating them may lead to a higher resolution of the observed structure.

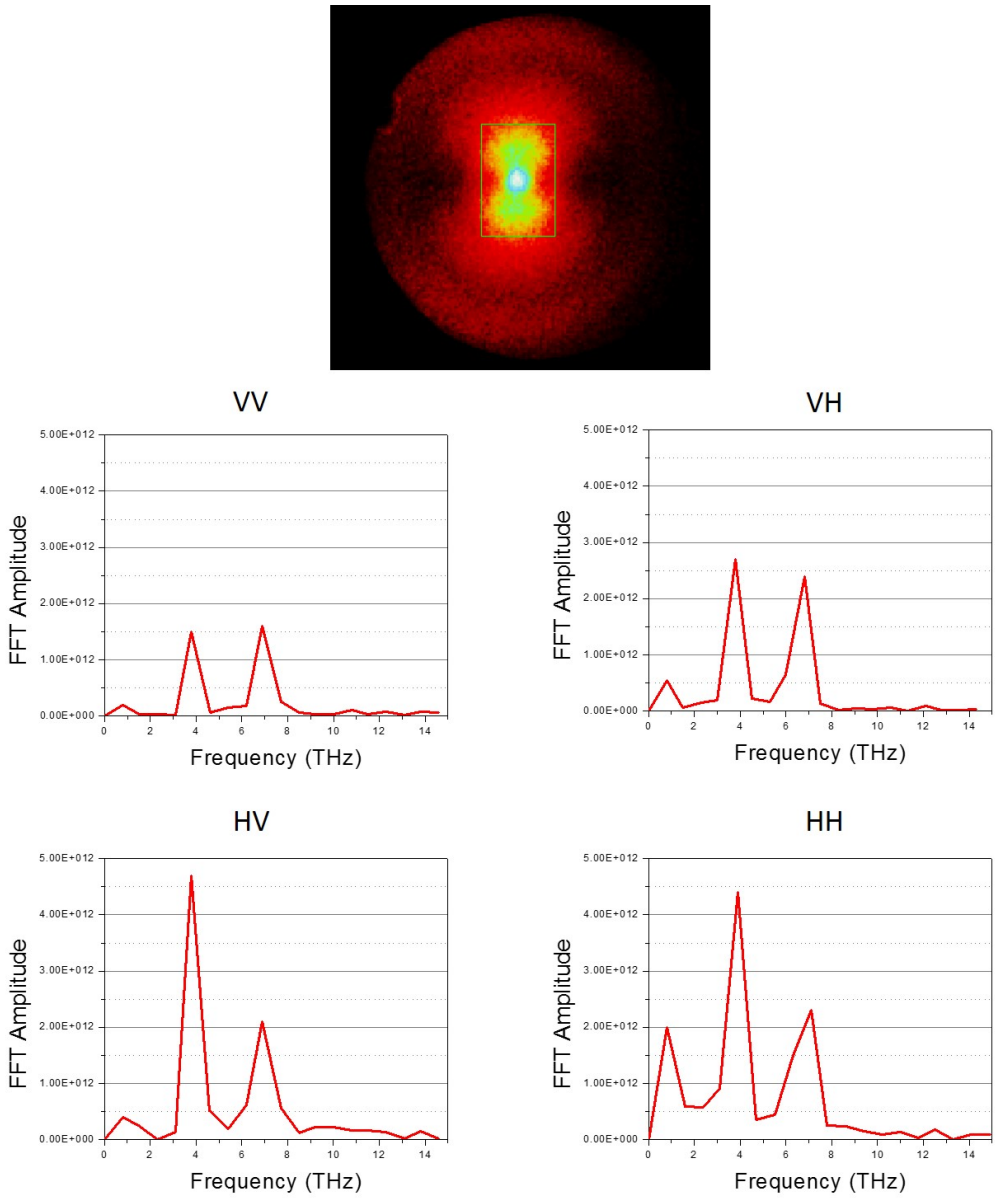

Figure 4.5.5: (Top) Example of the region used for integrating the ion signal for the FFT, shown by the small box near the center of the image. (Bottom) Pump-probe FFT data for I^+ for four pump/probe polarization configurations, V (vertical) and H (horizontal). The pump/probe pulse energies are 18 μJ/9 μJ. The data are all plotted on the same scale for comparison.

4.5.3 2D FFT Spectroscopy

By combining the VMI system with Fourier transform spectroscopy, we are able to obtain geometric information about the inner orbitals. The ionizing pulse will remove electrons from inner orbitals which have different symmetries and vibrational periods. By identifying the states based on the methods described above, we can take the FFT spectroscopy a step further to produce two-dimensional geometric images of structures with characteristic frequencies. This is done by performing a Fourier transform for each pixel in a VMI image at each time step resulting in a 2D FFT. The pixel i is first selected from each image taken in a pump-probe time delay measurement. This pixel is the same in each image, for example the first pixel in the CCD array of 768x1024. The intensity S associated with this pixel is recorded at each time delayed image and once all of the pixels are identified, an FFT can be performed. This procedure is repeated for every pixel in the array (Fig. 4.5.6). Any modulation will be recorded with the FFT array. Each FFT array is a one-dimensional array with the resolution set by the total pump-probe delay time and each value in the array is defined with a frequency. By choosing the frequency of interest, all pixels modulated at that frequency can be extracted and plotted as a two-dimensional image. These 2D images are then spatial pictures of any ions with the chosen frequency and represent the geometry of the ionizing molecular orbital.

An example of a typical set of 2D FFT images is given in Fig. 4.6.1 and Fig. 4.6.2. Since the X and A states modulate at different frequencies, they can be distinguished through the Fourier transform. Fig. 4.6.1 shows the result of the 2D FFT analysis for the four polarization configurations at the A(3/2) state frequency of 3.7 THz. A similar result for the X(3/2) state is given in Fig. 4.6.2. With a vertical probe pulse, the geometry is that of a ”dumbell” in which there are two caps one above and one below the center of the

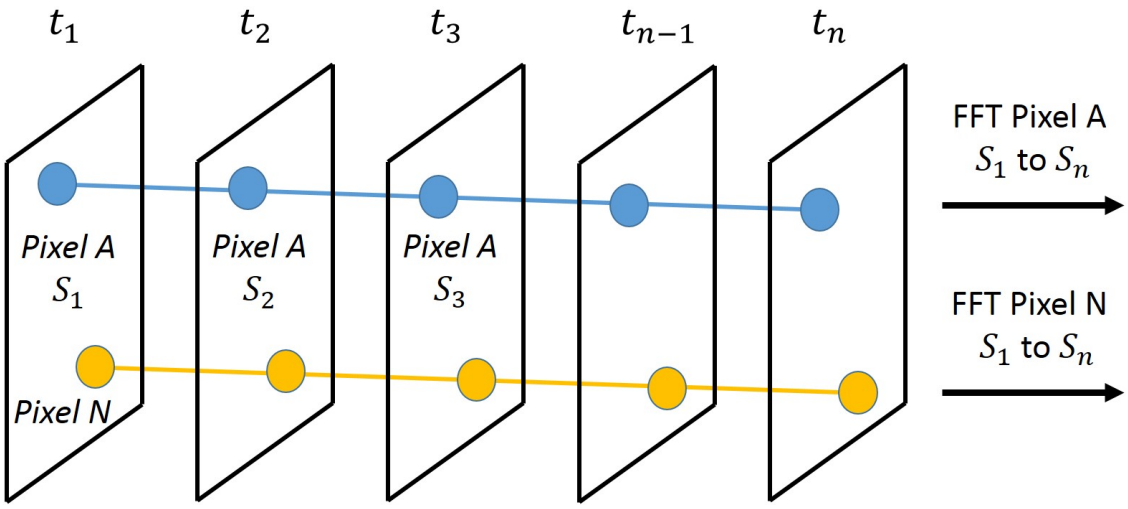

Figure 4.5.6: Schematic of the 2D FFT principle. The intensity of the signal S at pixel A is recorded from each VMI image at time t_1 to t_n and the data is then Fourier transformed. This is repeated for all the pixels in the image creating a two-dimensional FFT image.

image (0 KER). In this case, the probe stimulates dissociation perpendicular to the detector axis. When the probe pulse is rotated to horizontal polarization, the structure is a circular shape. Here, the probe dissociates the ions parallel to the detector axis.

VMI detectors can saturate near the center of the detector, or when the polarization is horizontal, resulting in a loss of sensitivity if the pressure or pulse energy are too high. This is observed for the horizontal/horizontal (HH) polarization configuration at higher pressure in Fig. 4.6.1 where there is a distinct dark region at the center of the image. By lowering the pressure, the detector is no longer saturated and the dark region fills in. The interpretation is then that the HH configuration produces ions which modulate at 3.7 THz even at 0 KER. This is at odds with early findings [38] in which no modulation at the A state frequency was observed for pump and probe pulses in a parallel configuration and may lead to a further understanding of the physics of the probe pulse. This technique shows distinctly different geometries of ion distributions depending on the pump-probe polarization. As this method appears to be sensitive to geometry, we can attempt to model both the ionization and probing step in the next section.

4.6 Discussion

4.6.1 Roles of the Pump and Probe Pulses

The geometry and orientation of the pump and probe pulses result in different spatial images in the 2D FFT discussed above. To model the ionization and probe steps, these geometries must be understood. The simulations that follow were performed on a 200x200 point grid by creating a three-dimensional cartesian coordinate system and defining the spherical coordinates through the standard transformation. The spherical coordinate ϕ is

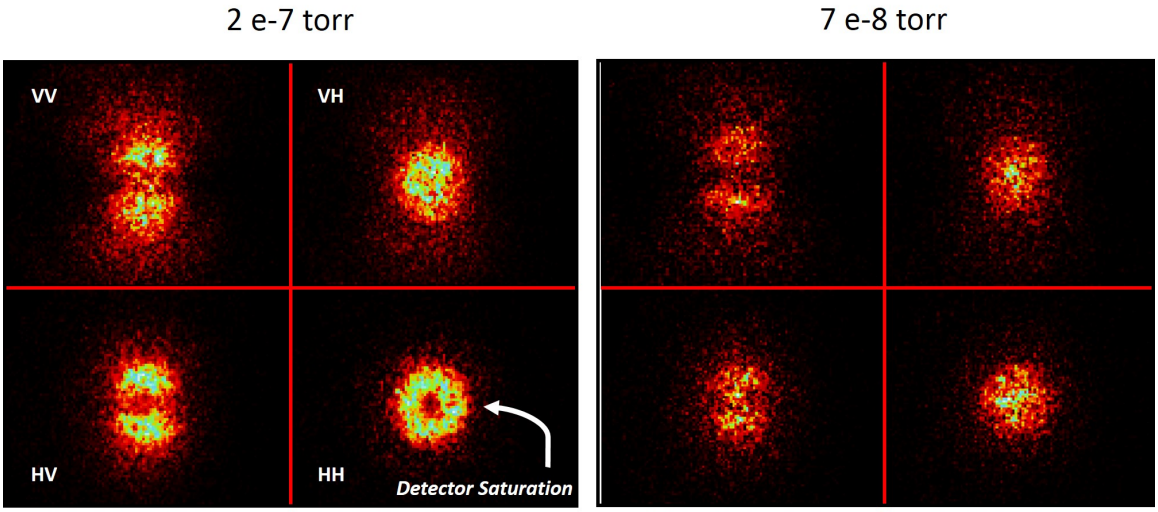

Figure 4.6.1: 2D FFT data for the A state of I_2^+ detected in the I^+ spectra at two different pressures. The higher pressure data on the left shows a dark spot in the center of the detector for polarization along the axis which is characteristic of saturation. By lowering the pressure by a factor of 3 (right), the dark center region fills in. Both sets of data are taken with 18 μJ pump and 9 μJ probe pulses.

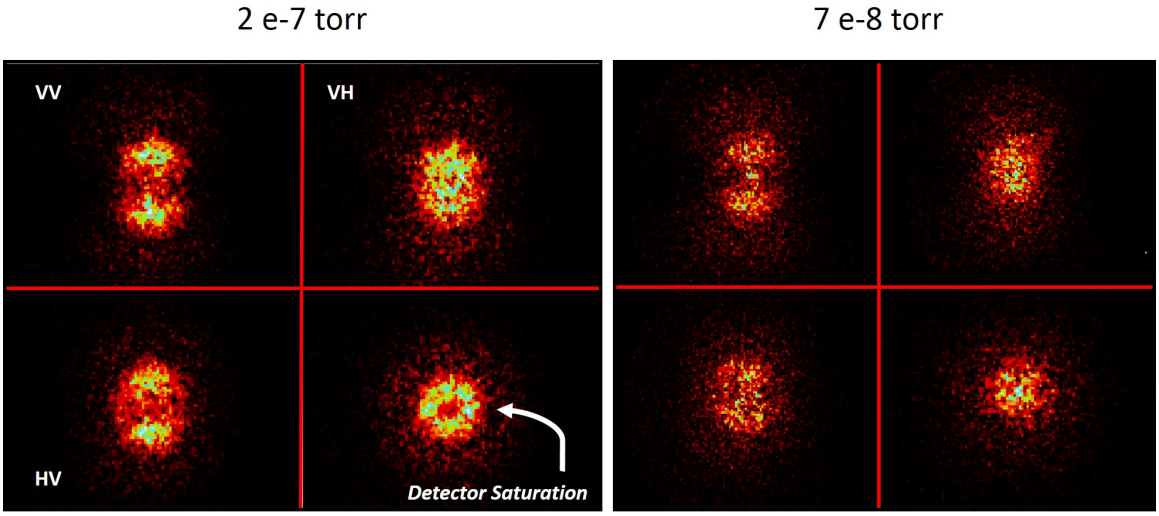

Figure 4.6.2: 2D FFT data for the X state of I_2^+ detected in the I^+ spectra at two different pressures. The higher pressure data on the left shows a dark spot in the center of the detector for polarization along the axis which is characteristic of saturation. By lowering the pressure by a factor of 3 (right), the dark center region fills in. Both sets of data are taken with 18 μJ pump and 9 μJ probe pulses.

the azimuthal angle ranging from (0, 2π) measured from the $+x$ axis in the $x-y$ plane The θ coordinate (altitude) goes from (0, π) measured from the $+z$ axis. To impose the cylindrical symmetry of the VMI, the ϕ coordinate is integrated over the three-dimensional distribution. This can be done without loss of generality as the cylindrically symmetric azimuthal contribution contains no useful information. The 3D image in (r, θ, ϕ) is then collapsed to a 2D image under the same conditions as that produced by the VMI.

The geometry produced by the pump pulse can be modeled based on the molecular orbitals being ionized. The X(3/2) state has a π_g symmetry and the A(3/2) has a π_u symmetry. The symmetries can be modeled with spherical harmonics creating distributions of the form:

$$S(\theta,\phi) \sim \sum_{l=0}^{l_{max}} \sum_{m=-l}^{l} B_{lm} Y_{lm}(\theta,\phi) \tag{4.6.1}$$

where the summation from l to l_{max} can include the orbital angular momentum quantum numbers necessary to describe simple to complex molecular systems. For systems with cylindrical symmetry the summation may be further reduced to a linear combination of Legendre polynomials. The observed geometries in the 2D FFT data appear to be lower order structures in terms of spherical harmonics as they are either "dumbell" or "circular" in shape. These structures can be produced by spherical harmonics up to $l = 2$, while higher orbital angular momenta have finer structure which we do not observe (or resolve) experimentally. A table of spherical harmonics is given in Table. 4.6.1. Graphic representations of the spherical harmonics are given in Fig. 4.6.3 and Fig. 4.6.4.

The probe pulse can be modeled geometrically in spherical coordinates as $\cos^2(\theta)$:

$$VerticalProbe \propto (\cos^2\theta)^n \tag{4.6.2}$$

$$HorizontalProbe \propto (\cos^2\phi)^n \tag{4.6.3}$$

Table 4.6.1: List of the first few spherical harmonics $Y_l^m(\theta, \phi)$.

$$Y_0^0 = \sqrt{\frac{1}{4\pi}}$$

$$Y_1^0 = \sqrt{\frac{3}{4\pi}} \cos\theta$$

$$Y_1^{\pm 1} = \mp \sqrt{\frac{3}{8\pi}} \sin\theta \, e^{\pm i\phi}$$

$$Y_2^0 = \sqrt{\frac{5}{16\pi}} (3\cos^2\theta - 1)$$

$$Y_2^{\pm 1} = \mp \sqrt{\frac{15}{8\pi}} \sin\theta \cos\theta \, e^{\pm i\phi}$$

$$Y_2^{\pm 2} = \sqrt{\frac{15}{32\pi}} \sin^2\theta \, e^{\pm 2i\phi}$$

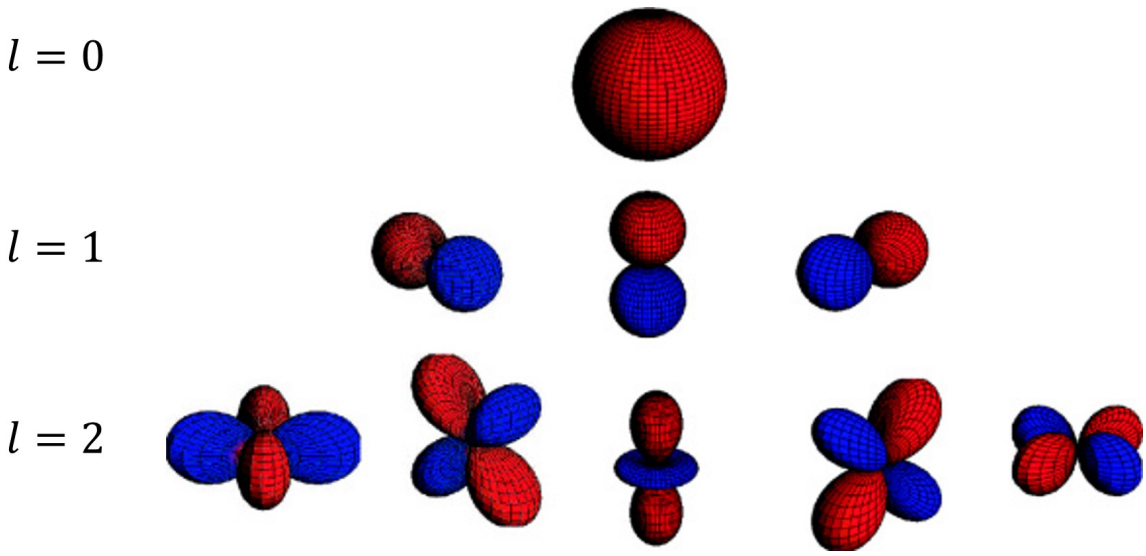

Figure 4.6.3: Spherical harmonics.

where n is the number of photons (order) involved in the bond softening process. The order of the bond softening is n = 1, 2, 3, etc. for one-photon, two-photon, etc. processes. These parameters can be adjusted to model the ionization structure observed in the data. The simulated probe pulse in Eq. 4.6.2 is along the z axis and in the terminology used up to this point will be labeled as vertical polarization. Horizontal polarization can be represented by the same function, but rotated into the $x-y$ plane such that the maxima lie at + and - x. For consistency, the angular coordinates must be transformed as well and $\theta \rightarrow \phi$. These geometries are shown schematically in Fig. 4.6.5.

4.6.2 Structure of the X and A States of I_2

Figs. 4.6.5 and 4.6.6 show the proposed geometry of the functions of the pump and probe pulses and the results of the simulation to produce a 2D VMI image. Spherical harmonics used to represent the ionization of the inner orbitals are based on the symmetry of the X and A state molecular orbitals. The X state has nodal planes along and perpendicular to the molecular axis and the A state has 1 nodal plane along the molecular axis. From Fig. 4.6.4, the X state orbital could be modeled with the Y_2^1 harmonic and the A state with the Y_1^1 harmonic as these exhibit the proper symmetries. The ionization due to the pump pulse and the probe step can then be simulated to produce 2D VMI images for the four polarization configurations of interest.

The simulations reproduce the overall structure observed in the experimental data. For the A state, the probe is simulated with a one-photon bond softening and the X state is simulated with two-photon bond softening. The order of the bond softening goes as the probe pulse to the n, where $n = 1$ for a one-photon process and 2 for a two-photon process. The data and simulations are compared in Figs. 4.6.7 and 4.6.8. The simulations for the A

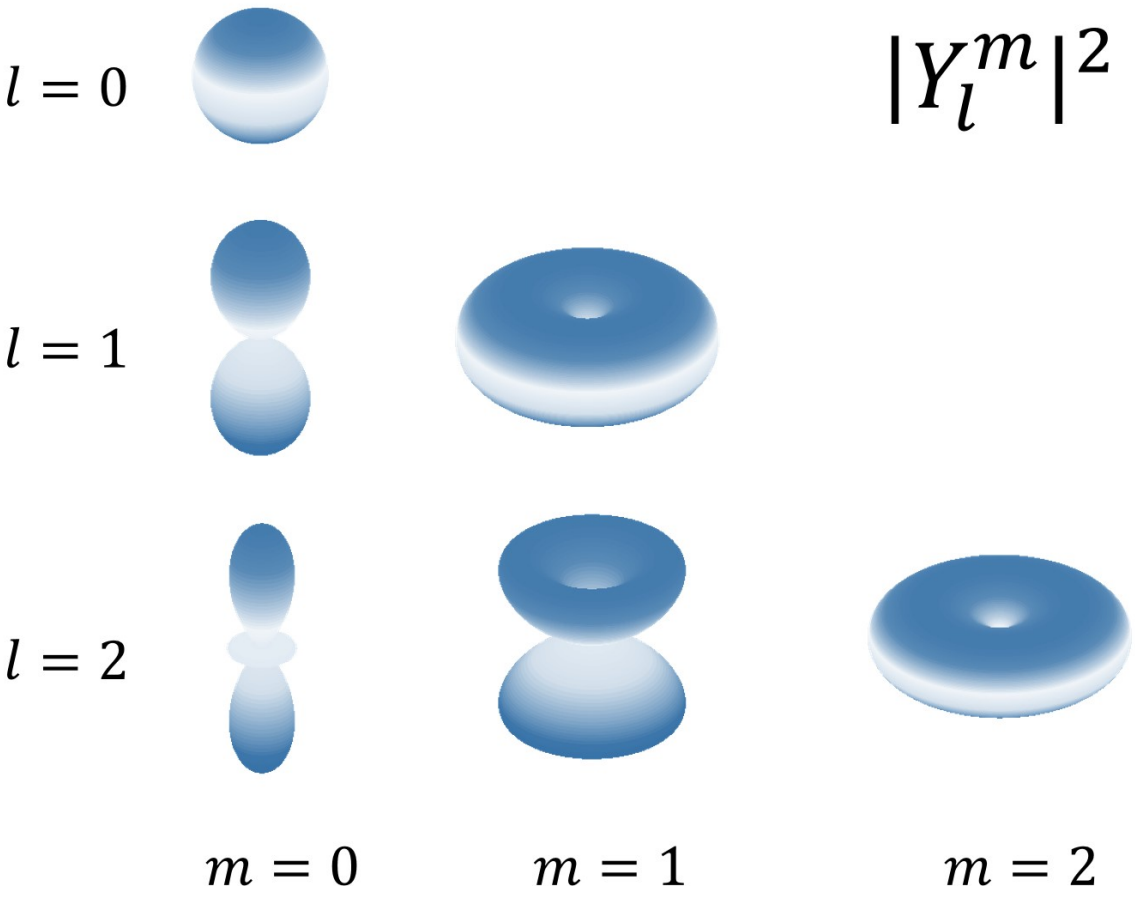

Figure 4.6.4: Magnitude squared distributions for spherical harmonics $l = 0, 1$, and 2.

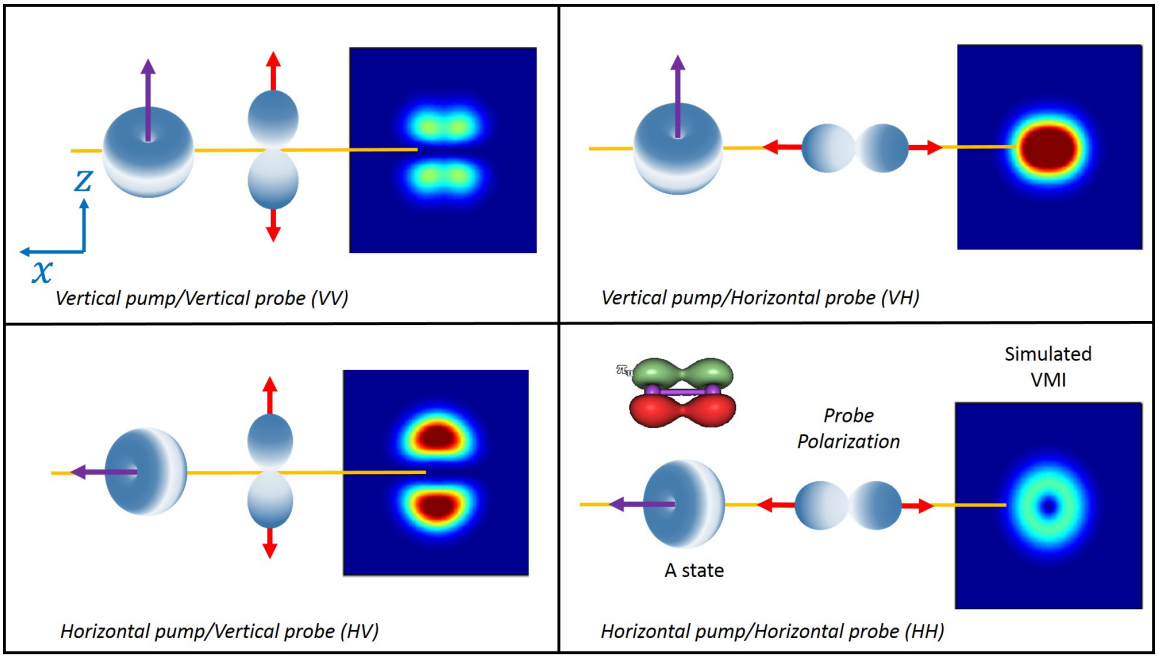

Figure 4.6.5: Pump-probe polarization geometry and simulated VMI data for the A state of I_2^+ detected through one-photon bond softening in the I^+ spectra. The top row has a vertical pump pulse polarization with a parallel or perpendicular probe and the bottom row has a horizontal pump pulse polarization with a parallel or perpendicular probe. The A state is modeled with spherical harmonic Y_1^1 ($l = 1, m = 1$).

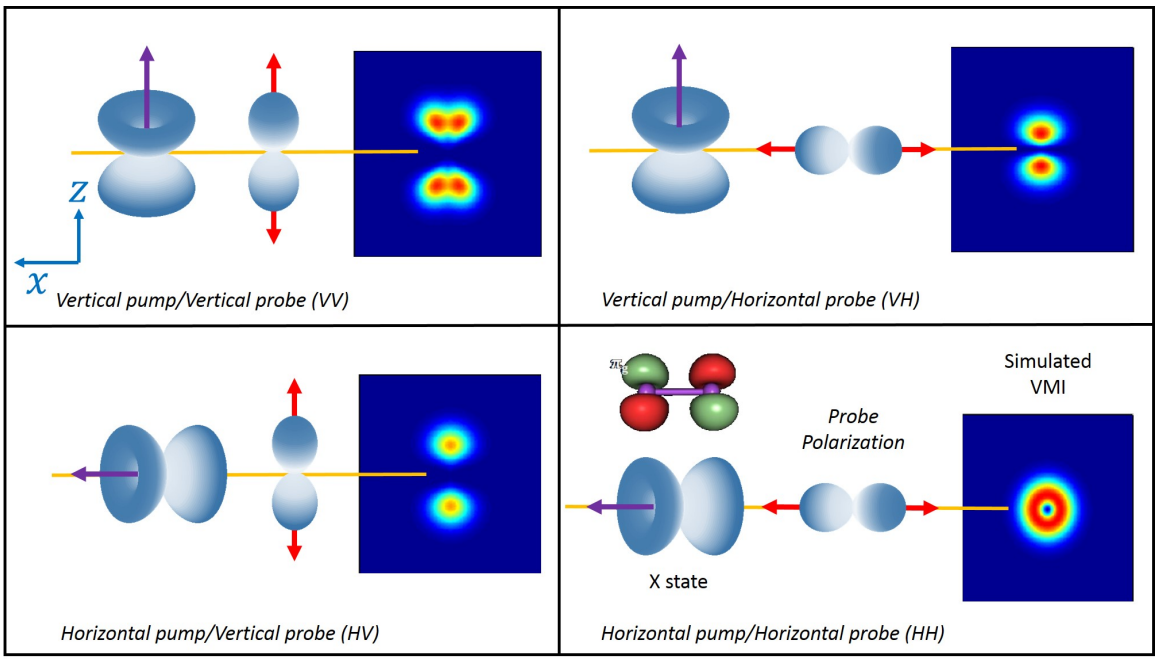

Figure 4.6.6: Pump-probe polarization geometry and 2D FFT images for the X state of I_2^+ detected through two-photon bond softening in the I^+ spectra. The top row has a vertical pump pulse polarization with a parallel or perpendicular probe and the bottom row has a horizontal pump pulse polarization with a parallel or perpendicular probe. The X state is represented by the spherical harmonic Y_2^1 ($l = 2, m = 1$).

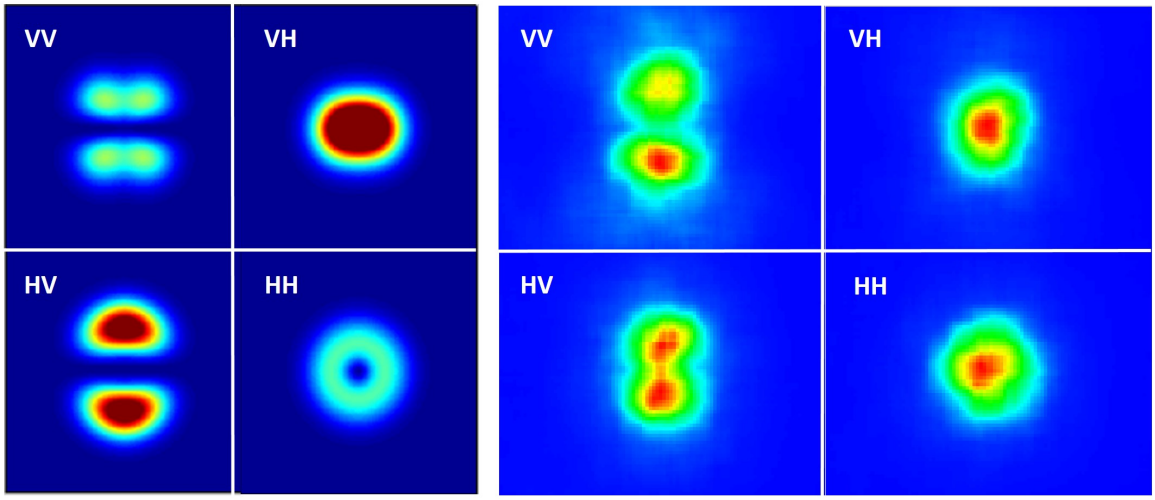

Figure 4.6.7: Simulated and experimental 2D FFT images for the A state of I_2^+ detected through one-photon bond softening in the I^+ spectra. The top row has a vertical pump pulse polarization with a parallel or perpendicular probe and the bottom row has a horizontal pump pulse polarization with a parallel or perpendicular probe. The pulse energies are 18 μJ pump and 9 μJ probe. The experimental data is block averaged to 5 pixels and then smoothed. The simulated A state is represented by the spherical harmonic Y_1^1 ($l = 1, m = 1$).

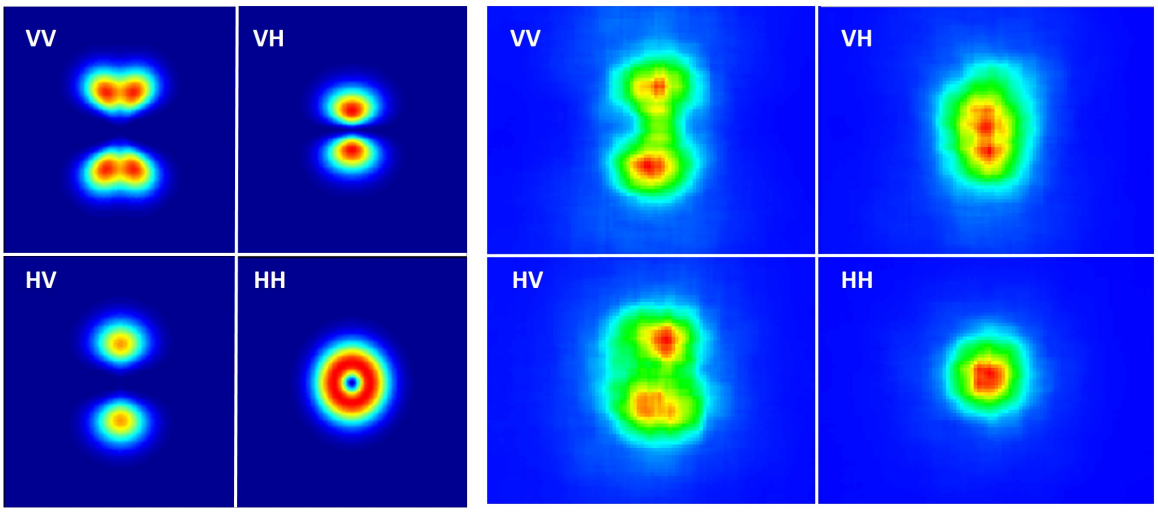

Figure 4.6.8: Simulated and experimental 2D FFT images for the X state of I_2^+ detected through bond softening in the I^+ spectra. The top row has a vertical pump pulse polarization with a parallel or perpendicular probe and the bottom row has a horizontal pump pulse polarization with a parallel or perpendicular probe. The pulse energies are 18 μJ pump and 9 μJ probe. The experimental data is block averaged to 5 pixels and then smoothed. The simulated X state is represented by the spherical harmonic Y_2^1 ($l = 2, m = 1$).

state indeed show that signal is stronger when the polarizations are perpendicular compared to parallel (HV compared to VV) in agreement with the data. This is not clear in the data for the VH vs. HH polarizations, although the structure is reproduced by the simulations. The "ring" structure in the HH case is not clear in the data, however, including the contribution of the Y_0^0 harmonic in the simulation does fill in the center region of the ring as shown in Fig. 4.6.9. Contributions like those from the $l = 0$ harmonic are reasonable as a linear combination of harmonics is suggested by Eq. 4.6.1. Simulations for the X state also agree well with the geometries in the data shown in Fig. 4.6.8. The intensity of the signal in all four polarization cases is nearly equal, which agrees with the nearly constant FFT amplitudes measured experimentally suggesting that the π_g orbital does not show a strong preference for a parallel or perpendicular transition, perhaps due to the nodal planes. The "ring" structure is again present in the HH configuration, but as shown in Fig. 4.6.10, the contribution of the Y_0^0 harmonic fills in the central region.

4.6.3 Further Modeling of the Ionization of I_2

The experimental data and simulations show qualitative agreement, however, the structure of the dissociation energy differs enough to propose an alternate hypothesis. The above section assumed that the ionizing laser pulse removes electrons from the X and A orbitals to produce the states directly through ionization. Another possibility is that ionization results in the X state directly and that population is then trasfered to the A state via the one-photon resonance between the states. In this case, the A state is not produced directly through ionization, but from a resonant transfer of the population from the X state. The transition between the states is a parallel transition such that it is strongest when the ionizing laser is along the molecular axis. Since the ionization occurs for a randomly oriented intial

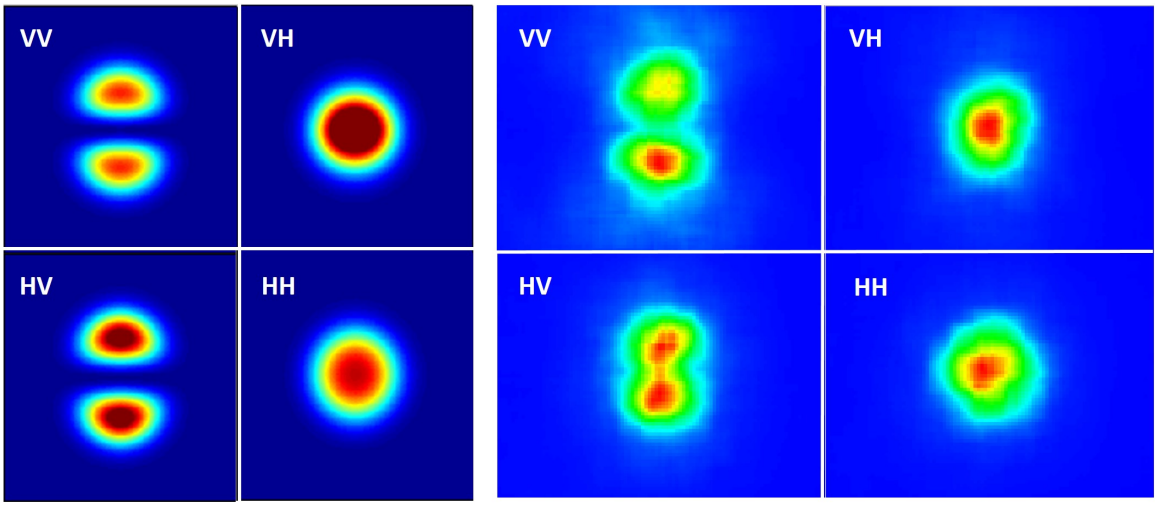

Figure 4.6.9: Simulated and experimental 2D FFT images for the A state of I_2^+ detected through one-photon bond softening in the I^+ spectra. The simulated A state is represented by the spherical harmonic Y_1^1 $(l = 1, m = 1)$ + 20 Y_0^0 $(l = 0, m = 0)$ and the central region of the HH case fills in.

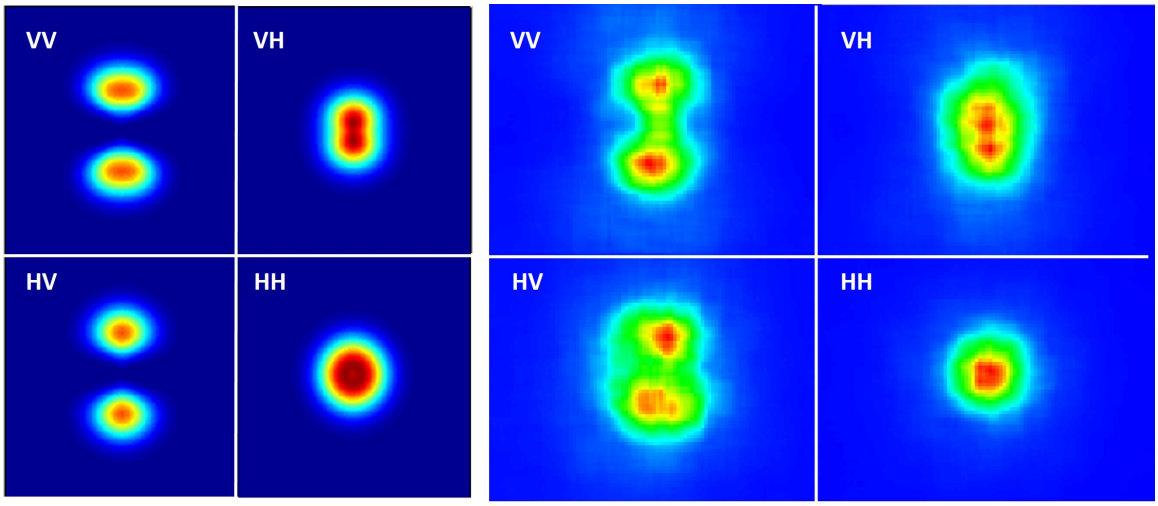

Figure 4.6.10: Simulated and experimental 2D FFT images for the X state of I_2^+ detected through two-photon bond softening in the I^+ spectra. The simulated X state is represented by the spherical harmonic Y_2^1 $(l = 2, m = 1)$ + 20 Y_0^0 $(l = 0, m = 0)$ and the central region of the HH case fills in.

ensembel of molecules, the resulting distribution will reflect the selection of all possible angular orientations. The distribution of the A state which is then probed will be of a $\cos^2\theta$ distribution, instead of the above proposed $\sin^2\theta$ distribution resulting from the Y_1^1 spherical harmonic. We propose that the X and A states are mixed in the neutral and since the ionization potential of the HOMO X state is less than the HOMO-1 A state, the resulting population after ionization will primarily be in the X state. In this section, the pump ionization step models the X state as a nearly isotropic distribution and the A state as a $\cos^2\theta$ distribution. The anisotropy of the X state may be reflected in the A state, though we believe the resonant coupling producing the $\cos^2\theta$ A state distribution will dominate. The resonant transfer of population to the A state occurs post-ionization and the probe still detects the A state through dissociation via bond softening.

This description is also in agreement with earlier work in I_2 [38]. In that work, 400 nm light was use in a pump-probe experiment to detect the A state through ionization to a dissociating channel of I_2^{2+}. The 400 nm light is non-resonant for the X-A transition, so the A state must have been produced directly by the pump through ionization of the neutral. In this case, the A state would ionize more strongly with a pulse perpendicular to the molecular axis as the electron distribution is primarily perpendicular to the axis. This was indeed seen in that experiment. However, if the A state is produced through resonant transfer with the X state, the distribution will be $\cos^2\theta$. These simulations based on a nearly isotropic X state distribution and a preferential $\cos^2\theta$ A state distribution suggest that the ionization of the neutral leaves the ion in a mixed state. This has been seen previously in iodine as described by the work of Chapter 2 and [72].

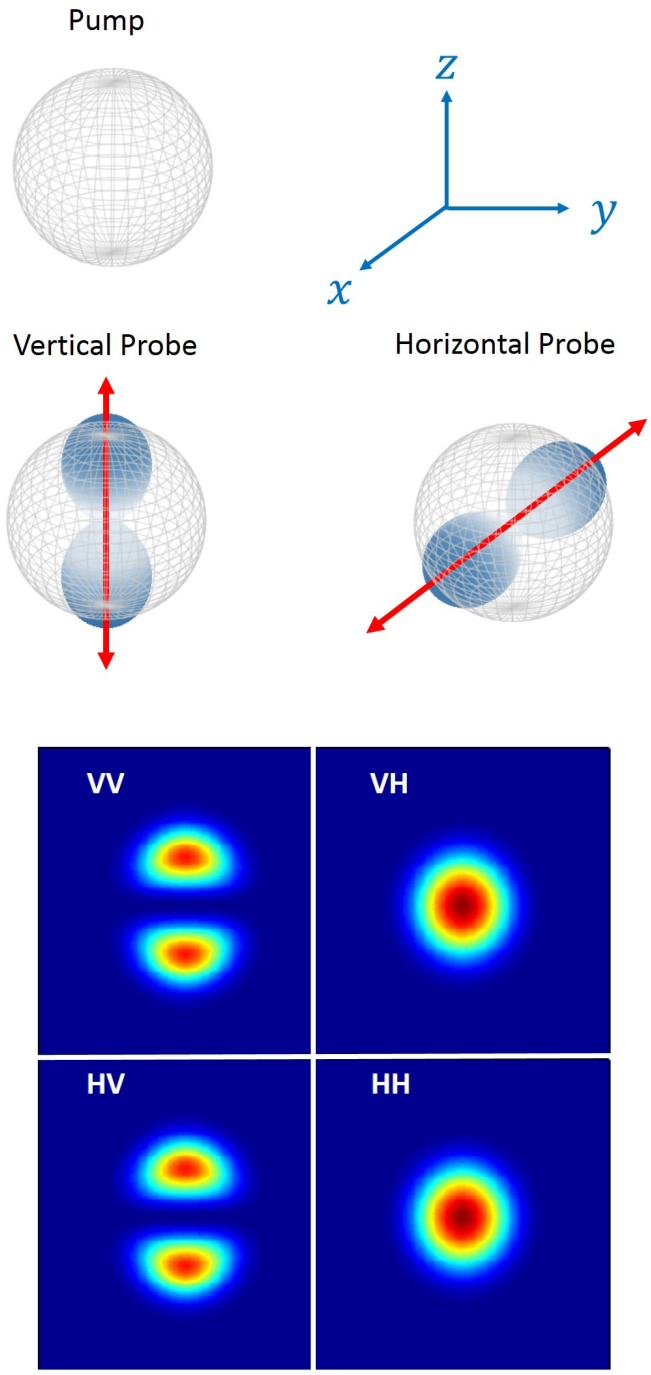

Figure 4.7.1: Schematic of the pump ionization step and the geometry of the probe for an isotropic distribution (top). Simulated image for an isotropic distribution of $\sin^2\theta + \cos^2\theta$ (bottom).

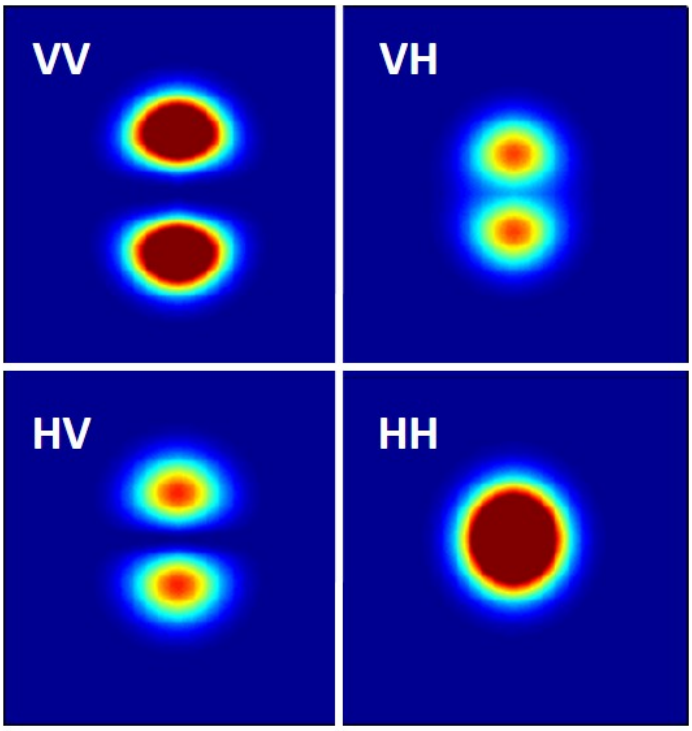

Figure 4.7.2: Simulated 2D FFT images for the A state of I_2^+ with a dominant $\cos^2\theta$ distribution detected through one-photon bond softening in the I^+ spectra. The simulated A state is represented by $\sin^2\theta + \cos^2\theta/0.1$ to represent a stronger selection of the resonant transfer process compared to direct ionization.

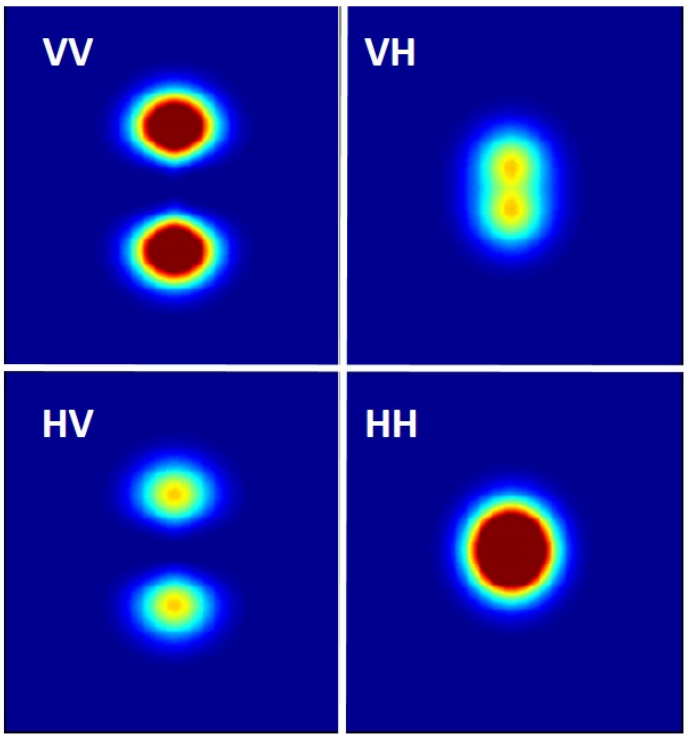

Figure 4.7.3: Simulated 2D FFT images for the X state of I_2^+ detected through two-photon bond softening in the I^+ spectra. The simulated X state is represented by $\sin^2\theta + \cos^2\theta/0.2$ to represent a slightly anisotropic distribution.

4.7 Conclusions

This chapter discussed the construction and characterization of the VMI detector and examined the inner orbital ionization of I_2. We have found that the X(3/2) and A(3/2) states are produced by the ionizing pump pulse and measured their frequencies using Fourier transform spectroscopy. Further confirmation that two distinct states are produced through ionization of the neutral exists in the observed energy dependence of the bond softening induced by a probe pulse. The photon order of the bond softening differs by one between the X and A states and from the potential curves available, a one-photon process appears likely for the dissociation of the A state, suggesting a two-photon process for the X state dissociation. We introduced a new method for imaging the molecular orbitals with 2D Fourier transforms such that pixels modulated at the X or A state frequencies can be used to create a two-dimensional geometric image of the ionization process. After identifying the states produced through inner orbital ionization, polarization measurements were made to examine the geometry of the orbitals. By describing the orbitals with spherical harmonics based on the orbital symmetries, simulations reproduce the VMI 2D FFT data qualitatively well. Interestingly, we find that the A state does modulate with a bond softening probe, even with a parallel pump-probe pulse configuration. This was not seen in our previous work of studying the ionization of the A state to the (2,0) channel in which the probe step was ionization. Ionization of inner orbitals can produce different configurations of the X and A states and these states may be probed differently by bond softening or ionization. These results suggest that the physics of the probe in either bond softening or ionization may be a sensitive tool for studying inner orbital ionization.

Chapter 5

Conclusions and Outlook

5.1 Interference of Inner Orbitals

The work presented in Chapter 4 on inner orbital ionization and characterization of the X and A states is part of the background needed for a future experiment. We have seen that the X and A (HOMO and HOMO-1) orbitals are ionized by a pump pulse as we have been able to measure the periods of vibration through Fourier spectroscopy. Each state also has a different dependence on the energy of the probe pulse, again suggesting that there is population in each of these states and that we have a measurable degree of control over the populations in these states. This technique can be described as excitation through ionization. There is a question of whether or not the production of these states through ionization can result in coherence between the states. In other words, are the populations in the HOMO and HOMO-1 orbitals coherent? Studying the X and A states of I_2^+ may allow us to independently measure whether the A state is produced directly through ionization or a resonant transfer of population with the X state.

Population can generally be transfered through two mechanisms. The first, driving the transition on resonance to produce real population transfer throughout the repetitive cycles of the laser interaction. Population may also be transfered impulsively. In the impulsive case, the molecule interacts with a non-resonant field for a period of time much shorter than the vibrational period. The broad bandwidth of the ultrafast laser spans the separation between multiple vibrational levels allowing for Raman transitions. Our group has observed vibrational motion in the impulsive limit using 25 fs pulses compared to a vibrational period of 155 fs in the vibration of neutral I_2. This phenomenon has been known as Lochfrass [39]. In that experiment, ionization creates a hole in the vibrational wave packet and the hole evolves in a coherent fashion.

As the electrons removed through ionization leave holes in the inner orbitals, there may be coherent evolution of the holes after ionization. So, the wavepacket remaining after ionization can evolve coherently. We wish to study the coherence between multiple, specific orbitals after ionization. However, the Lochfrass experiments used ionization as a probe to examine the remaining coherent hole in the neutral created by ionization. Further, the pulses used in the work of Chapter 4 are short, but are not short enough to be impulsive as the separation of the X and A states is about 1.6 eV. Transfering population impulsively here would require pulses of about 1 fs, while we used pulses of 50 fs. Still, we were able to observe the excitation of the X and A states. The conclusion being that non-resonant and non-impulsive pulses can still result in excitation. Can this type of interaction result in coherence?

It appears that the X and A states are produced through ionization. However, there is a resonance between the states as they are separated by about 1.6 eV. The resonant transfer of population from X $\rightarrow$ A will follow selection rules as the dipole for such a transition (between π_g and π_u) lies along the molecular axis. To transfer population, the laser must

be polarized along this axis and a polarization perpendicular to the axis will not result in population transfer. The A state can be produced through ionization, as shown in preivous work [38], and shows a preference for polarization perpendicular to the axis. We then have two ways of studying the pathways for producing the A state. One being resonant transfer with the X state using parallel polarization and the other producing the A state through ionization with perpendicular polarization. Any coherence may be observed with a time-delayed probe pulse. With the probe polarization parallel, the resonance between X and A is allowed while perpendicular polarization closes the resonance due to selection rules. The populations of the X and A states may then interfere if there is coherence between the states.

We have modeled the evolution of population in the X and A states with a resonant coupling pulse to allow population transfer between the states. The potential curves with the ionization and coupling pulses are shown in Fig. 5.2.1. The ionization step can place population in both states. The periods of vibration for the states are nearly 2:1 as the X state is about 140 fs and the A state is about 270 fs. This means that both states will periodically be at the same R to interfere. The interference could then occur when the X state wave packet is at the outer turning point of the well and the A state is at the inner turning point as shown in Fig. 5.2.2. At this point around 270 fs, the second, resonant coupling pulse at 800 nm is applied which transfers population between the states. After the coupling pulse, the population in each state can be plotted and is shown in Fig. 5.2.3. It appears that it is possible to observe coherence between the states in a pump-couple-probe experiment using 800 nm light.

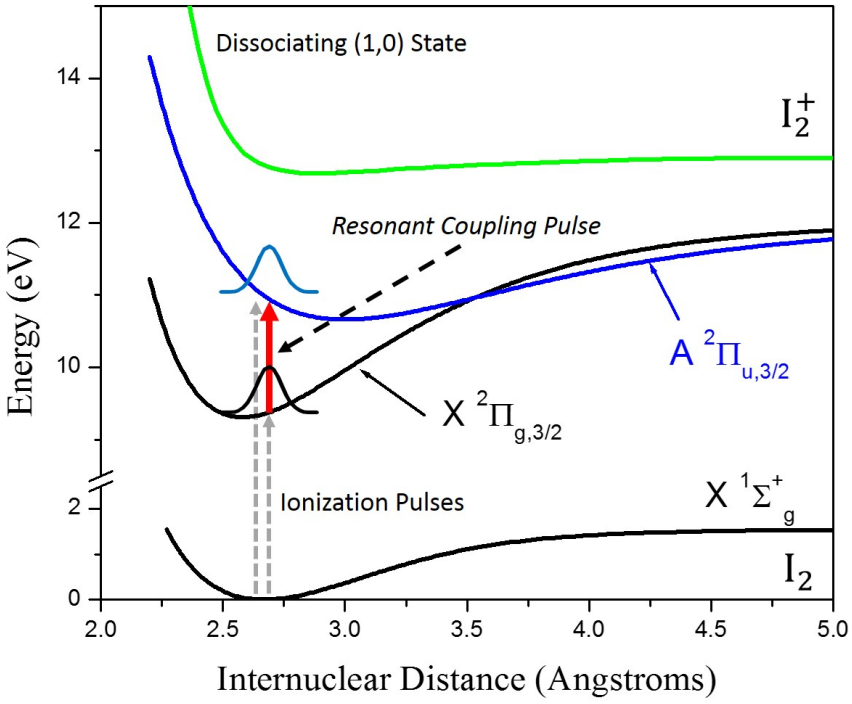

Figure 5.2.1: Potential curves showing the ionization and coupling steps in the X and A states of I_2^+.

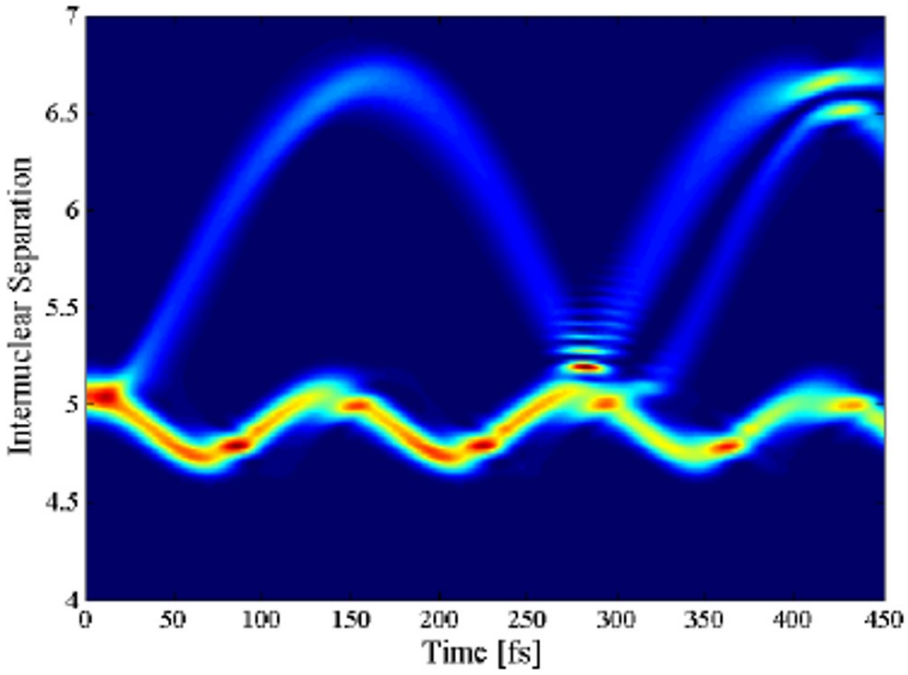

Figure 5.2.2: Simulations of wave packets in the X and A states of I_2^+.

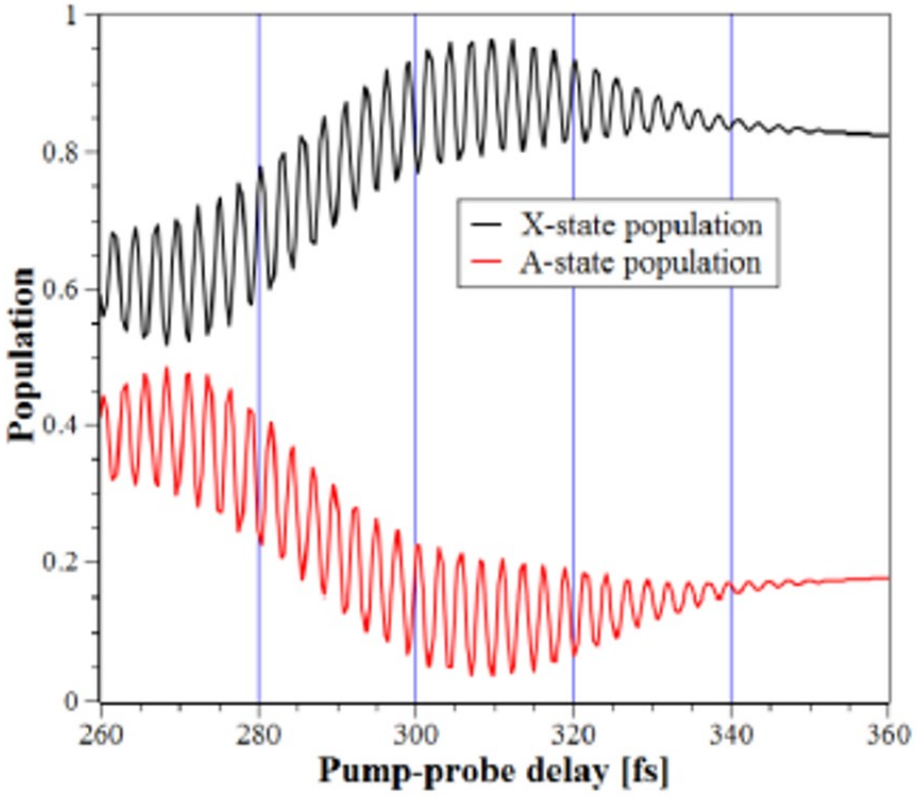

Figure 5.2.3: Simulations showing the coherent transfer of population between the X and A states of I_2^+.

5.2 Conclusions

This work focused on ionizing the I_2 molecule with a strong laser field. Chapter 2 studied ionization from the B state of the neutral with an asymmetric probe pulse. We measured the spatial asymmetry of the CAD channel of I_2^{2+} as a function of internuclear separation by first exciting the neutral molecule to the B state and letting it evolve in time. By varying the delay of a $1\omega 2\omega$ probe pulse, we measure the asymmetry as a function of internuclear separation for different values of the $1\omega 2\omega$ phase. The (2,0) channel is produced asymmetrically upon ionization of the B state by the asymmetric field. The maximum amplitude of the spatial asymmetry increases with R, goes through a maximum, and then decreases while the phase of the maximum asymmetry is constant. By comparing these results to a simple two-level model in a dc field, we found that the molecules are ionized directly into the field-dressed ionic states of the dication. This result implies that ionization of the molecule results in mixed states and the gerade/ungerade symmetry gives rise to asymmetric ion yields.

Chapter 3 examined charge transfer around a critical internuclear separation. We directly observed multi-electron effects both experimentally and theoretically in the asymmetric depletion of the (2,0) channel of I_2^{2+}. The dynamics of two-electron charge transfer produce the dominant pathway for ionization of the molecule at small internuclear separations around R_c. As R gets larger and the molecule expands, the two-electron effects become negligible and the one-electron description of EI sufficiently describes the ionization dynamics. This result reconciled recent findings in N_2 and also extended the first experimental observation of enhanced ionization by revealing the importance of multi-electron effects. Although studying dynamics of a single active electron has proven useful in many systems, the observation of charge transfer around R_c may have importance in experiments

where multi-electron effects are needed to interpret experimental results.

In order to study the spatial structure of ionization and dissociation, we developed a velocity map imaging detector. Chapter 4 describes implementing the detector and optimizing the ion optics to produce a focused velocity mapping image. This system was used to study inner orbital ionization of I_2 and when coupled with the technique of Fourier transform spectroscopy, was used to obtain geometric information about the ionizing orbitals. Fourier spectroscopy allowed for determination of the states produced through ionization and we were able to measure vibrational periods of the HOMO and HOMO-1 orbitals of I_2 through a bond softening mechanism with a dissociating state. By using different pump and probe polarizations, we were able to image different geometries, allowing us to develop a picture of the structure of the inner orbitals. Describing the orbitals with low order spherical harmonics and performing simulations to produce VMI images, we found qualitative agreement with the structures observed in the experimental data. The new technique of 2D FFT spectroscopy should be applicable to larger molecular systems where inner orbital ionization may be occuring. It is also another method of imaging molecular orbitals which has been a topic of recent interest and has been pursued by high harmonic generation and attosecond physics.

Bibliography

[1] P.A. Franken, A. E. Hill, C.W. Peters, and G. Weinreich, Phys. Rev. Lett. **7**, 118 (1961).

[2] P. Agostini, F. Fabre, G. Mainfray, and G.Petite, Phys. Rev. Lett. **42** 1127 (1979).

[3] L. V. Keldysh, Soviet Physics. JETP 2354 (1965).

[4] M. V. Ammosov, N. B. Delone, and V. P. Krainov, Soviet Physics. JETP **64.6** pp. 1191-1194 (1986).

[5] T. Auguste, P. Monot, L. A. Lompré, G. Mainfray, and C. Manus, J. Phys. B **25**, 4181 (1992).

[6] P. Dietrich, M. Yu. Ivanov, F. A. Ilkov, and P. B. Corkum, Phys. Rev. Lett. **77**, 4150 (1996).

[7] M. Ivanov, T. Seideman, P. Corkum, F. Ilkov, and P. Dietrich, Phys. Rev. A **54**, 1541 (1996).

[8] L. J. Frasinski, C. R. Courtney, and K. Codling, J. Mod. Opt. **50**, 485-495 (2003).

[9] C. Cornaggia, J. Lavancier, D. Normand, J. Morellec, and H. X. Liu, Phys. Rev. A **42**, 5464 (1990).

[10] C. Guo, M. Li, and G. N. Gibson, Phys. Rev. Lett. **82**, 2492 (1999).

[11] G. N. Gibson, M. Li, C. Guo, and J. P. Nibarger, Phys. Rev. A **58**, 4723 (1998).

[12] J. P. Nibarger, S. V. Menon, and G. N. Gibson, Phys. Rev. A **63**, 053406 (2001).

[13] J. P. Nibarger, M. Li, S. Menon, and G. N. Gibson, Phys. Rev. Lett. **83**, 4975 (1999).

[14] L. J. Frasinski, K. Codling, P. Hatherly, J. Barr, I. N. Ross, and W. T. Toner, Phys. Rev. Lett. **58**, 2424 (1987).

[15] P. Dietrich, D. T. Strickland, M. Laberge, and P. B. Corkum, Phys. Rev. A **47**, 2305 (1993).

[16] L. Quaglia and C. Cornaggia, Phys. Rev. Lett. **84**, 4565 (2000).

[17] T. Zuo and A. D. Bandrauk, Phys. Rev. A **52**, 2511 (1995).

[18] E. Constant, H. Stapelfeldt, and P. B. Corkum, Phys. Rev. Lett. **76**, 4140 (1996).

[19] R. Bavli and H. Metiu, Phys. Rev. Lett. **69**, 1986 (1992).

[20] T. Seideman, M. Yu. Ivanov, and P. B. Corkum, Phys. Rev. Lett. **75**, 2819 (1995).

[21] A. Saenz, Phys. Rev. A **61**, 051402 (2000).

[22] K. Codling, L. J. Frasinski, and P. A. Hatherly, J. Phys. B **22**, L321 (1989).

[23] I. Kawata, H. Kono, Y. Fujimura, and A. D. Bandrauk, Phys. Rev. A **62**, 031401(R) (2000).

[24] P. H. Bucksbaum, A. Zavriyev, H. G. Muller, and D. W. Schumacher, Phys. Rev. Lett. **64**, 1883 (1990).

[25] R. N. Coffee, L. Fang, and G. N. Gibson, Phys. Rev. A **73**, 043417 (2006).

[26] R. S. Mulliken, J. Chem. Phys. **7**, 20 (1939).

[27] R. N. Coffee and G. N. Gibson, Phys. Rev. A **72**, 011401(R) (2005).

[28] T. Zuo, S. Chelkowski, and A. D. Bandrauk, Phys. Rev. A **48**, 3837 (1993).

[29] S. Chelkowski, T. Zuo, and A. D. Bandrauk, Phys. Rev. A **46**, 5342 (1992).

[30] H. Yu, T. Zuo, and A. D. Bandrauk, Phys. Rev. A **54**, 3290 (1996).

[31] K. Harumiya, H. Kono, Y. Fujimura, I. Kawata, and A. D. Bandrauk, Phys. Rev. A **66**, 043403 (2002).

[32] A. D. Bandrauk and S. Chelkowski, Phys. Rev. Lett. **84**, 3562 (2000).

[33] B. Sheehy, B. Walker, and L. F. DiMauro, Phys. Rev. Lett. **74**, 4799 (1995).

[34] K. J. Betsch, D. W. Pinkham, and R. R. Jones, Phys. Rev. Lett. **105**, 223002 (2010).

[35] S. De, I. Znakovskaya, D. Ray, F. Anis, N. G. Johnson, I. A. Bocharova, M. Magrakvelidze, B. D. Esry, C. L. Cocke, I. V. Litvinyuk, and M. F. Kling, Phys. Rev. Lett. **103**, 153002 (2009).

[36] D. Ray, F. He, S. De, W. Cao, H. Mashiko, P. Ranitovic, K. P. Singh, I. Znakovskaya, U. Thumm, G. G. Paulus, M. F. Kling, I. V. Litvinyuk, and C. L. Cocke, Phys. Rev. Lett. **103**, 223201 (2009).

[37] L. Fang and G. N. Gibson, Phys. Rev. A **81**, 033410 (2010).

[38] L. Fang and G. N. Gibson, Phys. Rev. A **75**, 063410 (2007).

[39] L. Fang and G. N. Gibson, Phys. Rev. Lett. **100**, 103003 (2008).

[40] C. Guo, M. Li, J. P. Nibarger, and G. N. Gibson, Phys. Rev. A **58**, R4271 (1998).

[41] G. N. Gibson, R. N. Coffee, and L. Fang, Phys. Rev. A **73**, 023418 (2006).

[42] G. N. Gibson, Phys. Rev. A **67**, 043401 (2003).

[43] W. C. Wiley and I. H. McLaren, *Rev. Sci. Instrum.* **26**, 1150 (1955).

[44] E. Gagnon, P. Ranitovic, X. Tong, C. L. Cocke, M. M. Murnane, H. C. Kapteyn, and A. S. Sandhu, Science **317**, 1374 (2007).

[45] B. K. McFarland, J. P. Farrell, P. H. Bucksbaum, and M. Gühr, Science **322**, 1232 (2008).

[46] W. Li, X. Zhou, R. Lock, S. Patchkovskii, A. Stolow, H. C. Kapteyn, and M. M. Murnane, Science **322**, 1207 (2008).

[47] H. Akagi, T. Otobe, A. Staudte, A. Shiner, F. Turner, R. Dörner, D. M. Villeneuve, and P. B. Corkum, Science **325**, 1364 (2009).

[48] M. Kotur, T. C. Weinacht, C. Zhou, and S. Matsika, Phys. Rev. X **1**, 021010 (2011).

[49] H. Chen, V. Tagliamonti, G. N. Gibson, Phys. Rev. Lett. **109**, 193002 (2012).

[50] P. B. Corkum, Phys. Rev. Lett. **71**, 1994 (1993).

[51] A. D. Bandrauk, H. Z. Lu, Phys. Rev. A **68**, 043408 (2003).

[52] Y. Mairesse, J. Higuet, N. Dudovich, D. Shafir, B. Fabre, E. Mével, E. Constant, S. Patchkovskii, Z. Walters, M. Yu. Ivanov, and O. Smirnova, Phys. Rev. Lett. **104**, 213601 (2010).

[53] T. Seideman, M. Yu. Ivanov, and P. B. Corkum, Phys. Rev. Lett. **75**, 2819 (1995).

[54] T. Zuo and A. D. Bandrauk, Phys. Rev. A **52**, R2511 (1995).

[55] E. Constant, H. Stapelfeldt, and P. B. Corkum, Phys. Rev. Lett. **76**, 4140 (1996).

[56] D. Pavičić, A. Kiess, T. W. Hansch, and H. Figger, Phys. Rev. Lett. **94**, 163002 (2005).

[57] I. Bocharova, R. Karimi, E. F. Penka, J.-P. Brichta, P. Lassonde, X. Fu, J.-C. Kieffer, A. D. Bandrauk, I. Litvinyuk, J. Sanderson, and F. Légaré, Phys. Rev. Lett. **107**, 063201 (2011).

[58] E. Lötstedt, T. Kato, and K. Yamanouchi, Phys. Rev. A **85**, 041402(R) (2012).

[59] H. Chen, L. Fang, V. Tagliamonti, G. N. Gibson, Phys. Rev. A **84**, 043427 (2011).

[60] H. Chen, V. Tagliamonti, and G. N. Gibson, Phys. Rev. A **86**, 051403(R) (2012).

[61] J. P. Nibarger, M. Li, S. Menon, and G. N. Gibson, Phys. Rev. Lett. **83**, 4975 (1999).

[62] C. Guo, M. Li, and G. N. Gibson, Phys. Rev. Lett. **82**, 2492 (1999).

[63] J. H. Posthumus, K. Codling, L. J. Frasinski, and M. R. Thompson, Laser Phys. **7**, 813 (1997).

[64] G. N. Gibson, M. Li, C. Guo, and J. P. Nibarger, Phys. Rev. A **58**, 4723 (1998).

[65] K. Harumiya, H. Kono, Y. Fujimura, I. Kawata, and A. D. Bandrauk, Phys. Rev. A **66**, 043403 (2002).

[66] H. Yu and A. D. Bandrauk, Phys. Rev. A **56**, 685 (1997).

[67] L. Torlina, M. Ivanov, Z. B. Walters, and O. Smirnova, Phys. Rev. A **86**, 043409 (2012).

[68] W. Li, A. A. Jaroń-Becker, C. W. Hogle, V. Sharma, X. Zhou, A. Becker, H. C. Kapteyn, and M. M. Murnane, PNAS **107**, 20219 (2010).

[69] B. Sheehy, B. Walker, and L. F. DiMauro, Phys. Rev. Lett. **74**, 4799 (1995).

[70] S. De *et al.*, Phys. Rev. Lett. **103**, 153002 (2009).

[71] K. J. Betsch, D. W. Pinkham, and R. R. Jones, Phys. Rev. Lett. **105**, 223002 (2010).

[72] V. Tagliamonti, H. Chen, and G. N. Gibson, Phys. Rev. A **84** 043424 (2011).

[73] S. V. Menon, J. P. Nibarger, G. N. Gibson, J. Phys. B: At. Mol. Opt. Phys. **35**, 2961 (2002).

[74] J. Breidbach and L. S. Cederbaum, Phys. Rev. Lett. **94**, 033901 (2005).

[75] O. Smirnova, Y. Mairesse, S. Patchkovskii, N. Dudovich, D. Villeneuve, P. Corkum, and M. Y. Ivanov, Nature **460**, 972 (2009).

[76] S. Patchkovskii, Z. Zhao, T. Brabec, and D. M. Villeneuve, Phys. Rev. Lett. **97**, 123003 (2006).

[77] A. E. Boguslavskiy, J. Mikosch, A. Gijsbertsen, M. Spanner, S. Patchkovskii, N. Gador, M. J. J. Vrakking, A. Stolow, Science **335** 1336, (2012).

[78] J. P. Nibarger, S. V. Menon, and G. N. Gibson, Phys. Rev. A **63**, 053406 (2001).

[79] W. C. Wiley and I. H. McLaren, Rev. Sci. Instrum. **26**, 1150 (1955).

[80] G. N. Gibson, R. N. Coffee, and L. Fang, Phys. Rev. A **73**, 023418 (2006).

[81] G. N. Gibson, Phys. Rev. A **67**, 043401 (2003).

[82] I. Kawata, H. Kono, Y. Fujimura, and A. D. Bandrauk, Phys. Rev. A **62**, 031401(R) (2000).

[83] G. Camiolo, G. Castiglia, P. P. Corso, E. Fiordilino, and J. P. Marangos, Phys. Rev. A **79**, 063401 (2009).

[84] F. Verluise, *et al.*, Optics Letters **25**, 575 (2000).

[85] *Nonlinear Optics, Third Edition*, Robert W. Boyd, Academic Press, Elsevier Inc. (2008).

[86] G. M. Roberts, J. L. Nixon, J. Lecointre, E. Wrede, and J. R. R. Verlet, Rev. Sci. Instrum. **80**, 053104 (2009).

[87] *Imaging in Molecular Dynamics: Technology and Applications*, edited by Benjamin Whitaker, Cambridge University Press, Cambridge (2003).

[88] A. Eppink and D. H. Parker, Rev. Sci. Instrum. **68**, 3477 (1997).

[89] G. N. Gibson and R. R. Freeman, Phys. Rev. Lett. **67**, 1230 (1991).

[90] H. J. Worner, J. B. Bertrand, P. Hockett, P. B. Corkum, and D. M. Villeneuve, Phys. Rev. Lett. **104**, 233904 (2010).

[91] J. Itatani, J. Levesque, D. Zeidler, H. Niikura, H. Pepin, J. C. Kieffer, P. B. Corkum, and D. M. Villeneuve, Nature **432**, 867 (2004).

[92] H. Akagi, T. Otobe, A. Staudte, A. Shiner, F. Turner, R. Dorner, D. M. Villeneuve, P. B. Corkum, Science **325**, 1364 (2009).

[93] B. K. McFarland, J. P. Farrell, P. H. Bucksbaum, M. Guhr, Science **322**, 1232 (2008).

[94] M. Meckel, *et al.*, Science **320**, 1478 (2008).

[95] R. Murray, M. Spanner, S. Patchkovskii, and M.Y. Ivanov, Phys. Rev. Lett. **106**, 173001 (2011).

[96] D. Pavicic, K. F. Lee, D. M. Rayner, P. B. Corkum, and D. M. Villeneuve, Phys. Rev. Lett. **98**, 243001 (2007).

[97] S. Petretti *et al.*, Phys. Rev. Lett. **104**, 223001 (2010).

[98] P. H. Buckbaum, A. Zavriyev, H. G. Muller, and D. W. Schumacher, Phys. Rev. Lett. **64**, 1883 (1990).

[99] A. Zavriyev and P. H. Buckbaum, Phys. Rev. Lett. **70**, 1077 (1993).

[100] W. A. de Jong, L. Visscher, and W. C. Nieuwpoort, J. Chem. Phys. **107**, 9046 (1997).